POLITECNICO DI MILANO

School of Industrial and Information Engineering

Master of Science in Energy Engineering

1D Thermo-Fluid Dynamic Modelling of SI Engines: Exploring the Advantages of the Atkinson-Miller Cycle

Supervisor: Prof. Angelo Onorati

Candidates:

Chiara Iorio Ident. 904256
Filippo Stringa Ident. 863466

Academic Year 2018 - 2019

Ringraziamenti

Desideriamo innanzitutto ringraziare il Prof. Angelo Onorati per averci concesso l'opportunità di prendere parte a questo progetto, per il supporto, la pazienza e la costante fiducia dimostrataci. Un'altra dote, non del tutto scontata, è stata la sua incredibile disponibilità, aiuto fondamentale allo svolgimento di questa tesi con il giusto entusiasmo e per questo gliene siamo grati.
Un pensiero va indubbiamente alle nostre famiglie e amici, che in questi anni ci hanno sempre sostenuto incondizionatamente.
Senza i nostri compagni di università e di vita, poi, non saremmo mai arrivati alla fine di questo percorso, e di questo ne siamo abbastanza certi. Quindi vorremmo ringraziarli tutti: Adri, Ale, Dama, Diego, Fede, Gili e Samy.
Come promesso, una menzione d'onore va a Dani, che con tanta pazienza ha investito un po' del suo tempo da semi-disoccupato per svelarci i segreti di LaTeX. Senza di lui questa tesi non sarebbe stata così bella.

Milano, Luglio 2019 *Chiara e Filippo*

Ho pensato a lungo a cosa scrivere, a come scriverlo e a chi indirizzare questi ringraziamenti. Ci ho pensato così tanto che ho finito per indugiare per molto tempo, preoccupandomi troppo della forma e delle reazioni che certe parole avrebbero potuto suscitare, non capendo che infondo basta badare al senso, che i suoni baderanno a loro stessi. E mi sono decisa.
Una delle cose su cui non ho mai avuto dubbi, però, è l'estrema importanza che hanno avuto i miei genitori in tutto questo lungo... lunghissimo percorso, perché nessuno dovrebbe mai dare per scontata la presenza incondizionata di due persone, che seppur a centinaia di chilometri di distanza siano sempre pronte ad aver cura di te, a farti sapere che ci sono, che sia per curarti un mal di pancia, per consigliarti il programma giusto da impostare sulla lavatrice, o semplicemente per dirti che va tutto bene. Ed in sottofondo a tutte le telefonate da nord a sud non mancava mai un "Ciao piccola!" urlato dalla mia Toscina per salutare me, che di piccolo non ho quasi niente ma che ai suoi occhi probabilmente rimarrò sempre il piccolo Pizz, appunto. Troppo spesso ho trascurato il suo, di bisogno di sentirmi vicina, pensando che i miei problemi fossero troppo grandi per lasciare spazio anche a i suoi, e me ne pento ancora, ma proverò a rimettere a posto le cose, perché si sa, Timon non va da nessuna parte senza il suo Pumbaa, no? Chi invece mi ha sentita fin troppo vicina è sicuramente il Ciuccio, Francesca, con cui ho condiviso la stanza, la casa, la vita e gli esaurimenti nervosi per ben otto anni, il tutto intervallato da merende fatte di patatine dai gusti più improbabili, ma celestiali per i nostri palati sopraffini e da cene a base di pizza pistacchio e mortadella guardando per la diciottesima volta lo stesso film. Possiamo dire di aver creato un vero e proprio rito, insomma. E se per ogni uscita... strampalata, chiamiamola così, di Francesca del tipo "Puoi smettere di respirare, per favore?" (tutto vero, giuro) ce n'era almeno una fin troppo amorevole del tipo "Dai Pino, dammi un bacino!" di Cosimo, spettatore sfortunato di tutti i litigi e i drammi che solo due sorelle più piccole possono mettere su in quella casa che ormai ci sta un po' stretta, ma a cui infondo un pochino ci siamo affezionati. Sicuramente ho apprezzato le schiscette già pronte e tutti i brindisi allo scoccare della mezzanotte di ogni compleanno per farmi capire che lui, silenziosamente, non si dimentica mai di nulla, un po' meno tutte le volte che ho dovuto radergli la pelata.
Questi ringraziamenti si stanno facendo già un po' troppo lunghi e sono solo all'inizio. Uno dei miei più grandi difetti è la prolissità ed alcune delle persone che leggeranno queste pagine lo sanno bene, ma d'altronde tesi mia, ringraziamenti miei.
Non si possono di certo dimenticare gli amici del primo anno, i Polibros, Monica, Matteo, Annalisa, Aaron, Impry, Figo, Brambi, Simo che sono

stati i primi compagni di lezione e con cui, nonostante la distanza, le strade diverse e i tempi biblici di organizzazione, un momento per uno gnocco fritto lo si trova sempre.
(Come dici, Diego? Pensi che mi sia scordata di te? Ma non ci eravamo conosciuti al secondo anno io e te?)
Sono convinta che scegliersi gli amici sia un po' come guardarsi allo specchio, individuare ciò che ci manca, che ci piacerebbe fosse nostro e ricercarlo negli altri.
Il fatto è che noi amiamo sempre i diversi da noi, e continuiamo a cercarli in tutte le circostanze. L'imperturbabilità di Filo, ad esempio, è stato un grande aiuto alla nostra tesi, che è cominciata con un "Ok, Chiara, obiettivo: finire talmente in fretta la tesi da arrivare alla laurea abbronzati". Tra un caffè al Cheezy ed un cochino nei corridoi, siamo arrivati alla fine, anche discretamente abbronzati, direi. E anche se ha schifato fino alla fine le mie carezze e i miei abbracci come un bambino capriccioso, lo ringrazio lo stesso.
Fede e la sua incredibile capacità di fare comunella con chiunque hanno reso indubbiamente la vita al Poli più leggera, e grazie a lui, in qualsiasi momento decidessi di andare al bar, sapevo che ci sarebbe stato sempre qualcuno della Cheezy Gang pronto a farmi compagnia. Questa io la chiamo Freschezza.
Dei ringraziamenti vanno sicuramente anche ad Ale ed alla sua "sicilianità", che per me non significa altro che generosità, caffè offerti e massime siciliane che ormai sono diventate di uso comune anche per tutto il resto della gang. A Dama ed al suo essere spontaneo, a volte un po' troppo: non mi sono mica scordata di quel "Chiara, non sarebbe ora di rifarti la tinta?", eh. Aveva ragione. Alla purezza di Adri e al modo tutto suo di superca. . . scherzare. A Samy e alle sue canzoncine "motivazionali" che per sfinimento ho imparato ad apprezzare.
(Si, si adesso arrivo anche a te, Diego, tranquillo.)
Quasi dimenticavo, Diego! Probabilmente non lo perdonerò mai per avermi abbandonato proprio all'ultimo, per avermi privato dei suoi mirabolanti prodigi su Excel e delle sue correzioni sull'inglese, o dell'attesa del suo arrivo, rigorosamente dopo mezzogiorno, solo per prenderlo in giro, arrivando addirittura a coniare un nuovo modo per dire arrivare-schifosamente-tardi-per-poi-non-fare-nulla-fino-a-pranzo-e-abbioccarsi-con-la-testa-sul-banco-fino-almeno-alle-tre, ovvero *arrivare alla Diego*. Ecco, grazie a Diego ho capito che esistono ancora persone di cui ci si possa fidare, che a volte bisogna fidarsi un po' più di sé stessi e che alla fine andrà tutto bene, pur arrivando schifosamente-tardi-per-poi-non-fare-nulla-fino-a-pranzo-e-abbioccarsi-con-la-testa-sul-banco-fino-almeno-alle-tre. Ho anche capito

che studiare con lui quasi ventiquattr'ore su ventiquattro in patio nutrendosi solo di patatine alla pizza e biscotti al burro non fa bene al cervello e allo stomaco, ma forse un pochino all'anima sì.
Non sono mai stata una persona particolarmente socievole e Firas lo sa bene. Grazie a lui in questi ultimi due anni un po' di cose sono cambiate, la mia tolleranza all'alcool, no. Mi piace pensare che sia stato il mio regalo di compleanno, quella sera di fine ottobre in cui nemmeno lo conoscevo, cercavo solo un po' di vino rosso e invece ho trovato un amico che mi ha insegnato l'arte della condivisione. Poche cose sono certe nella vita, e una di queste è sicuramente la presenza nel suo frigo di una birra fresca che condividerà volentieri con te, non dopo aver perso una partita a carte (anche se continuerà a negare fino alla morte che sia successo). E ad ogni birra guadagnata corrisponde inevitabilmente un po' di dignità persa per le strade di Isola, ma anche nuovi amici, come Guido, che quella sera con la luna rossa è entrato nella mia vita in circostanze... originali. Con lui ho capito che non esistono davvero limiti a ciò che si può fare o desiderare, basta solo non lasciare che qualcun altro decida per te.
Ho anche imparato ad essere paziente, ad aspettare e a non indugiare nelle cose davvero importanti. Probabilmente quest'attesa non finirà mai, ma non è questo ciò che importa davvero.
Perché la passione non si piega alle leggi della ragione, non si cura minimamente di quello che riceverà in cambio, vuole esprimersi fino in fondo, imporre la sua volontà, anche se in cambio non ottiene altro che sentimenti mansueti, amicizia e indulgenza. Ogni vera passione è senza speranza, altrimenti non sarebbe una passione ma un semplice patto, un accordo ragionevole, uno scambio di banali interessi.
L'ultimo ringraziamento va ad Araki, artista che ha saputo ispirarmi, guidarmi, ed insegnarmi ad esprimere anche la parte più nascosta di me, in un modo e in un luogo che solo noi conosciamo e che nessun altro capirà, come quando scopri, in una vecchia cantina piena di cianfrusaglie ed oggetti di poco conto, uno scatto prezioso che non sapevi esistesse ed invece è lì, a sbatterti in faccia ciò che sei davvero. Nell'atto dell'amore, come in fotografia, c'è una forma di vita e una specie di morte lenta.

E dopo tutti questi uomini e citazioni colte ci vuole un po' di sana ignoranza, quindi, come direbbe un mio caro amico... *sku sku!*

Chiara

"The internal combustion engine will survive us all"

-Bertel Schmitt-

Contents

List of Figures

Sommario

L'obiettivo di questa tesi è dimostrare che l'applicazione del ciclo Atkinson-Miller ad un moderno motore ad accensione comandata aspirato, possa ridurne il consumo specifico di combustibile, e quindi migliorarne l'efficienza ai carichi parziali, rappresentanti le più comuni condizioni operative di un motore per applicazioni automobilistiche.
In primo luogo, è stato passato in rassegna l'attuale stato dell'arte dei motori basati sui cicli Atkinson e Miller, e le loro analogie e differenze sono state illustrate. Inoltre, sono state descritte delle possibili realizzazioni meccaniche dei cicli sovraespansi, evidenziandone le fondamentali criticità e fornendo degli spunti sulla loro applicazione in campo reale.
Dopo aver concluso con successo la fase di validazione del motore ad accensione comandata aspirato Alfa Romeo 2.0 16V in esame, sono stati analizzati gli effetti derivanti dall'applicazione delle strategie LIVC/EIVC attraverso un confronto tra il ciclo Otto di base ed il ciclo Atkinson-Miller. L'analisi si è focalizzata sui maggiori indicatori in termini di qualità delle prestazioni di un motore: consumo specifico di combustibile ed efficienza globale.
In ultima istanza, è stato aumentato il rapporto di compressione geometrico dei cilindri come ulteriore intervento per il miglioramento delle prestazioni. I dati su cui si è basta questa analisi sono i risultati di simulazioni eseguite tramite *Gasdyn*, un codice di calcolo monodimensionale sviluppato presso il Dipartimento di Energia del Politecnico di Milano.

Parole chiave: modello monodimensionale, motore ad accensione comandata, ciclo Atkinson-Miller, LIVC, EIVC, carichi parziali, consumo specifico di combustibile, efficienza globale, GCR.

Abstract

The aim of this thesis is to prove that the application of Atkinson-Miller cycle to a modern naturally aspirated SI engine can improve fuel economy and total efficiency during part load operations that are actually the most common working conditions of a city car engine.
First of all, a critical review of current state-of-the-art research on ACE and MCE is provided. Their similarities and differences are clarified. An in-depth description of the mechanical realizations for the over-expansion cycle is made; crucial challenges are pointed out and general recommendations on real applications are given.
After a successful validation of the 2.0 16V Alfa Romeo SI engine, an analysis of the outcomes of the LIVC/EIVC strategies' application is carried out. It consisted in the comparison between the baseline Otto cycle and the Atkinson-Miller cycle, focusing on BSFC and total efficiency, the main indicators of engine performance quality.
Moreover, an investigation on the possible improvements given by an increase of the geometrical compression ratio of the engine is performed.
The data upon which this analysis is based, are the outputs resulting from the simulations made by *Gasdyn*, a one-dimensional simulation code developed by the Internal Combustion Engine Team of the Energy Department of Politecnico di Milano.

Keywords: one-dimensional model, SI engine, Atkinson-Miller cycle, LIVC, EIVC, part load, BSFC, total efficiency, GCR.

Introduction

In 1882, an English engineer named James Atkinson invented the first Atkinson Cycle Engine. The original ACE, with a long expansion stroke and short intake and compression strokes, was realized with a complex linkage mechanism. High thermal efficiency of the original ACE was achieved at the expense of reduced power density and increased complexity. Minimal attention from the automotive industry was focused on the ACE for several years. In recent years, ACEs realized via VVT technology have been widely applied in hybrid vehicles. Increasing studies involving ACEs have been published.

A shortage of energy sources and climate warming have attracted global attention and become a severe problem that impacts the sustainable development of humans.

Greenhouse gases (GHGs) are a main factor leading to global climate warming. Reducing the GHGs and harmful emissions (NO_x, HC, etc.) from the transport sector, especially from vehicles, is a key factor that eliminates the climate change risk. Vehicle emissions are also the main contributor leading to haze and photochemical smog. Fossil fuels are the main energy source, but these have finite reserves. It is particularly crucial to decrease the degree of vehicle dependence on fossil fuels. Developing new energy resources and significantly enhancing the energy efficiency of the conventional ICE are both effective paths and are also necessary to control GHGs and harmful emissions.

The conventional ICE technology is thought to be approaching its development limit. However, the ICE technology is far from its development plateau. Much effort is being made to improve the fuel efficiency and reduce harmful emissions.

As the global amount of automobiles increases, the EPA's (Environmental Protection Agency) analysis shows that an annual reduction of 5–6% of GHGs is necessary to achieve the targets: 95 g/km for 2020, 70–75 g/km for 2025, and 50–55 g/km for 2030.

The 2020 target can be realized through advanced ICE technology while

further targets must depend on vehicle electrification (pure electric and hybrid vehicles).
The primary problems of an electric vehicle (EV) are: low battery energy density, thus a short range; long charging time; short battery cycle life; and high cost. A joint report by the EPA, CARB (California Air Resources Board) and NHTSA (National Highway Traffic Safety Administration) shows that the conventional vehicle technologies are more cost effective than any of the other technology options.
Moreover, if the upstream electricity generation and distribution are considered in the overall life cycle, the advantages of an EV, including energy savings and emissions reductions, will decrease. In this situation, the ICE-based vehicles (including a substantial portion of hybrid electric vehicles) tend to be superior in terms of fuel consumption and GHG emissions.
Therefore, the ICE still has significant potential for energy savings and emissions reduction.
An ICE in a hybrid vehicle is so crucial that it considerably determines the vehicle fuel consumption and emissions.
If the hybrid vehicle adopts an over-expansion Atkinson cycle SI engine as one of primary power sources, significant reduction in fuel consumption can be achieved. Yoshiharu Yamamoto stated that, "If we hit the 45% efficiency mark, the ICE will long remain a worthy being.". One possible way to increase the efficiency of ICEs is the usage of the Atkinson cycle.
In addition to the ACE described above, Miller Cycle Engine (MCE) is another type of over-expansion cycle engine patented in 1947 by an American engineer named Ralph Miller. ACE is usually naturally aspirated while MCE is supercharged but they are basically the same from a thermodynamic point of view.
The ACE is controlled to cross over the low BSFC region. Under a low load, the engine is cut off while the driven motor is working to propel the vehicle. As the load increases, the engine begins to work. If the engine output power is excessive, mechanical energy from the engine is split into two parts: a part used to propel the wheel and another part used to propel the generator to produce electricity that is stored in battery pack. When running a high load or with high speed, if the required power exceeds the engine efficient power or the maximum value, the driven motor can provide the leaving power. The reduced power density for ACE can be compensated by the driven motor. Therefore, ACE/MCE is the most suitable for hybrid vehicles.
The preliminary step in the construction of such engines consists in a study of the complex fluid-dynamics of an internal combustion engine by means of one-dimensional simulation tools that makes it possible to save time

and economic resources. The results of this thesis are provided by Gasdyn, a one-dimensional simulation tool developed by the Internal Combustion Engine (ICE) Group of the Energy Department of Politecnico di Milano. This tool is crucial in the prediction of the effects of the application of these thermodynamic cycles (ACE/MCE) to a baseline Otto cycle, pointing out the most successful actions in terms of fuel economy and total efficiency improvements.

Chapter 1

Governing Equations and Numerical Methods

1.1 Introduction

Internal combustion engines are classified as volumetric machines, hence they are characterized by unsteady flow at both inlet and outlet section requiring mathematical models able to properly reproduce such wave motions.
The first chapter of this thesis aims to present the governing equations with their simplifying hypotheses and the numerical methods implemented in Gasdyn, specifically the finite volume 3D Cell Method and the finite differential Total Variation Diminishing Method developed by Corberan and Gascòn (CG-TVD).
Finally, the boundary problem is introduced.

1.2 Governing equations

The cyclic opening and closing of the engine valves produces important pressure and velocity variations in the fluid moving through the ducts and inside the cylinders resulting in an overall strongly unsteady process: temperature and entropy gradients are so significant that the fluid shows high viscosity and compressibility.
Such behavior can be conveniently described by the 3D Navier-Stokes equations complemented by empirical laws relating the dependence of viscosity and thermal conductivity to the remaining flow variables and thermodynamic state relationships.
The complexity of this approach and the huge computational time required

to run this type of simulations has led to the development of 1D models based on the following assumptions:

- **Unsteady flow**;
- **Compressible fluid**: the ideal gas mixture model (specific heats variable with temperature and chemical composition) or the perfect gas model (constant specific heat) is adopted;
- **One-dimensional flow**: the length to diameter ratio $\frac{L}{D}$ of the pipes is high enough to assume the flow to be fully developed turbulent, consequently the longitudinal components of the fluid-dynamical quantities (pressure p, fluid velocity u, density ρ) can be considered constant within the cross-section and prevailing over the transversal ones;
- **Variable cross section**: small variations of the cross-section area F along the longitudinal direction x;
- **Non-adiabatic process**: the heat flux through the walls is not negligible;
- **Non-isentropic flow**: viscous forces are not negligible.

Considering Figure 1.1 and adopting the Eulerian approach, the continuity, momentum and energy equations can be written for the control volume defined by the dotted line.

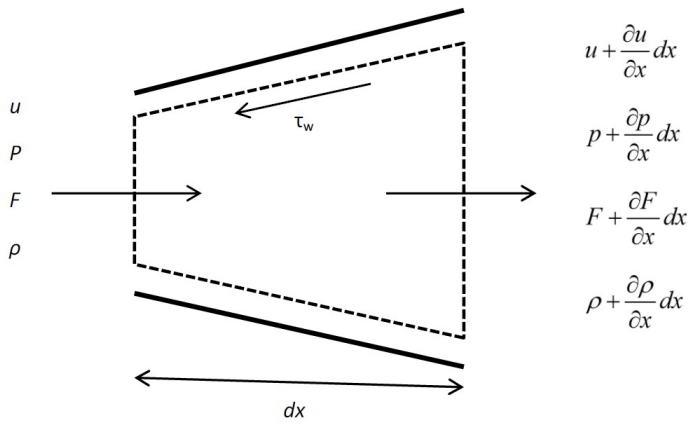

Figure 1.1: Control volume for variable area flow.

Continuity equation The net flow rate at the outlet of the control volume equals the decrease in mass of the control volume:

$$\left(\rho + \frac{\partial \rho}{\partial x}dx\right)\left(u + \frac{\partial u}{\partial x}dx\right)\left(F + \frac{\partial F}{\partial x}dx\right) - \rho u F = -\frac{\partial}{\partial t}(\rho F dx) \tag{1.1}$$

Considering only first order small quantities and rearranging:

$$\frac{\partial \rho}{\partial t} + \rho\frac{\partial u}{\partial x} + u\frac{\partial \rho}{\partial x} + \frac{\rho u}{F}\frac{dF}{dx} = 0 \tag{1.2}$$

$$\frac{\partial \rho}{\partial t} + \frac{\partial}{\partial x}(\rho u) + \frac{\rho u}{F}\frac{dF}{dx} = 0 \tag{1.3}$$

Momentum equation The resultant of pressure and shear forces on the control surface equals the sum of the rate of change of momentum within the control volume and the net flux of momentum across the control surface.
Pressure forces:

$$pF - \left(p + \frac{\partial p}{\partial x}dx\right)\left(F + \frac{dF}{dx}dx\right) + p\frac{dF}{dx}dx = -\frac{\partial}{\partial x}\left(pF\right)dx + p\frac{dF}{dx}dx \tag{1.4}$$

All forces are assumed to be positive according to the x-direction. The first two terms represent the pressure on the end sections while the third one is the pressure component along the x-direction acting on the lateral surface of the control volume.
Shear forces:

$$-\tau_w \pi D dx = -f\frac{\rho u^2}{2}\pi D dx \tag{1.5}$$

Where:

- D, equivalent diameter;
- τ_w, wall shear stress;
- f, friction factor;

Rate of change of momentum:

$$\frac{\partial}{\partial t}(\rho u F)dx \tag{1.6}$$

Net flux of momentum from control surface considering only first order small quantities:

$$\left(\rho + \frac{\partial \rho}{\partial x}dx\right)\left(u + \frac{\partial u}{\partial x}dx\right)^2\left(F + \frac{dF}{dx}dx\right) - \rho u^2 F = \frac{\partial}{\partial x}(\rho u^2 F)dx \tag{1.7}$$

Hence, the momentum equation is:

$$-\frac{\partial}{\partial x}(pF)\,dx + p\frac{dF}{dx}dx - f\frac{\rho u^2}{2}\pi D dx = \frac{\partial}{\partial t}(\rho u F)\,dx + \frac{\partial}{\partial x}(\rho u^2 F)dx \tag{1.8}$$

Expanding, dividing by F and rearranging the previous equation:

$$u\left(\frac{\partial \rho}{\partial t} + \rho\frac{\partial u}{\partial x} + u\frac{\partial \rho}{\partial x} + \frac{\rho u}{F}\frac{dF}{dx}\right) + f\frac{\rho u^2}{2}\frac{4}{D} + \frac{\partial p}{\partial x} + \rho\frac{\partial u}{\partial t} + \rho u\frac{\partial u}{\partial x} = 0 \tag{1.9}$$

The first term is identically zero from 1.2, so 1.9 becomes:

$$\frac{\partial u}{\partial t} + u\frac{\partial u}{\partial x} + \frac{1}{\rho}\frac{\partial \rho}{\partial x} + G = 0 \tag{1.10}$$

Where:

$$G = f\frac{u^2}{2}\frac{u}{|u|}\frac{4}{D} \tag{1.11}$$

Energy equation The energy equation can be derived by applying the First Law of Thermodynamics to the control volume as follows:

$$\dot{Q} - \dot{W_S} = \frac{\partial E_0}{\partial t} + \frac{\partial H_0}{\partial x}dx \tag{1.12}$$

Looking at the terms in detail:

$$E_0 = \frac{\partial(e_0 \rho F)}{\partial t}dx \tag{1.13}$$

is the total stagnation internal energy, where the specific stagnation internal energy is defined as $e_0 = e + \frac{1}{2}u^2$ and

$$H_0 = \frac{\partial(h_0 \rho u F)}{\partial x} dx \tag{1.14}$$

is the net outflow of stagnation enthalpy across the control surface, where the specific quantity h_0 is related to e_0 by the following expression:

$$h_0 = e_0 + \frac{p}{\rho} \tag{1.15}$$

Assuming that the heat transfer is positive if flowing into the control volume, the total heat transfer rate from/to the control volume is:

$$\dot{Q} = q\rho F dx + q_{HR} F dx \tag{1.16}$$

Where:

- q, heat transfer rate per unit time per unit mass of gas;
- $q_H R$, heat released per unit volume per unit time by possible chemical reactions in the exhaust manifold.

The work done by/on the system $\dot{W}_S$ is zero for a gas flowing into a pipe element of an engine manifold.
Finally, the energy equation can be written as:

$$q\rho F dx + q_{HR} F dx = \frac{\partial(e_0 \rho F)}{\partial t} dx + \frac{\partial(h_0 \rho u F)}{\partial x} dx \tag{1.17}$$

It is now possible to summarize the governing equations for the one-dimensional flow of a compressible fluid in a pipe with variable cross section, wall friction and heat transfer in a set of non-linear hyperbolic partial differential equations:

$$\begin{cases} \frac{\partial \rho}{\partial t} + \frac{\partial}{\partial x}(\rho u) + \frac{\rho u}{F}\frac{dF}{dx} = 0 \\ \frac{\partial u}{\partial t} + u\frac{\partial u}{\partial x} + \frac{1}{\rho}\frac{\partial \rho}{\partial x} + G = 0 \\ q\rho F dx + q_{HR} F dx = \frac{\partial(e_0 \rho F)}{\partial t} dx + \frac{\partial(h_0 \rho u F)}{\partial x} dx \end{cases} \tag{1.18}$$

These three equations contain four unknowns ρ, u, p, and e, then a further

relationship is required to solve the problem. The properties of the gas must be related by a state equation, in this case the ideal gas state equation is sufficiently accurate. Moreover, if the fluid is considered a perfect gas the internal energy can be expressed as the product of specific heat capacity at constant volume c_v and temperature T. Here there are the two equations aforementioned:

$$\frac{p}{\rho} = RT \tag{1.19}$$

$$e = c_v T \tag{1.20}$$

It is now possible to rewrite the energy equation 1.17 as:

$$q\rho F dx + q_{HR} F dx = \frac{\partial}{\partial t}\left[(\rho F dx)\left(c_v T + \frac{u^2}{2}\right)\right] + \frac{\partial}{\partial x}\left[(\rho u F)\left(c_v T + \frac{p}{\rho} + \frac{u^2}{2}\right)\right] dx \tag{1.21}$$

Rearranging the 1.21 with the continuity and momentum equations 1.3, 1.10:

$$\left(\frac{\partial p}{\partial t} + u\frac{\partial p}{\partial x}\right) - a^2\left(\frac{\partial \rho}{\partial t} + u\frac{\partial \rho}{\partial x}\right) - \rho\,(k-1)\left(q + \frac{q_{HR}}{\rho} + uG\right) = 0 \tag{1.22}$$

Where:

- $a = \sqrt{kRT}$, speed of sound;
- $k = \frac{c_p}{c_v}$, ratio of specific heats.

The traditional Method of Characteristics is based on the *non-conservative form* of these equations:

$$\begin{cases} \frac{\partial \rho}{\partial t} + \rho\frac{\partial u}{\partial x} + \frac{\rho u}{F}\frac{dF}{dx} = 0 \\ \frac{\partial u}{\partial t} + u\frac{\partial u}{\partial x} + \frac{1}{\rho}\frac{\partial \rho}{\partial x} + G = 0 \\ \left(\frac{\partial p}{\partial t} + u\frac{\partial p}{\partial x}\right) - a^2\left(\frac{\partial \rho}{\partial t} + u\frac{\partial \rho}{\partial x}\right) - \rho\,(k-1)\left(q + \frac{q_{HR}}{\rho} + uG\right) = 0 \end{cases} \tag{1.23}$$

Anyway, they can be expressed in a *conservative form* that preserves the

properties of the fluid in a pipe with varying cross-sectional area:

$$\begin{cases} \frac{\partial(\rho F)}{\partial t} + \frac{\partial(\rho u F)}{\partial x} = 0 \\ \frac{\partial(\rho u F)}{\partial t} + \frac{\partial\left(\rho u^2 + p\right)F}{\partial x} - p\frac{dF}{dx} + \frac{1}{2}\rho u^2 f \pi D = 0 \\ \frac{\partial(\rho e_0 F)}{\partial t} + \frac{\partial(\rho h_0 F)}{\partial x} - q\rho F - q_{HR}F = 0 \end{cases} \tag{1.24}$$

With this formulation it is possible to describe the discontinuities in the flow. To write the conservative form it is necessary to identify the groups of variables conserved throughout the shocks and to collect them in a common differential operator.
This set of equations can be rewritten in symbolic vector form, useful for the application of the CG-TVD Method that will be explained later on. If the cross-sectional area is retained in differential terms, the governing equations become:

$$\frac{\partial \bar{W}(x,t)}{\partial t} + \frac{\partial \bar{F}(\bar{W})}{\partial x} + \bar{C}\left(\bar{W}\right) = 0 \tag{1.25}$$

(From this point forward, the cross-sectional area will be noted with the letter A instead of F to prevent the reader from confusing it with the components of the vector $\bar{F}\left(\bar{W}\right)$.)
Where the three vectors are:

- $\bar{W}\left(x,t\right) = \begin{bmatrix} \rho A \\ \rho u A \\ \rho e_0 A \end{bmatrix}$, vector of convective fluxes;
- $\bar{F}\left(\bar{W}\right) = \begin{bmatrix} \rho u A \\ \left(\rho u^2 + p\right) A \\ \rho u h_0 A \end{bmatrix}$, vector on the x-direction;
- $\bar{C}\left(\bar{W}\right) = \begin{bmatrix} 0 \\ -p\frac{dA}{dx} \\ 0 \end{bmatrix} + \begin{bmatrix} 0 \\ \rho G A \\ -(q\rho + q_{HR})A \end{bmatrix}$, vector of source terms (the first member contains the contributes of pressure force due to section variation, the second one represents the effects of friction and heat exchanges).

In a more compact form:

$$\bar{W}_t + \bar{F}\left(\bar{W}\right)_x = \bar{C}\left(\bar{W}\right) \tag{1.26}$$

As for the non-conservative equations, a state equation is required to solve the problem.
These are all the equations used by Gasdyn and solved with numerical methods such as the finite volume 3D Cell Method and the finite differential Total Variation Diminishing Method implemented by Corberan and Gascòn (CG-TVD).

1.3 Numerical methods

Since it is not possible to solve the hyperbolic partial differential equations derived in the previous paragraph analytically, proper numerical methods are required. Then, the governing equations must be discretized to form a set of algebraic relationships that can be solved numerically.
In 1858, Riemann found the first solution to this kind of problems developing the Method of Characteristics and introducing new computational perspectives that brought to more advanced numerical methods. Although the Method of Characteristics is a powerful tool for analyzing non-linear waves, it presents some limitations:

- Assumption of ideal gas;
- Assumption of linearity in the temporal domain of the solution when determining the value of physical properties of the fluid between two nodes of the mesh. It leads to a first order approximation that results insufficient for gas-dynamic computations;
- Inability to get the discontinuities in the solution such as shock waves distributed all over the mesh.

The Method of Characteristics remained the most diffused technique due to its simplicity and its physical approach to solve the hyperbolic problem until more accurate computational method were implemented.

1.3.1 The 3D Cell Method

Introduction

The 3D Cell is a finite volume numerical method developed specifically for silencers. It has an excellent ability to conserve the mass along the ducts, even when the section and the discretization of the geometry change. The goal is to create an architecture which allows a rapid simulation of the engine functioning without losing the geometric information. This is

possible thanks to the decomposition of the components into finite volumes, which keeps track of real dimensions without making computations too heavy.

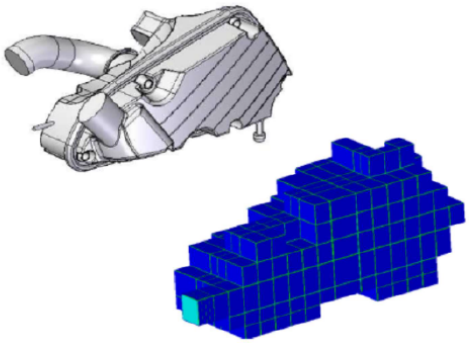

Figure 1.2: Simplified scheme of a complex geometry.

Theory of the numerical method

The grid of this method is composed by two fundamental elements: cells and ports. Every cell communicates with each other through ports in every space direction: in this way all the extensive characteristics, like mass and energy, and all the thermodynamic quantities are evaluated and associated to the same cells, whereas the fluxes to the ports, projecting them vectorially along the speed direction.

The Eulerian approach is adopted, therefore fluxes are not projected

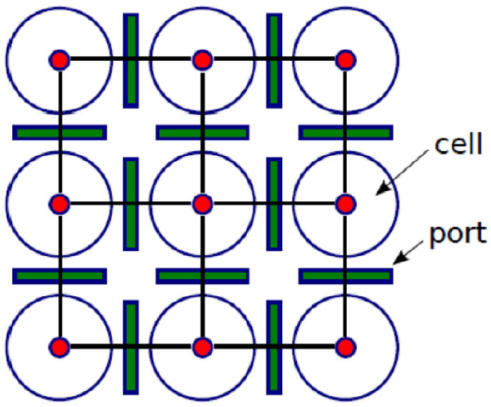

Figure 1.3: 3D Cell grid.

on every space direction, but on one coordinate only, along which the

balances are evaluated, keeping into account the geometry of the duct without making the numerical method too heavy. The heat transfer term is introduced for each cell as a function of the external surface connected to local diameter of the component. The pressure loss is a function of port diameter and length. The aim is to calculate the new variables within cells at time t_{n+1} for every timestep but a port balance is also necessary for following conservative balances. This implies that the fluxes are calculated using the information at time t_n of two adjacent cells, proceeding only half timestep $t_{n+1/2}$ at a time. Then the conservation of mass, momentum and energy inside each cell is evaluated through a port balance, obtaining values at time t_{n+1} . In this way the method reaches a second order accuracy both in space and time.

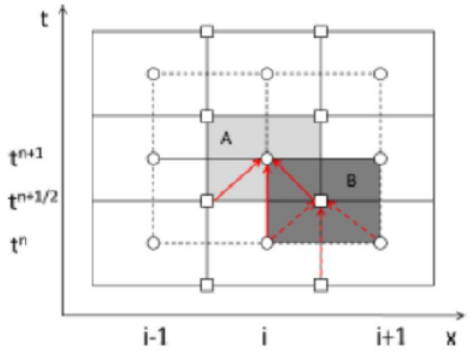

Figure 1.4: 3D Cell temporal structure.

Continuity equation Mass and energy balances are carried out for each cell, while momentum conservation is performed for ports only. A set of Eulerian equations is integrated over volume dV and time dt:

$$\int_t^{t+dt} (\frac{\partial}{\partial t} \int_V \rho dV + \int_V Div\,(\rho \mathbf{U})\, dV) dt = 0 \tag{1.27}$$

According to Gauss Theorem:

$$\int_V Div\,(\rho \mathbf{U})\, dV = \int_S (\rho \mathbf{U} \times n)\, dS \tag{1.28}$$

Resulting in:

$$\rho^{n+1} = \rho^n + \frac{1}{V} \sum_{p=1}^{N_{ports}} (\rho U A)_p^{n+1/2} \Delta t \tag{1.29}$$

The surface integral of mass transport through the cell becomes the summation of the mass flow rates through each face of the cell oriented according to **U** in space. The method is 1D, so the vector **U** has only one direction and the summation results in a simple difference between mass flow rates across left and right side of the cell. Computing directly the mass contained in every single cell instead of density, the equation becomes:

$$M_c^{n+1} = M_c + (FM_{p,Sx}^{n+\frac{1}{2}} - FM_{p,Dx}^{n+\frac{1}{2}})\Delta t \tag{1.30}$$

where FM are the mass fluxes on the left and right ports p of each cell c.

Energy equation Also energy balance is integrated over time and space:

$$\rho e^{n+1} = \rho e^n + \frac{1}{V}\sum_{p=1}^{N_{ports}} (\rho U h A)_p^{n+1/2}\Delta t + E_s \tag{1.31}$$

where E_s is associated to heat transfer (convective component), while enthalpy flux is defined as the product of mass flow rate and relative specific enthalpy h:

$$(\rho U h A)^{n+1/2} = (\rho U A)^{n+1/2} h \tag{1.32}$$

In this method the internal energy is preserved:

$$E_c^{n+1} = E_c^n + \left(FH_{p,Sx}^{n+\frac{1}{2}} - FH_{p,Dx}^{n+\frac{1}{2}}\right)\Delta t + Es \tag{1.33}$$

FH is the enthalpic flux and E_s is evaluated as:

$$E_s = \pi D_c \Delta x h conv(Twall - Tc) \tag{1.34}$$

- D_c , diameter and Δx length of the cell;
- h_{conv} , convective coefficient;
- T_{wall} , external temperature of the duct;
- T_c , temperature of the cell.

Momentum equation This balance is carried out for ports only. Keeping into account the 1D approximation and integrating it over time and space, the following equation is obtained:

$$\rho U A_p^{n+1/2} = \rho U A_p^{n-1/2} + \frac{\Delta t}{\Delta x}\left(\left(\rho U^2 + p\right)_{c,Sx}^{n} - \left(\rho U^2 + p\right)_{c,Dx}^{n}\right) A_p + M_s \tag{1.35}$$

- A_p , port area;
- $(\rho u^2 + p)$, momentum flux in every cell;
- M_s , source term collecting pressure losses and the method controlling diffusive term called *DTM* (Diffusion Source Term), that reduces oscillations of the solution without modifying the overall trend.

The pressure is evaluated by means of the perfect gas law, while velocity through the momentum Q_c:

$$U_c = \frac{\rho V_c \mathbf{U}}{\rho V_c} = \frac{Q_c}{M_c} \tag{1.36}$$

Generally, every port is weighed with respect to its distance from the cell center, evaluating every contribution according to the *U-component* entering the p-th face.

$$\rho U A_c^{n+1} = \rho U A_c^{n} + \sum_{p=1}^{N_{ports}} (\rho U A_p^{n+\frac{1}{2}}) \Delta x \times n_p \tag{1.37}$$

The contribution due to section variation along the direction of interest is also derived:

$$\int_{c,Sx}^{c,Dx} p dA = \int_{c,Sx}^{p} p dA + \int_{p}^{c,Dx} p dA \tag{1.38}$$

The pressure is constant form cell to cell by definition, so:

$$\int_{c,Sx}^{c,Dx} p dA = p_{c,Dx}\left(A_{c,Dx} - A_p\right) + p_{c,Sx}(A_p - A_{c,Sx}) \tag{1.39}$$

All the balances are carried out along one direction only, so everything is defined as a difference between port inlet and outlet, while the momentum of the cell is represented by the port mass flow rate

arithmetic average:

$$Q_c = \frac{1}{2}(FM_{p,Dx} + FM_{p,Sx})\Delta x_c \tag{1.40}$$

The definition of the generic port p mass flow rate is:

$$FM_p^{n+1} = FM_p^n + [\left(FQ_{c,Sx} - FQ_{c,Dx}\right) + p_{c,Dx}\left(A_{c,Dx} - A_p\right) + p_{c,Sx}\left(A_p - A_{c,Sx}\right)]\frac{\Delta t}{dx_p} + M_s \tag{1.41}$$

where FQ_c is the mechanical energy contribution of each cell.

CFL condition

In the simulation of any component, the choice of Δx depends on the size of the smallest element. Therefore, the choice of Δt is linked to Δx by the Courant-Friedrichs-Lewy (*CFL*) criterion. Practically, for every geometric element the maximum information propagation speed is defined as the sum of the speed of sound and its velocity. Dividing Δx by the information propagation speed, some times are obtained and the smallest will be chosen among them.

$$\Delta t_c = \frac{\Delta x_c}{a_c + |U_c|} \tag{1.42}$$

Where a_c is the speed of sound of the fluid in the cell.
At this point *CFL* is used as stability criterion: it is not used Δt_c directly, but a fraction of it

$$\upsilon = \frac{\Delta t_{final}}{\min(\Delta t_c)} with\ \upsilon < 1 \tag{1.43}$$

CFL is always < 1 in order to be conservative.

1.3.2 The Corberan-Gascòn Method (CG-TVD)

The CG-TVD method was developed by J.M. Corberan and M.L. Gascòn in 1994. It is a symmetrical finite differential Total Variation Diminishing Method that extends the classical Lax-Wendroff scheme and

conserves average mass flow rate from node to node in the most accurate way possible (second or even first order accuracy).

Mathematical model

The application of the CG-TVD method to internal combustion engines starts from the definition of the governing equations for a one-dimensional, unsteady, non-homeotropic flow in a variable geometry duct in vectoral form already presented in the previous section.
Considering the 1.26:

$$\bar{W}_t + \bar{F}\left(\bar{W}\right)_x = \bar{C}\left(\bar{W}\right)$$

Where the three vectors are:

- $\bar{W}(x,t) = \begin{bmatrix} \rho A \\ \rho u A \\ \rho e_0 A \end{bmatrix}$, vector of convective fluxes;
- $\bar{F}\left(\bar{W}\right) = \begin{bmatrix} \rho u A \\ \left(\rho u^2 + p\right) A \\ \rho u h_0 A \end{bmatrix}$, vector in x-direction;
- $\bar{C}\left(\bar{W}\right) = \begin{bmatrix} 0 \\ \rho G A - p A' \\ -(q\rho + q_{HR})A \end{bmatrix}$, vector of source terms (the first member contains the contributes of pressure force due to section variation, the second one represents the effects of friction and heat exchanges).

Then the system is completed by the hypothesis of perfect gas expressed as:

$$e_0 = \rho\frac{u^2}{2} + \frac{p}{k-1} \tag{1.44}$$

This method departs from LW formulation in the definition of the vector of the fluxes $\bar{W}(x,t)$ by substituting some components with some of the vector $\bar{F}\left(\bar{W}\right)$. This adjustment emphasizes the conservation of local and global mass flow rate, making this method particularly convenient whenever source terms (especially those linked to section variations which have the biggest impact on flow rate conservation) are not negligible and actually characterize the solution.

The Jacobian matrix of the flux function is defined as:

$$\mathbf{J} = \begin{bmatrix} 0 & 1 & 0 \\ \frac{k-3}{2}u^2 & (3-k)\,u & k-1 \\ u\left(\frac{k-1}{2}u^2 - H\right) & H-(k-1)u^2 & ku \end{bmatrix} \tag{1.45}$$

Where:

- $H = \frac{a^2}{k-1} + \frac{u^2}{2}$, total enthalpy;
- $a = \sqrt{kRT}$, speed of sound.

J is a strictly hyperbolic matrix that presents three real eigenvalues:

$$\alpha^z = \begin{bmatrix} u-a \\ u \\ u+a \end{bmatrix} \tag{1.46}$$

The matrix **P** is composed by the corresponding right eigenvectors:

$$\mathbf{P} = \left(\bar{P}^1, \bar{P}^2, \bar{P}^3\right) = \begin{bmatrix} 1 & 1 & 1 \\ u-a & u & u+a \\ uH-ua & \frac{u^2}{2} & H+ua \end{bmatrix} \tag{1.47}$$

The problem is hyperbolic, hence **P** diagonalizes **J** according to the following expression:

$$\mathbf{QJP} = diag\,(u-a,\ u,\ u+a) \tag{1.48}$$

where $\mathbf{Q} = \mathbf{P}^{-1}$ is the inverse matrix of **P** made up of the left eigenvalues of **J**:

$$\mathbf{Q} = \mathbf{P}^{-1} = \begin{bmatrix} -\frac{u}{2a} + \frac{k-1}{4}\frac{u^2}{a^2} & -\frac{1}{2a} - \frac{k-1}{2}\frac{u}{a^2} & \frac{k-1}{2a^2} \\ 1 - \frac{k-1}{2}\frac{u^2}{a^2} & (k-1)\frac{u}{a^2} & -\frac{k-1}{a^2} \\ -\frac{u}{2a} - \frac{k-1}{4}\frac{u^2}{a^2} & \frac{1}{2a} - \frac{k-1}{2}\frac{u}{a^2} & \frac{k-1}{2a^2} \end{bmatrix} \tag{1.49}$$

The numerical progression is solved through the following scheme:

$$W_j^{n+1} = W_j^n - \lambda\left(G^{TVD}_{j+\frac{1}{2}} - G^{TVD}_{j-\frac{1}{2}}\right) - \lambda\left[B_{j-\frac{1}{2},j} - B_{j,j+\frac{1}{2}}\right] \tag{1.50}$$

Where:

$$G^{TVD}_{j+\frac{1}{2}} = \frac{1}{2}\left\{F_j + F_{j+1} - B_{j,j+\frac{1}{2}} + B_{j+\frac{1}{2},j+1} - P_{j+\frac{1}{2}} h\left(\lambda \bar{D}_{j+\frac{1}{2}}\right) Q_{j+\frac{1}{2}} \left(F_{j+1} - F_j + B_{j,j+1}\right)\right\} + P_{j+\frac{1}{2}} \bar{\psi}_{j+\frac{1}{2}} \tag{1.51}$$

And the components of the vector $\bar{\psi}_{j+\frac{1}{2}}$ are defined as:

$$\varphi^k_j = s^k_{j+\frac{1}{2}} max\left\{0,\ min\left\{\left|\bar{\varphi}^k_{j+\frac{1}{2}}\right|,\ \ s^k_{j+\frac{1}{2}}\bar{\varphi}^k_{j-\frac{1}{2}},\ \ \ s^{\ k}_{j+\frac{1}{2}}\bar{\varphi}^k_{j+\frac{3}{2}}\right\}\right\} \tag{1.52}$$

Where $\bar{\varphi}^k_{j+\frac{1}{2}}$ represents the second order contributions vector:

$$\bar{\varphi}^k_{j+\frac{1}{2}} = \frac{1}{2}\left(h(\lambda \bar{D}_{j+\frac{1}{2}}) - \lambda \bar{D}_{j+\frac{1}{2}}\right) Q_{j+\frac{1}{2}} + \left(F_{j+1} - F_j + B_{j,j+1}\right) \tag{1.53}$$

$\mathbf{h}(\mathbf{x})$ is a matrix computed as:

$$h(\lambda \bar{D}_{j+\frac{1}{2}}) = diag\left(sign\left(\lambda \alpha^z_{j+\frac{1}{2}} + \lambda \beta^z_{j+\frac{1}{2}}\right)\right)_{z=1,2,3} \tag{1.54}$$

In particular:

$$\alpha^1 = u - a, \alpha^2 = u, \alpha^3 = u + a \tag{1.55}$$

While:

$$\begin{aligned}
\beta^1 &= \frac{\left(\frac{1}{2a} + \frac{k-1}{2}\frac{u}{a^2}\right)\left(pA'(x) - \rho G A\right) - \frac{k-1}{2a^2}\left(\rho \dot{q} A\right)}{-\frac{1}{2a}\rho A \frac{\partial u}{\partial x} + \frac{1}{2a^2}\frac{\partial (pA)}{\partial x}} \\
\beta^2 &= \frac{(1-k)\,\frac{u}{a^2}\left(pA'(x) - \rho G A\right) - \frac{1-k}{a^2}(\rho \dot{q} A)}{\frac{\partial (\rho A)}{\partial x} + \frac{1}{a^2}\frac{\partial (pA)}{\partial x}} \\
\beta^3 &= \frac{\left(-\frac{1}{2a} + \frac{k-1}{2}\frac{u}{a^2}\right)\left(pA'(x) - \rho G A\right) - \frac{k-1}{2a^2}\left(\rho \dot{q} A\right)}{\frac{1}{2a}\rho A \frac{\partial u}{\partial x} + \frac{1}{2a^2}\frac{\partial (pA)}{\partial x}}
\end{aligned} \tag{1.56}$$

If the denominator of β^z tends to zero, we can consider $\beta^z = 0$ and the propagation speeds are the corresponding characteristic speeds associated with the homogeneous flow.

A valid estimation of the source terms $B_{j,j+1}$ is the following:

$$B_{j,j+1} = \begin{bmatrix} 0 \\ -p_{j,j+\frac{1}{2}} \left(A_{j+1} - A_j\right) + (\Delta x)(\rho G A)_{j+\frac{1}{2}} \\ -(\Delta x)(\rho \dot{q} A)_{j+\frac{1}{2}} \end{bmatrix} \tag{1.57}$$

In the particular context of the quasi-one-dimensional unsteady flow through a duct with varying cross-section, it is important to distinguish between the approximations used for the term related to the variation of the pipe cross-sectional area, $pA'(x)$, and those used to approximate the terms related to the presence of friction forces and heat transfer at pipe walls, which are less important.
The term $pA'(x)$ should always be balancing the second component of the fluxes, therefore treated as a divergence term, as it really is because it represents the divergence of the surface forces over the lateral walls of the control volume. Consequently, it is important to approximate the integral of $pA'(x)$ between x_j and x_{j+1} as an expression of the form:

$$p_{j+\frac{1}{2}}(A_{j+1} - A_j) \tag{1.58}$$

Where $p_{j+\frac{1}{2}}$ represents some average of the pressure between p_j and p_{j+1}. In this thesis it has been adopted the arithmetical average for $p_{j+\frac{1}{2}}$, obtaining:

$$pA'(x) = \frac{(p_j + p_{j+1})}{2} \left(A_{j+1} - A_j\right) \tag{1.59}$$

Finally, the values of physical quantities in $x_{j+\frac{1}{2}}$ contained in the expression of source terms and in the matrices linked to $\mathbf{J}$ are defined. The Jacobian matrix is evaluated in-between two nodes of the mesh, and if its terms are not constant, they must be estimated with proper averaging techniques. The authors of the method suggest using Roe's linearization to obtain an average in the middle points for u, H, ρ and ρA:

$$
\begin{aligned}
u_{j+\frac{1}{2}} &= \frac{\chi_{j+\frac{1}{2}} u_{j+1} + u_j}{\chi_{j+\frac{1}{2}} + 1} \\
H_{j+\frac{1}{2}} &= \frac{\chi_{j+\frac{1}{2}} H_{j+1} + H_j}{\chi_{j+\frac{1}{2}} + 1} \\
\rho_{j+\frac{1}{2}} &= \sqrt{\rho_{j+1}\rho_j} \\
(\rho A)_{j+\frac{1}{2}} &= \sqrt{\rho_j A_j \rho_{j+1} A_{j+1}} \\
\chi_{j+\frac{1}{2}} &= \sqrt{\frac{\rho_{j+1} A_{j+1}}{\rho_j A_j}}
\end{aligned}
\tag{1.60}
$$

The authors recommend using $\rho_{j+\frac{1}{2}}$, $u_{j+\frac{1}{2}}$, $p_{j+\frac{1}{2}}$ and $T_{j+\frac{1}{2}}$ for the source terms vector too, nevertheless they affirm that there is not a significant difference in deriving it using a simple arithmetic average.

1.4 The boundary problem

The previous paragraphs have concentrated on methods of solving the equations of wave motion inside a pipe. It was stated that an important aspect of the overall calculation of flow in pipes was the interaction of the flow with the boundaries. Every pipe has two ends associated with it, and hence has two boundaries. There are various types of boundary and these must be simulated in a satisfactory manner: the best way to accurately incorporate the boundaries in all wave action techniques is by the Method of Characteristics. This is because the only way to get to the end of the pipe in a logical manner is to go along a wave, i.e. along a characteristic. Typical boundaries are: open ends, closed ends, inflow boundaries, valve boundaries, junctions (with or without pressure losses), pulse converters, orifices or valves in pipes, throttle bodies, turbines and compressors. The treatment of all these has one feature in common: the boundaries are all treated as if the flow is quasi-steady, this means that the characteristic of the boundary is not function of the frequency of the incident waveform. The assumption of *quasi-steady* flow implies that the physical size of the boundary can be neglected when compared with the length of the pipe connected to it and that the equations of steady flow can be applied locally to this infinitesimally small region. It also implies that at the boundary the rate of change of properties with distance is much greater than the rate of change with time, i.e. $\frac{\partial P}{\partial x} \gg \frac{\partial P}{\partial t}$, where P is any property.

1.4.1 Non-dimensional equations

These wave equations are based on the convention introduced by Benson, and a parameter a_A is introduced to define the entropy level in the duct. Figure 1.5 shows three isobars on an a-s diagram (equivalent to a T-s diagram) where a_A is the speed of sound which would be reached at the arbitrary reference pressure due to an isentropic change of state from the pressure p.

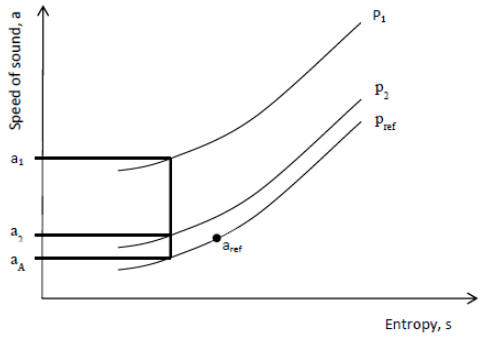

Figure 1.5: Isentropic processes depicted on a-s diagram.

For a perfect gas, obeying

$$\frac{p}{\rho^x} = const$$

The changes of state are given by

$$\frac{\rho}{\rho_A} = \left(\frac{p}{p_{ref}}\right)^{\frac{1}{x}} \tag{1.61}$$

$$\frac{p}{p_{ref}} = \left(\frac{a}{a_A}\right)^{\frac{2k}{(k-1)}} \tag{1.62}$$

Note that the quantity a_{ref} is arbitrarily fixed by defining a reference temperature T_{ref} with respect to the entropy level whereas the value of a_A varies and therefore reflects the entropy level in the duct.
Differentiating the last equations gives:

$$\frac{dp}{p} = \frac{2k}{k-1}\frac{da}{a} - \frac{2k}{k-1}\frac{da_A}{a} \tag{1.63}$$

$$\frac{d\rho}{\rho} = \frac{d\rho_A}{\rho} - \frac{1}{k}\frac{dp}{p} \tag{1.64}$$

Equation 1.63 shows that the change in pressure is no longer related only to the change in speed of sound but is affected by the change in the level of entropy defined by da_A.
Starting from the compatibility equations:

$$\begin{cases} \frac{1}{\rho a}dp + du + \frac{1}{\rho a}\left(\Delta_1 + \Delta_2 + \Delta_3\right)dt = 0 \\ \frac{1}{\rho a}dp - du + \frac{1}{\rho a}\left(\Delta_1 + \Delta_2 - \Delta_3\right)dt = 0 \\ dp - a^2 d\rho + \Delta_1 dt = 0 \end{cases} \tag{1.65}$$

Considering only the right-moving wave characteristic, the differential terms of the first equation of the set above can be replaced using the equations 1.63 and 1.64 to give:

$$\frac{2k}{k-1}da + du - \frac{2k}{k-1}a\frac{da_A}{a_A} - \frac{k-1}{a}\left(q + \frac{4f}{D}\frac{u^3}{2}\frac{u}{|u|}\right)dt + \frac{au}{F}\frac{dF}{dx}dt + \frac{4f}{D}\frac{u^2}{2}\frac{u}{|u|}dt \tag{1.66}$$

Defining the gas-dynamic non-dimensional quantities

$$A = \frac{a}{a_{ref}}, U = \frac{u}{a_{ref}}, A_A = \frac{a_A}{a_{ref}}, Z = \frac{a_{ref}t}{x_{ref}}, X = \frac{x}{x_{ref}}$$

Enables to rewrite the 1.66 as follows:

$$dA + \frac{k-1}{2}du = d\lambda \tag{1.67}$$

Where:

$$d\lambda = A\frac{dA_A}{A_A} - \frac{(k-1)}{2}\frac{AU}{F}\frac{dF}{dX}dZ - (k-1)\frac{f}{D}x_{ref}U^2\frac{U}{|U|}\left[1 - (k-1)\frac{U}{A}\right]dZ + \frac{(k-1)^2}{2}q\frac{x_{ref}}{a_{ref}^3}\frac{1}{A}dZ \tag{1.68}$$

The terms of the right-hand side of this equation, which define the change

of Riemann variable of the flow along the wave characteristic $\frac{dx}{dt} = u + a$, can be analysed as follows:

- Effect of the variation in the entropy level $\delta\lambda_{entropy} = A\frac{dA_A}{A_A}$;
- Effect of the pipe area variation $\delta\lambda_{area} = -\frac{(k-1)}{2}\frac{AU}{F}\frac{dF}{dX}dZ$;
- Effect of the pipe wall friction $\delta\lambda_{friction} = -(k-1)\frac{f}{D}x_{ref}U^2\frac{U}{|U|}\left[1-(k-1)\frac{U}{A}\right]dZ$;
- Effect of heat transfer $\delta\lambda_{heat_transfer} = \frac{(k-1)^2}{2}q\frac{x_{ref}}{a^3_{ref}}\frac{1}{A}dZ$.

Hence equation 1.68 can be expressed as:

$$d\lambda = \delta\lambda_{entropy} + \delta\lambda_{area} + \delta\lambda_{friction} + \delta\lambda_{heat-transfer} \tag{1.69}$$

Where the total change of the Riemann variable as it propagates across a mesh is the sum of the separate effects.
The change of Riemann variable along the wave characteristic $\frac{dx}{dt} = u - a$ can be expressed as:

$$dA - \frac{k-1}{2}du = d\beta \tag{1.70}$$

$$d\beta = A\frac{dA_A}{A_A} - \frac{(k-1)}{2}\frac{AU}{F}\frac{dF}{dX}dZ + (k-1)\frac{f}{D}x_{ref}U^2\frac{U}{|U|}\left[1+(k-1)\frac{U}{A}\right]dZ + \frac{(k-1)^2}{2}q\frac{x_{ref}}{a^3_{ref}}\frac{1}{A}dZ \tag{1.71}$$

$$d\beta = \delta\beta_{entropy} + \delta\beta_{area} + \delta\beta_{friction} + \delta\beta_{heat-transfer} \tag{1.72}$$

In the equations 1.68 and 1.71 the quantities A and U can be replaced by

$$\begin{aligned} A &= \frac{\lambda+\beta}{2} \\ U &= \frac{\lambda-\beta}{k-1} \end{aligned} \tag{1.73}$$

where the Riemann variables are evaluated at points L and R of Figure 1.6 respectively.

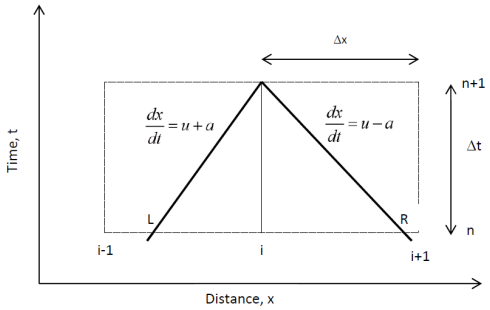

Figure 1.6: Homentropic characteristics shown on the position *(x-t)* diagram.

To calculate the value of dA_A along the pathline characteristic the last equation of 1.65 is used.

$$dA_A = \frac{(k-1)}{2}\frac{A_A}{A^2}\frac{x_{ref}}{a_{ref}^3}\left(q + \frac{2f}{D}a_{ref}^3\left|U^3\right|\right)dZ \tag{1.74}$$

In this case the entropy level depends only on the fiction and heat transfer contributions:

$$dA_A = \delta A_{friction} + \delta A_{heat-transfer} \tag{1.75}$$

1.4.2 Riemann variables at boundaries

The Riemann variables (invariants) are defined as:

$$\lambda = a + \frac{k-1}{2}u \tag{1.76}$$

$$\beta = a + \frac{k-1}{2}u \tag{1.77}$$

In this paragraph λ and β will be renamed λ_{in} and λ_{out} in order to represent waves which are approaching and leaving a boundary respectively. The Riemann variables will also be used in the dimensionless form using a reference condition for the speed of sound, a_{ref} to give:

$$A = \frac{\lambda_{in} + \lambda_{out}}{2} \tag{1.78}$$

$$U = \frac{\lambda_{in} - \lambda_{out}}{k-1} \tag{1.79}$$

1.4.3 Starred Riemann variables

It is also useful to introduce the concept of the starred Riemann variables, when examining non-homentropic flows. The only modification consists in dividing the Riemann variables by their entropy level. A general Riemann variable entering the boundary is then defined as:

$$\lambda^*_{in} = \frac{\lambda_{in}}{(A_A)_{in}} \tag{1.80}$$

While that leaving the boundary is:

$$\lambda^*_{out} = \frac{\lambda_{out}}{(A_A)_{out}} \tag{1.81}$$

This approach takes the change of entropy into the relevant parameter, the starred Riemann variable, and this is a useful method for dealing with non-homentropic flows.

1.4.4 Open end boundary

The main feature of a simple open end boundary is that the pressure at the exit of the pipe is equal to that outside the pipe. The effect of such a boundary is to invert an incident wave: thus, an incident compression wave is reflected as a rarefaction wave, and vice versa; it also results in an increase in the velocity at the end of the pipe. An example of this is shown in the isometric distance-time pressure diagram in Figure 1.7.

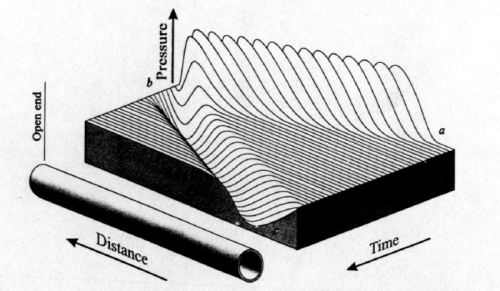

Figure 1.7: Wave reflection at an open end: an isometric illustration in the distance-time (x-t) plane.

The wave is introduced to the pipe at a and travels towards the open end at b. The compatibility condition for an open end is that the pressure must equal the atmospheric, or outside, pressure. This can only be achieved if a pressure wave is reflected as a rarefaction wave, and vice versa.

1.4.5 Closed end boundary

The important feature of a closed end boundary is that it does not transmit flow: hence the velocity at the end is zero. A wave reflected by interaction with a closed end is the same sense as the incident one. Hence a pressure wave is reflected as a pressure wave of equal magnitude. This occurs because there can be no flow at the closed end and hence the incident wave must be sent back into the pipe. The reflection is brought about by a reversal of momentum and the pressure (or force) must be increased to a higher level to achieve the wave reversal. This effect can be seen very clearly in Figure 1.8.

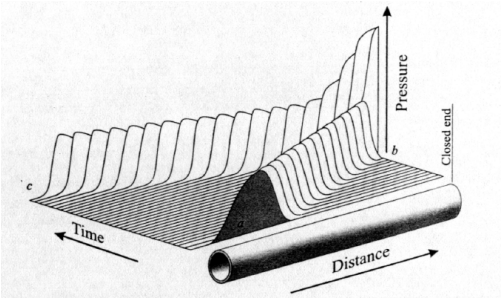

Figure 1.8: Wave reflection at a closed end: an isometric illustration in the distance-time (x-t) plane.

A pressure wave is introduced into the left-hand end of the pipe, at a. It travels along the pipe form left to right and reaches the closed end at b. The reflection of the wave results in an increase in the pressure acting on the closed end; this is caused by the reversal of the momentum of the wave. Hence the wave seems to "climb" over itself in reflecting back down the pipe.

Chapter 2

Overview on the Atkinson-Miller Cycle

2.1 Introduction

Vehicle electrification has to be addressed to reduce dependence on fossil fuels and meet future emission regulations. Pure electric vehicles still have many limitations, but hybrid vehicles are the optimum transference scheme. An over-expansion cycle (Atkinson or Miller) engine is the most suitable for hybrid vehicles.
Compared with a conventional Otto cycle engine, an over-expansion cycle engine can realize a larger expansion ratio and thus, a higher thermal efficiency while maintaining a normal effective compression ratio to avoid the knock.
Basics for the Atkinson and Miller cycles are introduced first. An analysis on mechanical realizations for the over-expansion cycle is conducted. Challenges for real applications of these mechanical realizations are presented. After a comprehensive review of the advantages and applications of the "Atkinson cycle effect" in load control, reducing NO_x formation and suppressing the knock, main problems are discussed and some solutions are provided.

2.2 Theoretical explanation of over-expansion cycles

The original ACE is a type of full-expansion cycle. Figure 2.1 presents the p-V and T-S diagrams comparison among the ideal Otto, Miller and

Atkinson cycles. 1–2–3–4O–1 is the Otto cycle process, and 1–2–3–4A–1 is the Atkinson cycle. For the Otto cycle, the expansion stroke equals the compression stroke. At the end of the power stroke, the in-cylinder pressure is obviously higher than the barometric pressure, meaning that working charges still have considerable potential to make useful work. While the Atkinson cycle fully expands to 4A with the in-cylinder pressure equal to the barometric pressure, more thermal energy (1–4O–4A–1) can be converted to useful mechanical work, resulting in higher thermal efficiency.

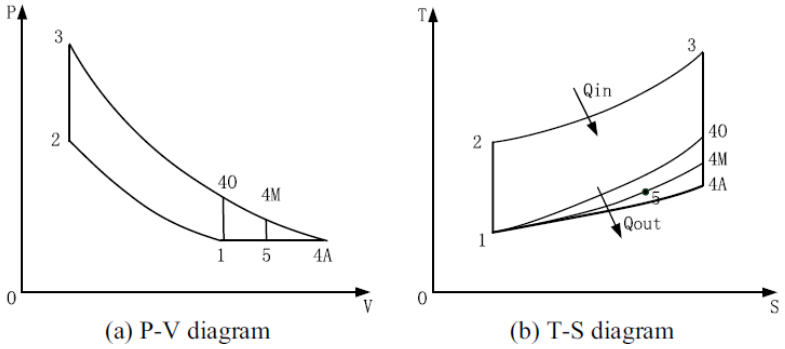

Figure 2.1: p-V and T-S diagrams for ideal Otto, Atkinson and Miller cycles.

2.2.1 Atkinson cycle vs. Miller cycle

Figure 2.1 shows the Miller cycle process (1–2–3–4M–5–1), which is an over-expansion cycle but does not expand to the barometric pressure. There is no doubt that the Atkinson cycle is more efficient than the Miller cycle because of the increased work output (5–4M–4A–5). However, in a practical ACE, the piston is not necessary for expansion to the barometric pressure. First, a long expansion stroke lengthens the cylinder body, increasing piston friction loss and engine weight. Then, low in-cylinder pressure at the end of the expansion stroke will lead to large exhaust pumping loss because there is not a free exhaust process when the exhaust valves open. This conversely discounts the thermodynamic merit of the full-expansion Atkinson cycle. Therefore, the cycle process in a practical ACE is closer to the ideal Miller cycle that is shown in Figure 2.1. Despite the fact that in-cylinder gas pressure at 4M is still higher than the barometric pressure, more thermal energy (1–4O–4M–5–1) is drawn from the working charges compared with the Otto cycle.
A real MCE generally uses LIVC (or EIVC) to realize the overexpansion

cycle such as in many modern ACEs. However, ACE is naturally aspirated while MCE is generally equipped with a super/turbocharger. Thus, the Miller cycle is essentially the same as the Atkinson cycle.

2.2.2 Thermodynamic analysis

Some assumptions were introduced in the thermodynamic model and some practical impact factors, such as the fuel vaporization and combustion process, were ignored. Figure 2.2 qualitatively demonstrates the effects of compression ratio CR, equivalence ratio Φ and expansion-to-compression ratio r on cycle efficiency. Within the entire effective range of CR, the cycle

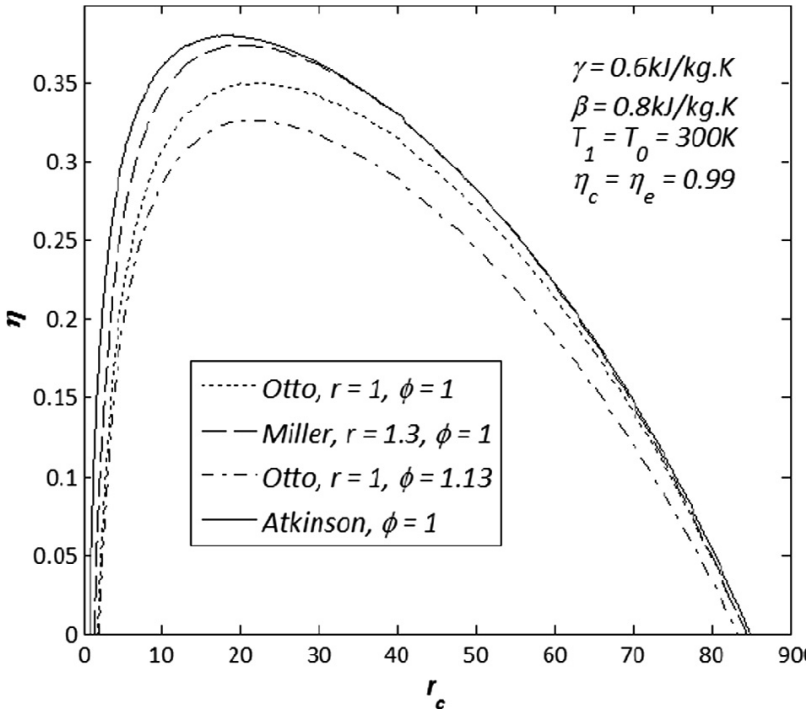

Figure 2.2: Effects of CR, r and Φ on cycle efficiency.

efficiency of the Atkinson cycle is always higher than the Otto and Miller cycles. However, as the CR increases, the efficiency differences decrease. There is an optimum CR approximately 20 that maximizes cycle efficiency of the Atkinson or Miller cycles. As the Φ increases, cycle efficiency of the Otto cycle obviously decreases.
According to formula:

$$T_{4a} = T_3 E R^{1-k}$$

for the Atkinson or Miller cycle engine, a higher expansion ratio contributes to lower in-cylinder temperature at the end of the expansion stroke, thus resulting in a lower exhaust temperature, as shown in Figure 2.1(b).
Some important thermodynamic characteristics for the over-expansion cycles have been summarized:

1. An over-expansion cycle has more work output and higher thermal efficiency than an Otto cycle at the same operating conditions;

2. There is an optimum compression ratio that maximizes the performances of Atkinson or Miller cycles. The effective power, power density and effective efficiency increase up to an optimum value and then start to decrease with increasing compression ratio. The effective power and effective efficiency increase with increasing cycle temperature ratio, cycle pressure ratio and inlet pressure while decrease with increasing friction coefficient, inlet temperature and retarding angle of intake valve closing;

3. The equivalence ratio has a significant impact on engine performance. Under high or full loads, an Atkinson or Miller cycle engine can implement an equivalence ratio equal or closer to 1, compared with an Otto cycle engine. The combustion efficiency increases, and the fuel economy is greatly improved;

4. Partial load efficiency of the over-expansion cycle with the largest feasible expansion ratio is the highest.

2.3 Methods for realizing the Atkinson cycle

This section mainly studies the types and mechanical realizations of the Atkinson cycle including the Miller cycle.

2.3.1 Atkinson cycle types

Figure 2.3 shows three types of Atkinson cycles:

1. The original Atkinson cycle is realized by fully expanding to the barometric pressure to draw the full working potential of in-cylinder working charges while the intake and compression strokes are the same as a normal Otto cycle. The engine, with less geometrical displacement V_D, has to be designed as a larger volume V_A for a long expansion stroke.

2. The Atkinson cycle is realized by retarding or advancing intake valve closure timing based on a normal Otto cycle: LIVC or EIVC. The expansion stroke is the same as the Otto cycle, while the effective compression stroke shortens. In this simple way, an over-expansion cycle is realized.

3. The expansion stroke length is the same as a normal Otto cycle, but a higher expansion ratio is realized by reducing dead volume V_{cc} as shown in Figure 2.3(b). LIVC or EIVC is carried out to realize the over-expansion cycle. The reduced ECR resulting from LIVC or EIVC can be compensated by the increased GCR. In this way, a greater efficiency improvement can be achieved.

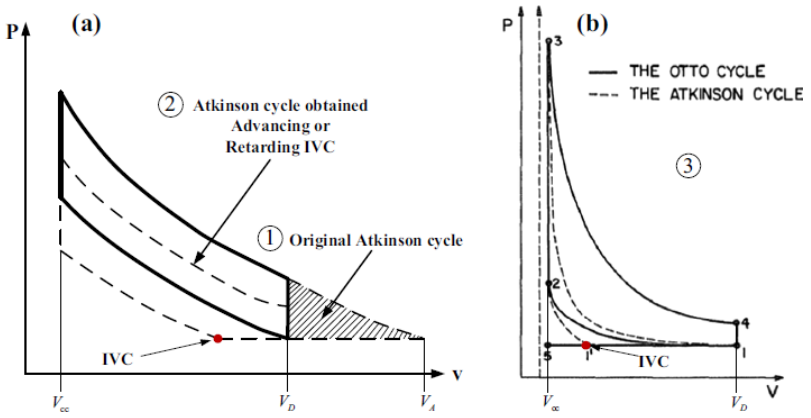

Figure 2.3: Three types of Atkinson cycle.

2.3.2 Mechanical realizations

Type 1 is the first practical ACE arranged as an opposed piston engine, the Atkinson differential engine. As shown in Figure 2.4(a), a single crankshaft was connected to two opposed pistons through a toggle jointed linkage that had a non-linearity. For half a revolution, one piston remained almost stationary while the other approached it and returned. Then, for the next half revolution, the pistons changed over which piston was almost stationary and which piston approached and returned. Thus, in each revolution, one piston provided a compression stroke and a power stroke, and the other piston provided an exhaust stroke and a charging stroke.
A later version, also designed by James Atkinson in 1887, is one of the most familiar ACE structures, as shown in Figure 2.4(b). The piston

is not directly connected to the crankshaft but is connected through a unique mechanical linkage. In this way, the engine could implement longer expansion and exhaust strokes than its intake and compression strokes.

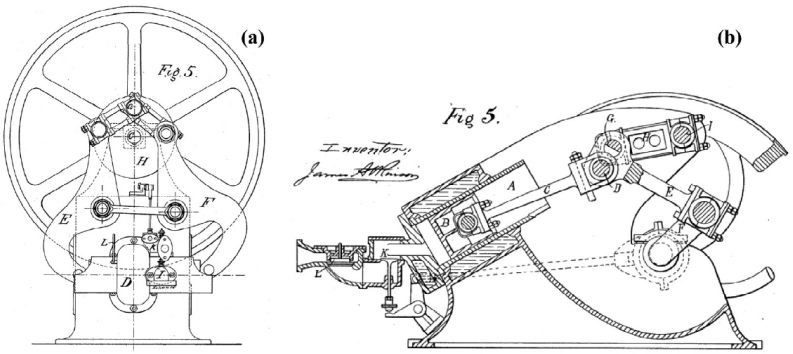

Figure 2.4: Patent drawing of the original Atkinson engine.

Since then, some other novel multi-link mechanical systems have been designed.
The mechanism shown in Figure 2.5 is a four bar mechanism that connects the piston to the crankshaft via an oscillating member positioned on the opposite side of the cylinder relative to the crankshaft. The oscillating member is supported on an eccentric shaft that rotates at half of the crankshaft speed in the same direction and is driven by the crankshaft. The oscillating member, eccentric shaft and crankshaft jointly impact the piston movement and give rise to a shorter intake and compression stroke than a long expansion and exhaust stroke. A phasing mechanism between the crankshaft and the eccentric shaft allows relative angular motion between them. This relative motion changes the piston position at TDC and thus changes the combustion chamber volume, allowing the compression ratio to be altered continuously.
This mechanism realizes the overexpansion cycle as in *Type 1* but also alters the CR by adjusting the combustion chamber volume as in *Type 3*.

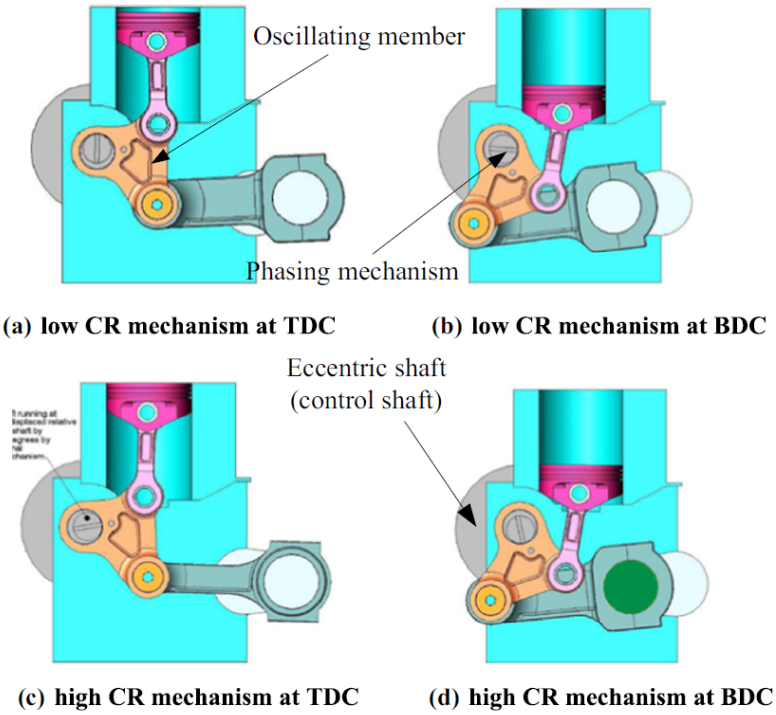

Figure 2.5: Mechanism for variable compression and stroke ratios.

The multi-link mechanical system shown in Figure 2.6 has been developed for Honda's EXlink (Extended Expansion linkage engine), as the world's first mass-produced multiple linkage ACE.
A multi-link system is primarily comprised of a trigonal link, a swing rod, an eccentric shaft, a connecting rod and a crankshaft. In the EXlink engine, the trigonal link is positioned between the connecting rod and the crankshaft. The trigonal link is connected to the eccentric shaft through the swing rod to accomplish the extended expansion linkage mechanism. The eccentric shaft, driven by the crankshaft, turns at half of the crankshaft speed in the same direction. This multi-link mechanism allows the piston's stroke to lengthen for the expansion/exhaust and shorten for the intake/compression per cycle. In this way, the *Type 1* Atkinson cycle can be realized in a simpler and more compact structure than the original one in Figure 2.4.
Shown in Figure 2.7, a crank train concept realized via a planetary gear mechanism has been researched as an effective measure to realize the Atkinson cycle (*Type 1*). Because of the defined gear ratios of the sun wheel (crankshaft), planetary wheel (extender) and annulus gear, piston motion for the Atkinson cycle could be generated.

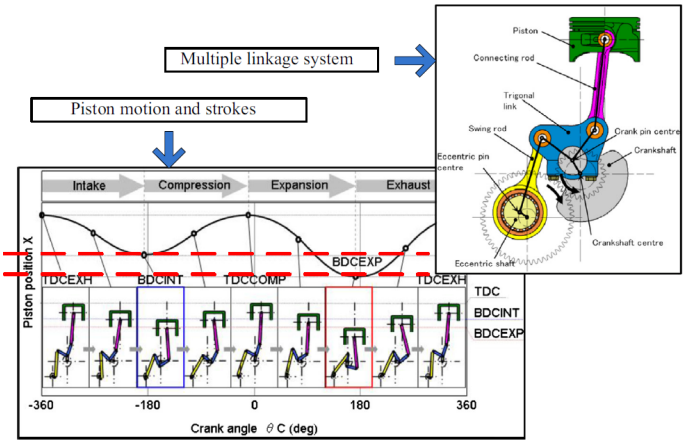

Figure 2.6: EXlink multiple linkage system and piston movement.

The Atkinson cycle piston motion is based on the superposition of the two movements of the extender and crankshaft. As a result, the dead volume remains invariable while an almost two times longer expansion stroke than the compression stroke is achieved. In this way, cylinder pressure at the end of the expansion stroke as low as the barometric pressure can be realized to fully extract the working potential of in-cylinder gases.

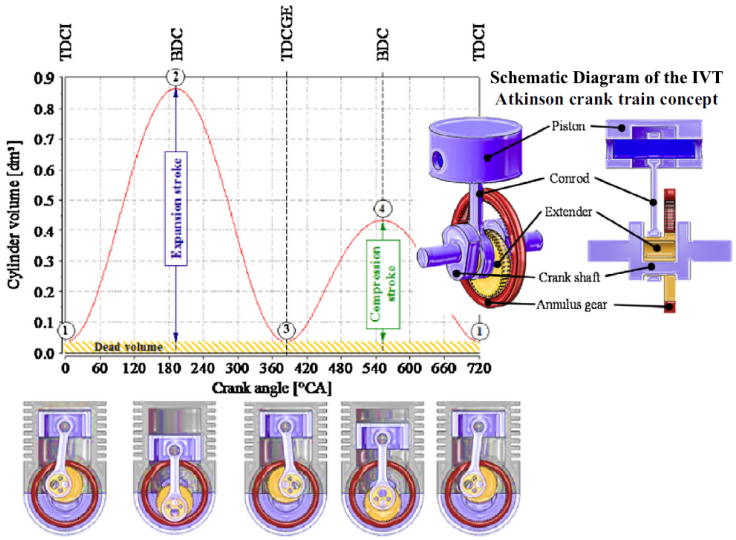

Figure 2.7: Piston motion and schematic diagram of the IVT Atkinson cycle concept.

Atkinson or Miller cycles for *Type 2* can be realized via LIVC (or EIVC) based on a baseline Otto (or Diesel) cycle engine. A series of discrete

LIVC timings can be performed by manually retarding the camshaft or fabricating some camshafts with different cam profiles, as shown in Figure 2.8(a).

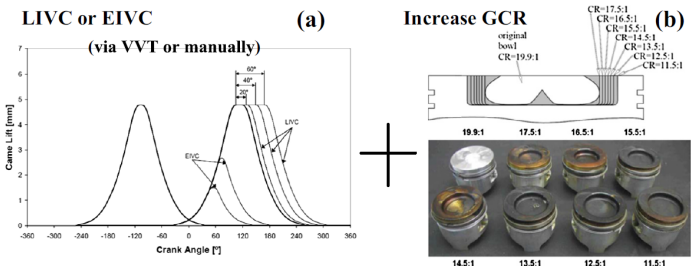

Figure 2.8: Atkinson or Miller cycle realized by LIVC (EIVC)+increased GCR.

Continuously variable LIVC timings can be implemented by a VVT mechanism. VVT technology has been widely used in gasoline engines, making it particularly easy to realize the over-expansion cycle. This type of ACE or MCE is actually a modified Otto (or Diesel) cycle engine. With a VVT mechanism, LIVC can be performed by keeping intake valves open longer than in the normal condition in the compression stroke shown in Figure 2.9. In this way, the expansion ratio, close or equal to the GCR, is larger than the ECR. The disadvantage is that a reverse flow process decreases the engine power density.

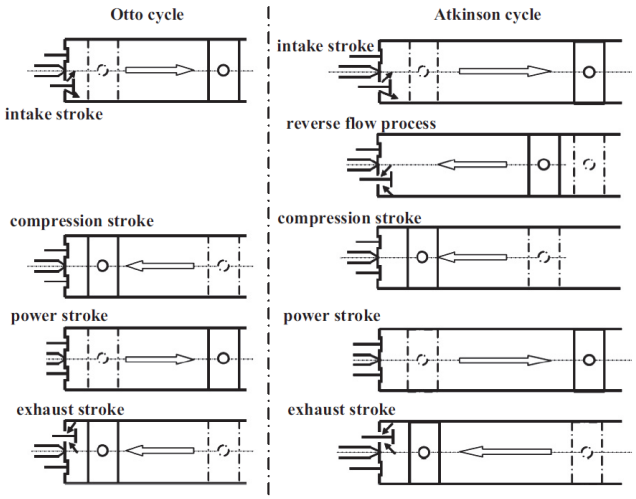

Figure 2.9: Comparison between the Otto cycle and over-expansion cycle realized via VVT.

For the EIVC shown in Figure 2.8(a), the intake valves close extremely early in the intake stroke. Then, pistons continue to run towards BDC, inducing an internal cooling process. After the BDC, the pistons run upward, compressing in-cylinder charges. The expansion and subsequent compression back to the volume at which the intake valves are closed is relatively energy-free, because both processes are nearly isentropic at such low temperatures. In this way, the effective expansion stroke is longer than the effective intake and compression strokes and enables equivalently realizing the over-expansion cycle.
EIVC will lead to considerable WOT power loss, especially in the high speed range. Higher intake boost pressure is needed to compensate the more power loss for EIVC. The efficiency is higher for EIVC because of the lower compression work compared to LIVC, when backflow to the intake manifold occurs.
With a partial load, *Type 2* can reduce pumping loss and improve fuel economy. However, the improvement is less as a result of the reduced ECR and the same expansion ratio as the baseline Otto cycle. The initial purpose of the Atkinson cycle SI engine is an increased expansion ratio to enhance thermal efficiency while maintaining a normal ECR to avoid the knock. The expansion ratio can be increased by lengthening the expansion stroke (*Type 1*) or reducing the dead volume that is *Type 3*.
For *Type 3*, mechanical realization by VVT+increased GCR is the most frequently adopted technical measure. The combustion chamber volume is reduced via changing the geometry of the piston top to increase the expansion ratio while a normal ECR is maintained based on LIVC.
The method using VVT+VCR can achieve optimum performance over the entire speed and load range. As shown in Figure 2.10, the combustion chamber volume can be continuously adjusted by changing the position of the outer piston relative to the inner piston, which is realized by controlling the oil pressure in the upper and lower oil chambers. In this way, ECR can remain invariable even though significant LIVC is performed and the expansion ratio can be the optimum value under any operating condition.

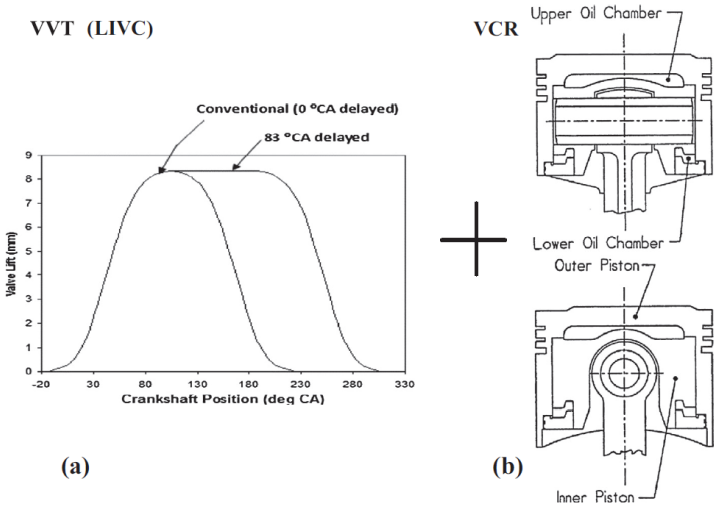

Figure 2.10: Atkinson cycle realized by VVT+VCR.

2.4 Applications and problems of the Atkinson cycle

2.4.1 Engine load control

During most of the operating time (almost more than 50%), conventional automotive engines work at partial load conditions.
It is particularly convenient and flexible to use a throttle valve to regulate fresh charge amounts. However, the throttle valve causes a large vacuum in the intake manifold, leading to considerable intake pumping loss. If the throttling losses can be cancelled out, 15–20% fuel consumption can be saved. The "Atkinson cycle effect" has been proved to be an effective method to assist in engine load control and improve partial load fuel economy by reducing pumping loss.
LIVC or EIVC can be implemented by a VVT mechanism to aid engine load control. As shown in Figure 2.11, the exhaust-intake pumping loop area ($= PMEP$) decreases because of LIVC or EIVC operation.
At the same engine load $IMEP_{net}$ ($= IMEP_{gross} - PMEP$), the compression-expansion loop area $IMEP_{gross}$ decreases, meaning that a lesser fuel-air mixture is required. In this way, the fuel economy is improved because of the $PMEP$ reduction.
At a constant engine load, a larger throttling width can be implemented because of the "Atkinson cycle effect". As a result, the vacuum degree in the intake manifold decreases, thus reducing the pumping loss.

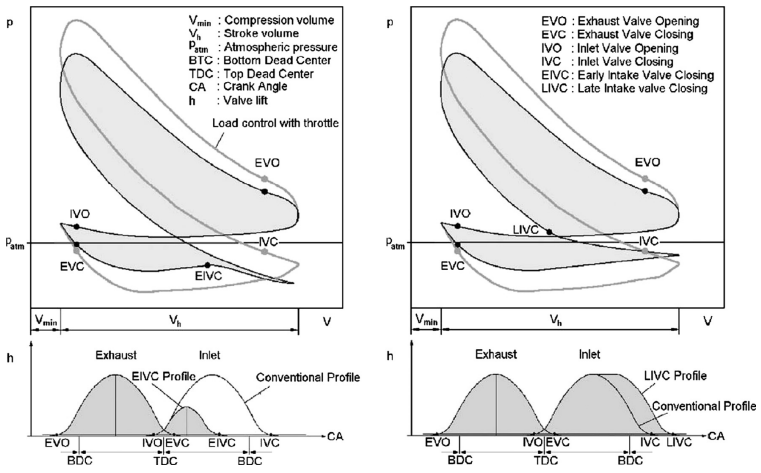

Figure 2.11: Comparisons of load control methods: EIVC or LIVC vs. Throttle.

2.4.2 NO_x formation reduction

The harmful emission NO_x mainly includes NO and NO_2; NO is the predominant oxide of nitrogen that is produced inside the engine cylinder. In SI engines, NO_2/NO ratios are negligibly small. For SI engines, the reduced ECR by LIVC or EIVC decreases the mixture pressure and temperature at the end of the compression stroke. Accordingly, the peak flame-temperature declines. Thus, the Atkinson or Miller cycle, as an effective way to reduce the peak flame-temperature, is an "internal cooling cycle". The NO_x formation is particularly temperature-dependent; this is the original idea for reducing the NO_x emissions based on the "Atkinson cycle effect".

2.4.3 Knock prevention

The knock is an abnormal combustion phenomenon that is the result of auto-ignition of the end-gas before the spark-flame front arrives. Its occurrence mainly depends on the end-gas temperature and pressure as well as the spark-flame development rate.
The "Atkinson cycle effect" is an effective measure for suppressing the knock because it can reduce the end-gas pressure and temperature. The principle for suppressing the knock is the same as that of reducing NO_x formation. Suppressing the knock is the original purpose of introducing the Atkinson cycle in a SI engine. A normal ECR could be maintained through LIVC or EIVC.

2.4.4 Main problems

In an SI engine, the most applicable load ranges for reducing pumping loss and NO_x formation, as well as suppressing the knock, are different. In the medium to low load range, the effect of pumping loss is more significant while it is more crucial for NO_x and the knock in the high load range. The primary problems are:

1. LIVC has two contrary effects on thermal efficiency. On one side, it can reduce pumping loss; on another side, it reduces the ECR and thus reduces the indicated thermal efficiency.

2. The effectiveness of the "Atkinson cycle effect" on reducing pumping loss in the high speed range declines because of the shortened time for a fresh charge to flow back to the intake manifold. Moreover, the effective LIVC range in reducing the charge amount is limited. Although EIVC has a larger load regulation range, its disadvantages are also significant, as described previously.

For the main problems of applying the "Atkinson cycle effect" in Atkinson or Miller cycle SI engines, a novel load control strategy over the entire load range is provided.

- Under extremely low loads, advance IVC timing for high ECR and only use the throttle valve to govern the engine load;

- Around a medium load, perform LIVC operation since pumping loss is considerable holding a substantial proportion of energy loss in this load range;

- At high loads, the NO_x and knock are crucial and the pumping loss is not of importance.

2.5 Possible solutions for reduced ECR

Three technical measures can be adopted to address the reduced ECR and extend the throttling-less load control range:

Mixture heating It is only suitable for medium to low loads. At high loads, mixture heating is not advantageous because it intensifies the knock tendency and increases the NO_x formation. Within the medium to low load range, improvement in fuel economy does not match the reduction of pumping loss.

Higher GCR It is thought that the thermal efficiency is mainly determined by the expansion ratio:

$$\eta_{th} = 1 - \frac{1}{ER^{k-1}}$$

For a modern ACE or MCE, a higher expansion ratio is generally realized by way of increasing GCR. Therefore, the negative effects of the ECR reduction can be compensated by the increased GCR.

VCR To maintain an invariable ECR, the clearance volume at TDC can be accordingly reduced as the load becomes light. A VCR mechanism can realize continuous compensation for the reduced ECR and can achieve the highest thermal efficiency improvement by optimizing the expansion ratio and extending the advantageous less throttling LIVC range.

Chapter 3

Validation of the 2.0 16V Alfa Romeo Engine

3.1 Introduction

This chapter opens with a brief description of the software that has been used to make all the simulations on which this work is based. Then, the architecture of the engine is described focusing on the most relevant components for the purposes of this thesis. In the last section the engine validation process is explained. It consists in comparing the parameters predicted with a simulation tool with the results obtained through an experimental campaign made in the Alfa Romeo testbeds before proceeding with the actual investigation.

3.2 Introduction to Gasdyn

The engine model analyzed in this thesis has been implemented in the one-dimensional Computational Fluid-Dynamic software Gasdyn, developed by the ICE team of Politecnico di Milano and based on the numerical methods previously presented.
The Graphical User Interface used to build up the engine model is called GasdynPre and consists in a workspace and toolbar containing the set of elements that can be included in a model (Figure 3.1). This software can perform a quick optimization of engine parameters like torque, power, fuel consumption, noise and pollutant emissions and model several layouts (multi-cylinder, multi-valve, naturally aspirated, turbocharged engines) and ignition systems (spark or compression ignition).
The simulations run by Gasdyn are of fundamental importance in com-

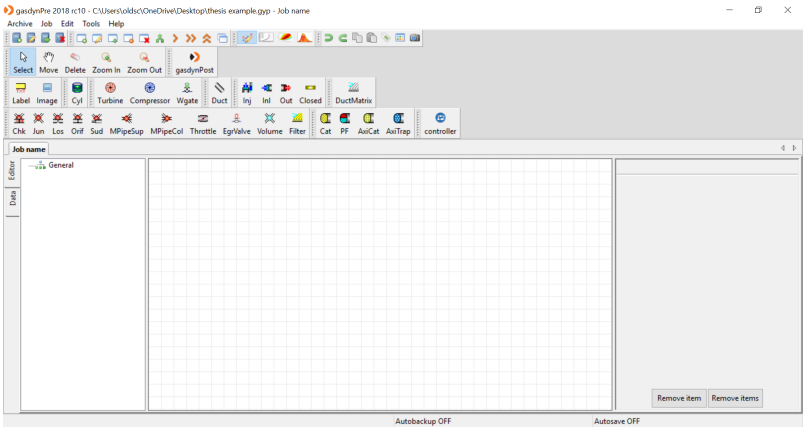

Figure 3.1: Gasdyn interface.

paring experimental and predicted data thus calibrating every engine component to improve the overall performance.
First of all, the engine scheme must be built up properly combining 1D (ducts) and 0D elements (junctions, volumes, etc. . .) and other objects that are a lumped-parameters representation of some components of the real engine (cylinders, valves, turbine, compressor).
This is a crucial step since it allows to turn the actual 3D engine geometry into a 1D scheme, thus reducing simulation time without compromising the reliability of the engine model.
Once the engine architecture is completed and every significant parameter has been specified, the simulation can start. The required time is proportional to the structural complexity and to the number of engine speeds simulated, each of which requires a variable number of calculation cycles so that the numerical results can converge.
Finally, some output files are created. These data can be post-processed making a comparison between experimental and predicted behaviour of the engine thus validating it.

3.3 The Engine

In this section the schematic of engine block, intake and exhaust lines is described. Then experimental data provided by the manufacturer will be compared with the ones predicted by Gasdyn.

3.3.1 Engine schematization

This thesis examines an Alfa Romeo, spark-ignition, four-stroke, 16 valves, 4 cylinders engine whose main characteristics are listed below:

Table 3.1: Main engine characteristics

Architecture	4 cylinders, in-line
Combustion Chamber	Pent roof, 132° angle
Bore	83 mm
Stroke	91 mm
Total Displacement	1968 cm^3
Compression Ratio	10
Rod Length	145 mm
Intake Valves	2
Exhaust Valves	2
Firing Order	3-2-4-1
Timing System	VVT, two modes
Maximum Brake Specific Power	56 $\frac{kW}{dm^3}$ @103 rps

The architecture of the engine is schematized in Gasdyn as shown in the following figure:

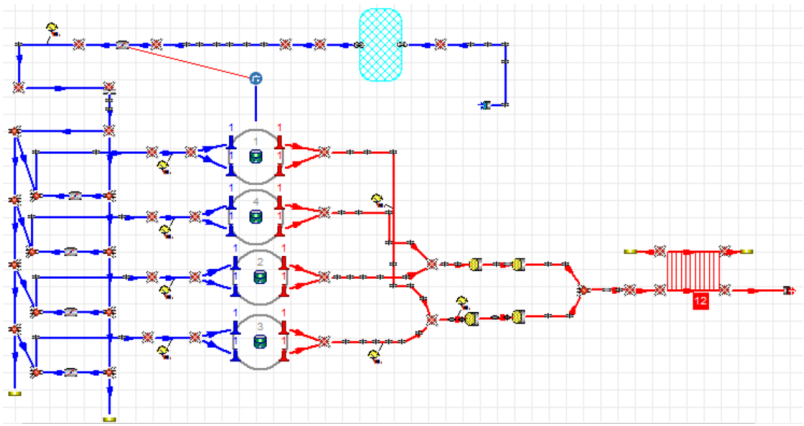

Figure 3.2: Gasdyn scheme.

Intake Line The intake line is opened by an isentropic inlet followed by two ducts connected by a simple Benson-type junction that offers the best modelling of pressure waves along the ducts. After that there is a plenum schematized as an expanded volume. The intake line continues with a series of ducts and more Benson junctions until the

throttle valve is found. Here the air flow is forced to contract due to the presence of the valve, hence it first compresses and then expands depending on the valve opening that can actuate a pressure recovery. At full load the engine operates in WOT (Wide Open Throttle) conditions:

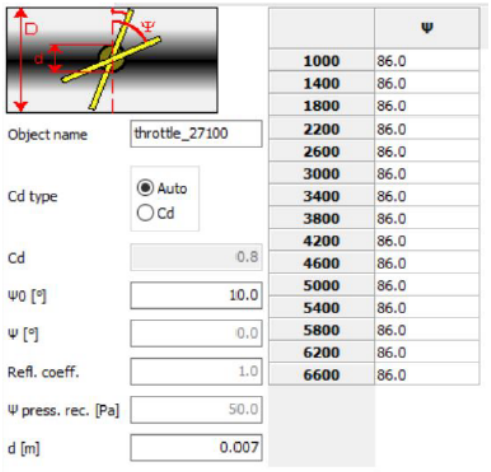

Figure 3.3: WOT characteristics.

Focusing on the throttle valve, the real opening angle that was found during a previous study of the same engine is 86° instead of 90° at full load.
A junction with a pressure loss coefficient of 4 is set at the entrance of the intake branches to calibrate pressure waves along the model. The ducts that connect the main intake route to the different cylinders are curved and each of them presents a throttle valve that can modify the air path (VIS, Variable Intake System) if needed.

Engine Head A total of four valves is located on the head of the cylinder: two for the intake and two for the exhaust line.
Intake and exhaust valves input data at full load, air fuel ratio A/F and spark advance for each regime are shown in the following figures:

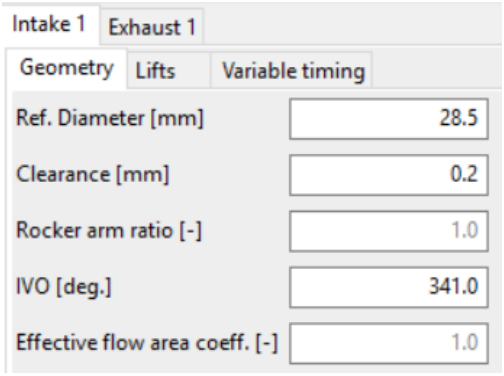

Figure 3.4: Intake valve geometry.

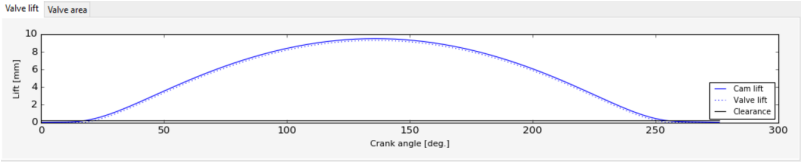

Figure 3.5: Intake valve lift.

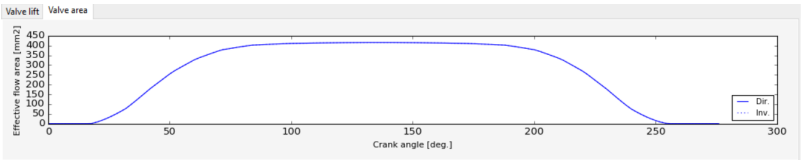

Figure 3.6: Intake valve area.

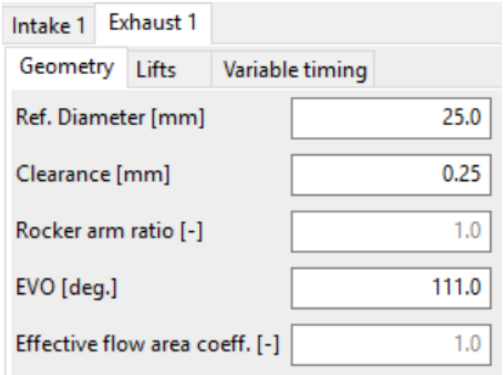

Figure 3.7: Exhaust valve geometry.

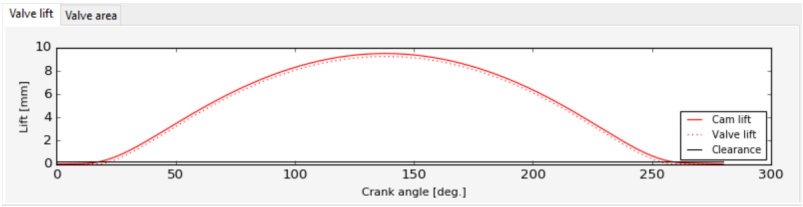

Figure 3.8: Exhaust valve lift.

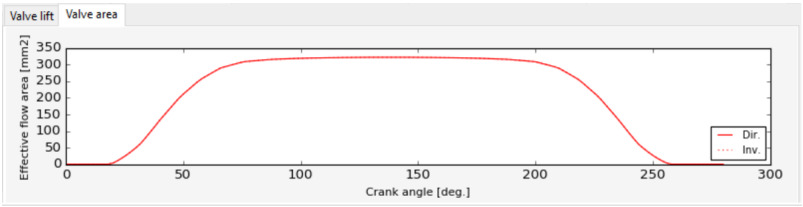

Figure 3.9: Exhaust valve area.

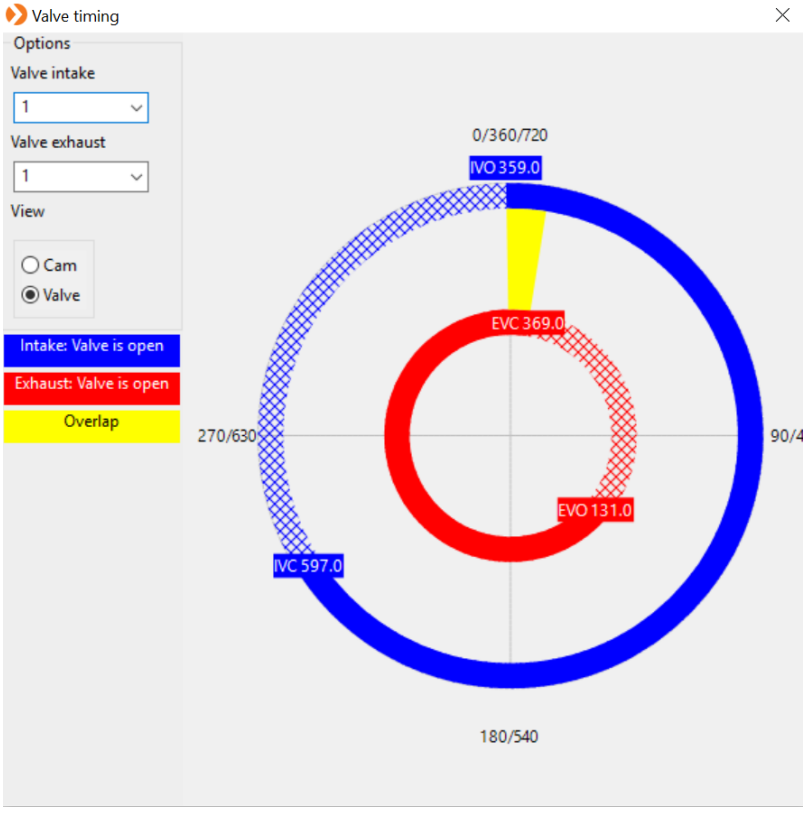

Figure 3.10: Valve timing circular diagram.

	A/F ratio [-]	Spark advance [deg. aTDC]
1000	12.2	-1.0
1400	12.9	-7.0
1800	12.9	-11.5
2200	12.8	-15.0
2600	12.8	-17.0
3000	12.7	-18.0
3400	12.8	-18.5
3800	12.7	-19.0
4200	12.7	-17.0
4600	12.5	-18.0
5000	12.5	-19.0
5400	12.5	-19.5
5800	12.5	-20.0
6200	12.4	-19.5
6600	12.3	-20.5

Figure 3.11: Full load A/F ratio and spark advance.

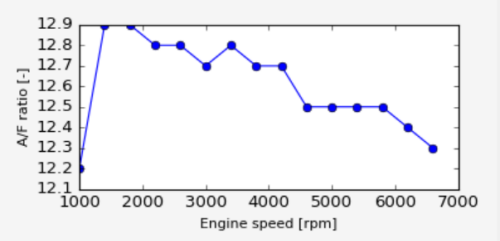

Figure 3.12: Full load A/F ratio.

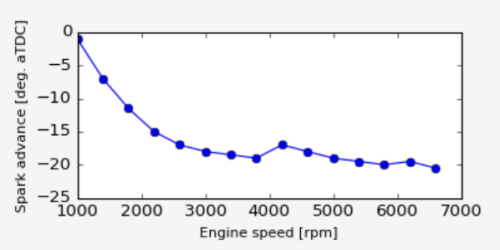

Figure 3.13: Full load spark advance.

The throttle valve and the cylinder head are connected through a PID controller that regulates the opening angle of the valve to achieve the desired torque for each part load of interest.
A proportional–integral–derivative controller (PID controller) is a control loop feedback mechanism widely used in those applications requiring continuously modulated control. A PID controller continuously calculates an error value as the difference between a desired setpoint (torque) and a measured process variable (opening of the throttle valve) and applies a correction based on proportional, integral, and derivative terms (denoted P, I, and D respectively), hence the name.
In practical terms it automatically applies accurate and responsive correction to a control function that can be expressed mathematically as:

$$u(t) = k_p e(t) + k_i \int_0^t e(\tau)\, d\tau + k_d \frac{de}{dt}$$

Where:

- u, control signal;
- $e = r - y$, control error;
- r, reference value also called setpoint;
- k_p, proportional gain;
- k_i, integral gain;
- k_d, derivative gain.

The control signal is thus the sum of three terms: a proportional term that is proportional to the error, an integral term that is proportional to the integral of the error, and a derivative term that is proportional to the derivative of the error.
In the following figure the controller parameters used are shown:

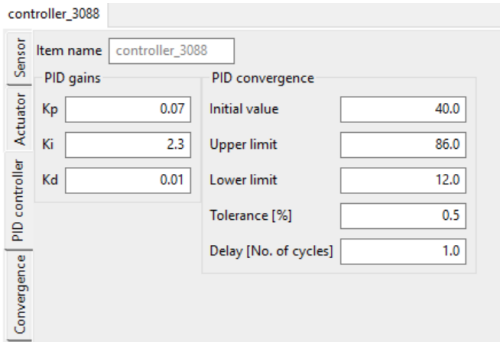

Figure 3.14: Controller parameters.

Anyways, the validation process focuses on the WOT condition; the PID controller operation will be exploited later when studying part load conditions.

Exhaust Line The exhaust ducts of each cylinder are joint together through a Benson-type junction forming a single duct, that in turn converges with the resulting duct of another cylinder. Such a coupling is made to reduce the interference between the discharge processes of each cylinder: pipe exiting cylinder 1 (0°CA) joins the one coming from cylinder 3 (360°CA) and the same for manifolds from cylinders 2 and 4.
At this point only two exhaust ducts are left, both connected to the pre-catalyst pipes with a Benson-type junction.

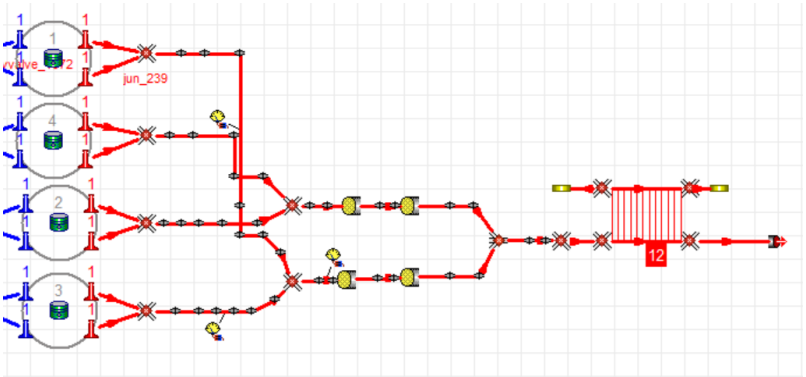

Figure 3.15: Exhaust line.

After that, two TWC_s (Three-Way-Catalytic Converters) are placed. It is possible to select many parameters related to them such as the geometry of the shell, the type of wash coat and insulating material,

specifics of the substrate and even the composition of the active layer. In this specific case, the ratio of Pt, Pd and Rh is 5:0:1; the first two act as oxidants for CO and HC, while the last one reduces NO.
Converters must be placed far enough from the cylinders to keep their temperature in the correct functioning range and before the silencer.
Finally, the two ducts left merge into a final pipe that ends with the silencer which is not simulated by its on model but with experimental back pressure data.

3.3.2 Model validation

Pressure waves

First, pressure waves in both intake and exhaust ducts are examined, then some general parameters like volumetric efficiency, brake power, brake torque, BMEP and total efficiency will be inspected.
Pressure waves are a good indicator of numerical methods accuracy. These have been measured in WOT conditions and for four different regimes: 1800, 3000, 5000 and 6600 rpm, that is the maximum brake power rotational speed.
Two measurement points have been chosen to measure the pressure waves of the intake line: downstream the throttle valve and right before the intake duct of cylinder 3 (the first one in the firing order) splits into two separate pipes connected to the intake valves.
The intake pressure waves downstream the throttle valve are reported below:

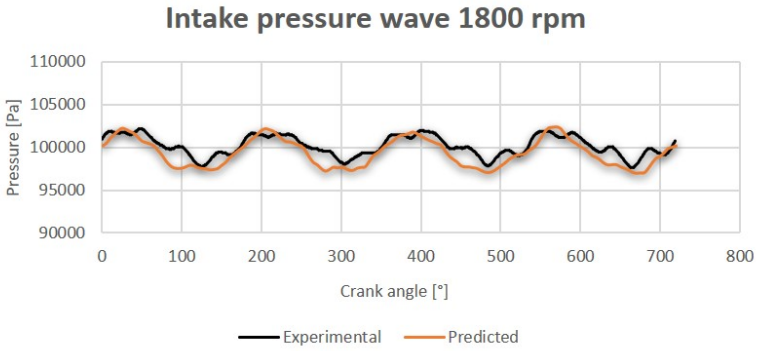

Figure 3.16: Intake pressure wave, full load, 1800 rpm.

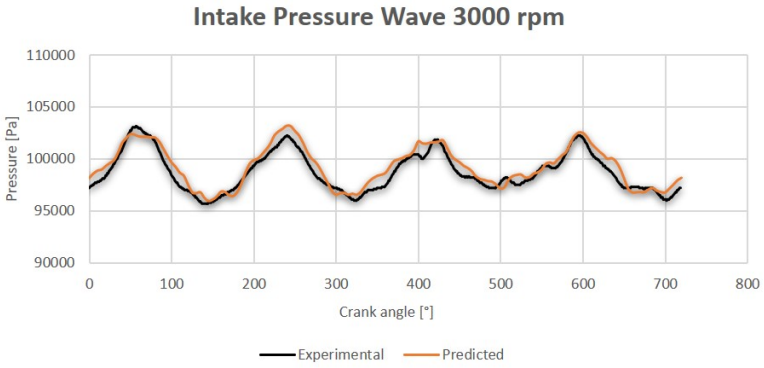

Figure 3.17: Intake pressure wave, full load, 3000 rpm.

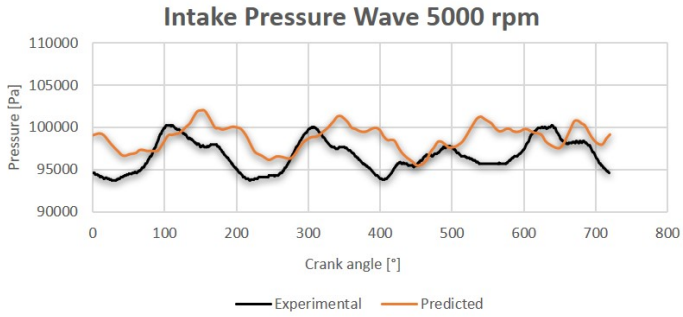

Figure 3.18: Intake pressure wave, full load, 5000 rpm.

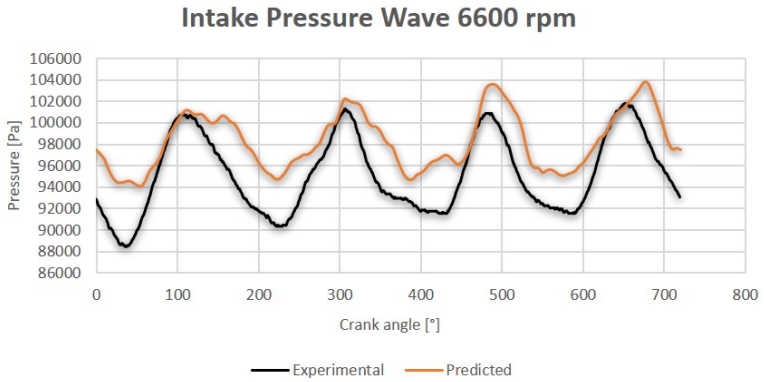

Figure 3.19: Intake pressure wave, full load, 6600 rpm.

From this plot it is evident that predicted results agree with experimental data especially at low engine speeds, while higher regimes are characterized by a good but slightly onward shifted trend.
Here a plot of static pressure as a function of rotational speed is provided:

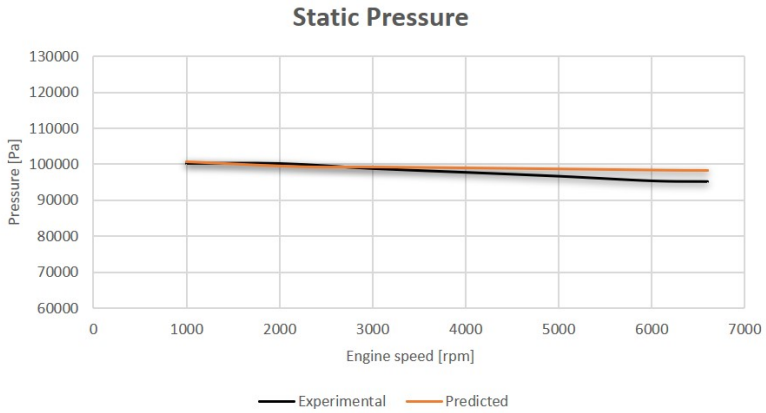

Figure 3.20: Static pressure downstream the throttle valve.

Pressure waves and static pressure in the second measurement point are displayed as well:

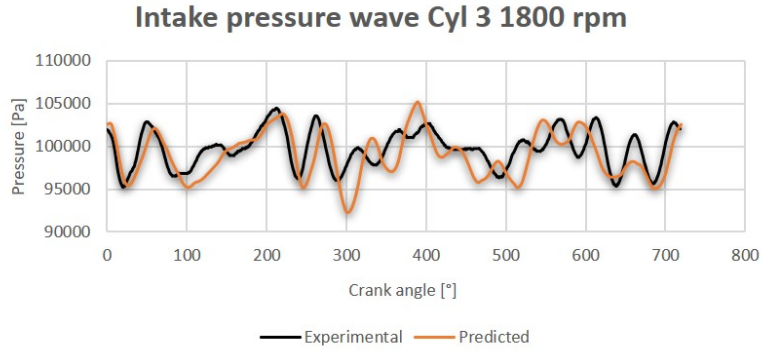

Figure 3.21: Intake pressure wave, full load, 1800 rpm.

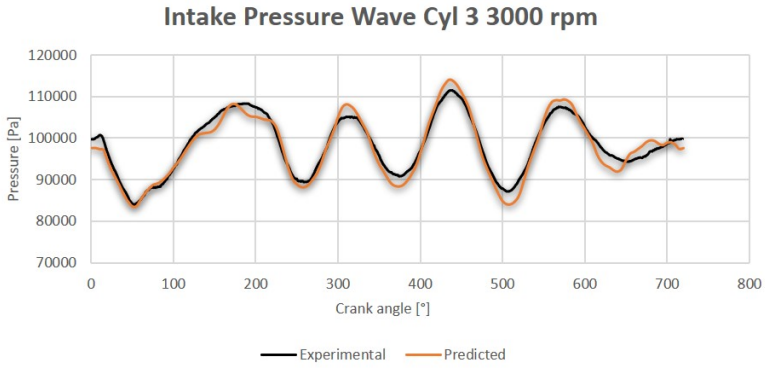

Figure 3.22: Intake pressure wave, full load, 3000 rpm.

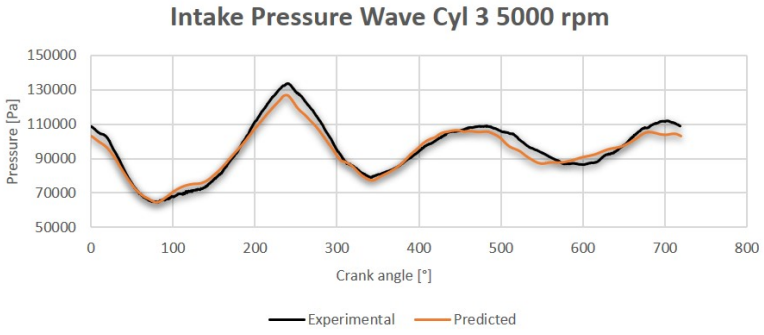

Figure 3.23: Intake pressure wave, full load, 5000 rpm.

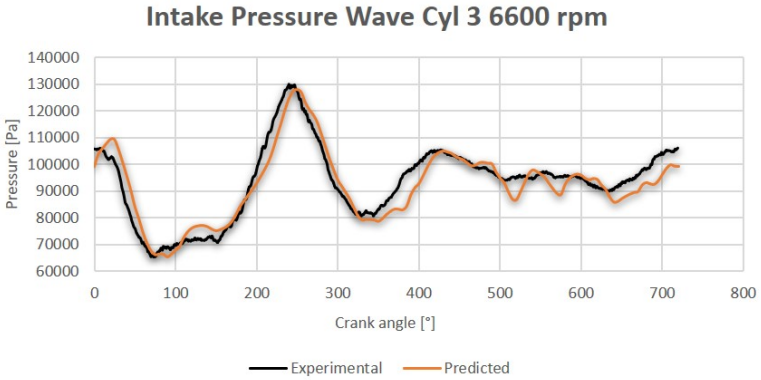

Figure 3.24: Intake pressure wave, full load, 6600 rpm.

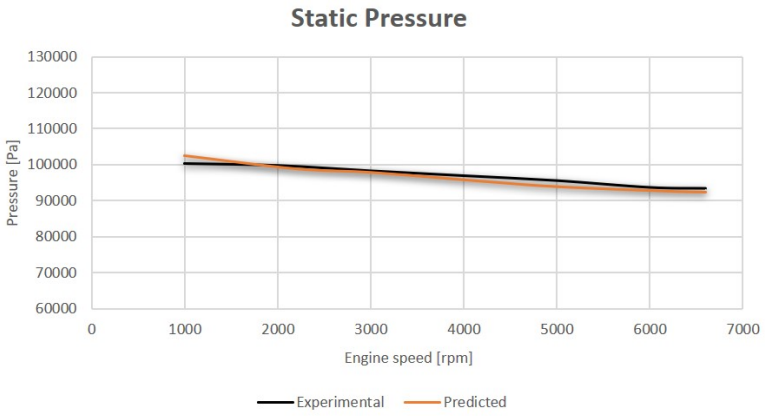

Figure 3.25: Static pressure in the intake duct of cylinder 3.

A good correspondence between simulated and experimental data is obtained in the second measurement point too, aside from the pressure wave at 1800 rpm that presents wider oscillations from 300°CA forward. Moving to the exhaust line, the following graphs depict pressure waves along the duct that connects the pipes exiting cylinder 3:

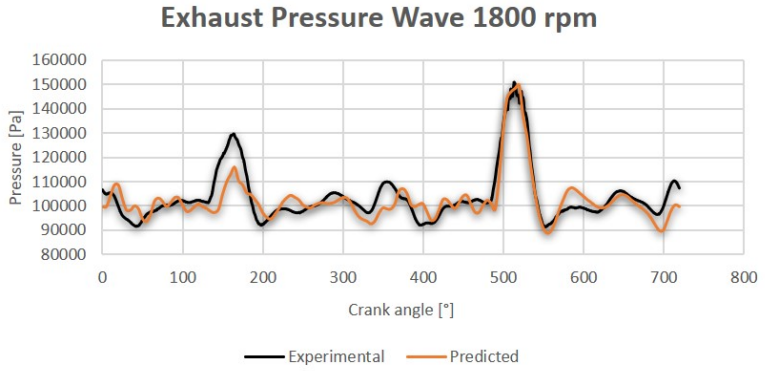

Figure 3.26: Exhaust pressure wave, full load, 1800 rpm.

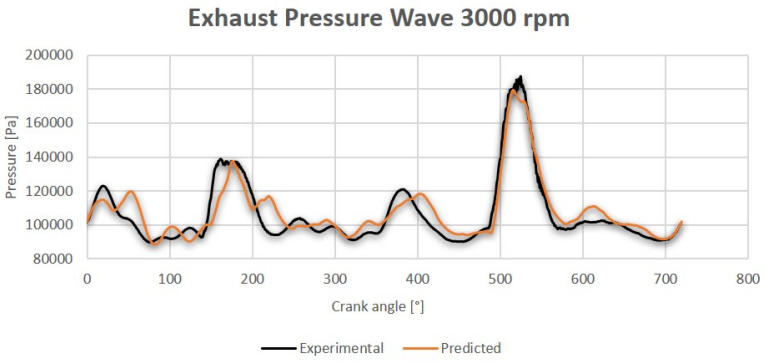

Figure 3.27: Exhaust pressure wave, full load, 3000 rpm.

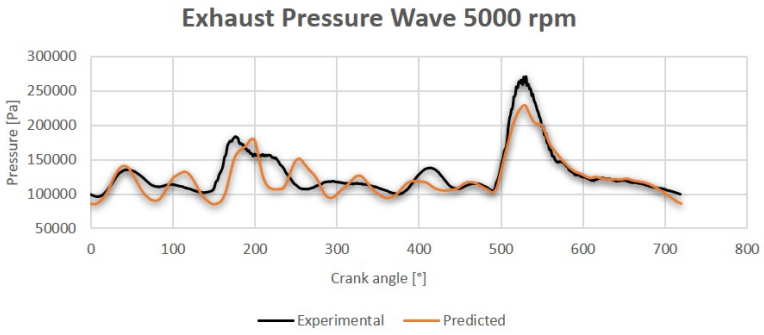

Figure 3.28: Exhaust pressure wave, full load, 5000 rpm.

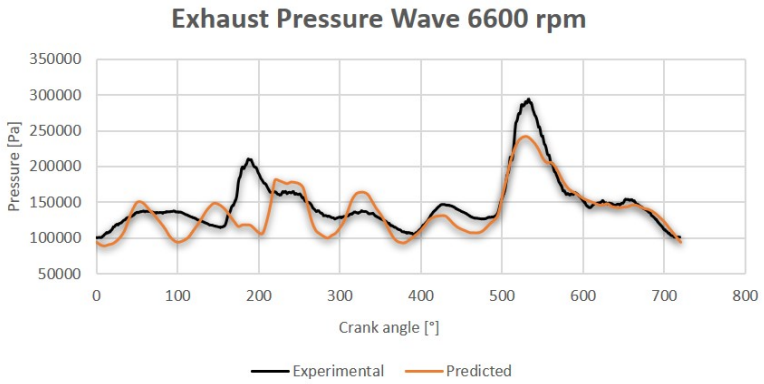

Figure 3.29: Exhaust pressure wave, full load, 6600 rpm.

As it is shown in the graphs, the exhaust pressure waves prediction worsens as the rotational speed increases. Again, at 5000 and 6600 rpm the trends do not overlap until 500°CA is reached.

A good correspondence between experimental and predicted data has been found for cylinder pressure too:

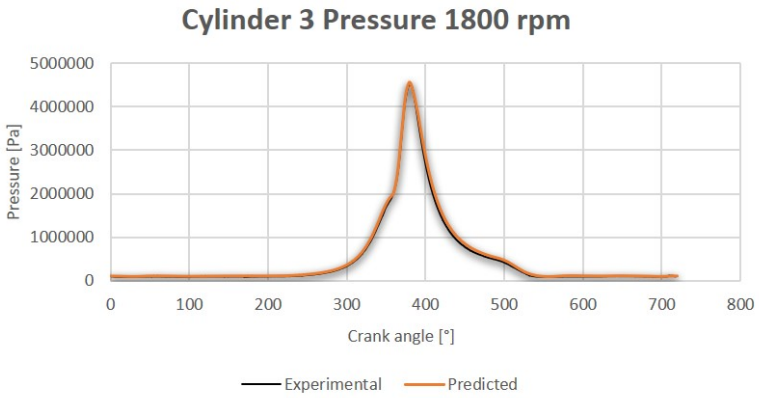

Figure 3.30: Cylinder pressure wave, full load, 1800 rpm.

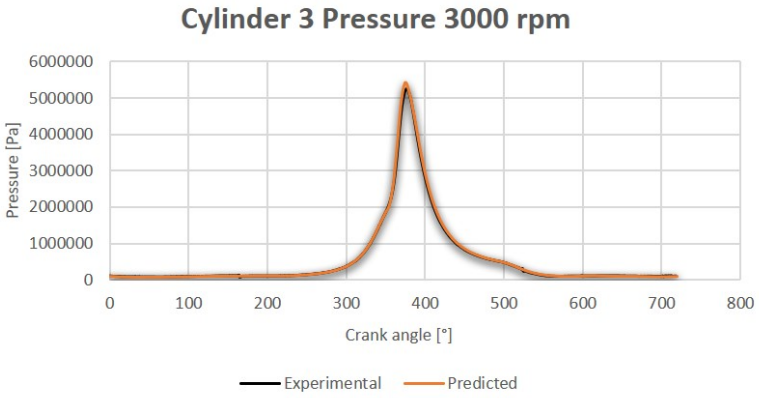

Figure 3.31: Cylinder pressure wave, full load, 3000 rpm.

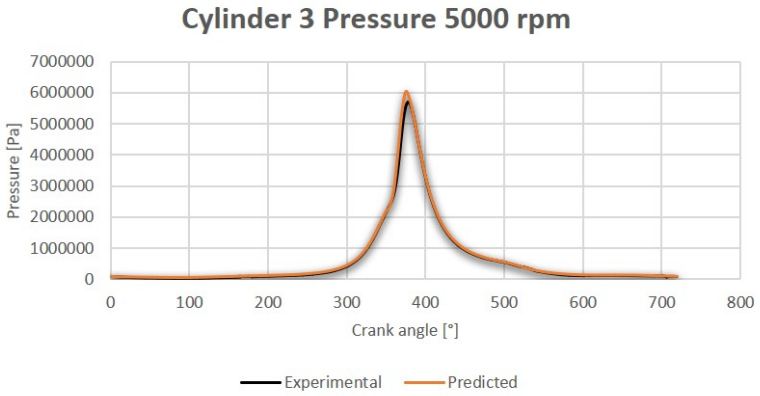

Figure 3.32: Cylinder pressure wave, full load, 5000 rpm.

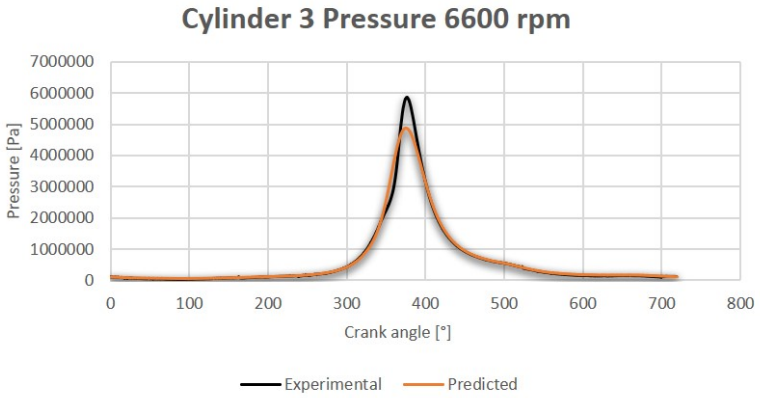

Figure 3.33: Cylinder pressure wave, full load, 6600 rpm.

Main engine parameters

The volumetric efficiency λ_v is a measure of the effectiveness of the global intake process. The following plot shows the overall trend of λ_v computed as the average of the volumetric efficiency of each cylinder for the entire range of rotational speeds considered by now. It shows a slight overestimation of the prediction at high rpm only.
Air mass flow rate is strictly related to volumetric efficiency, its comparison to experimental data was successful and it is reported as well:

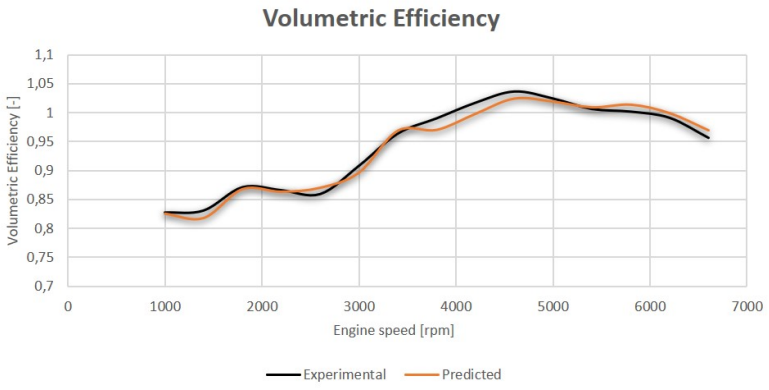

Figure 3.34: Average cylinder volumetric efficiency.

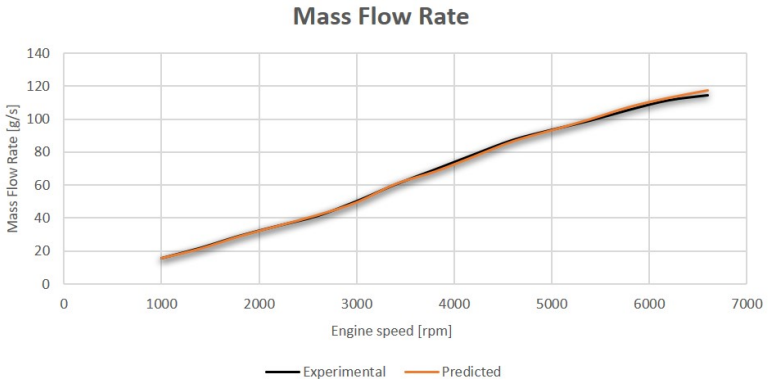

Figure 3.35: Mean mass flow rate aspirated by the engine.

The filling process influences many other parameters, especially torque; indeed, it shows a similar trend and a good correspondence with testbeds' data:

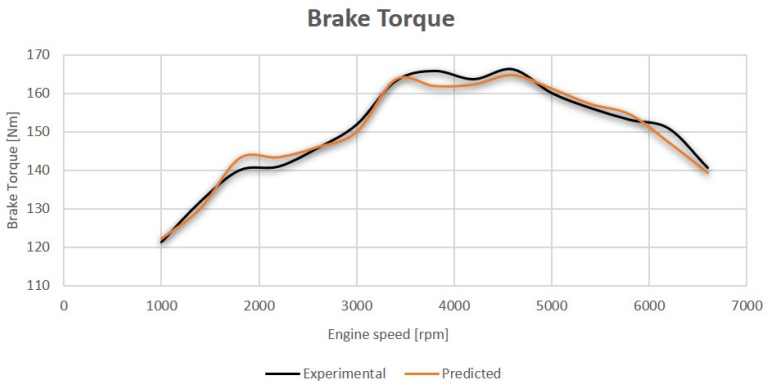

Figure 3.36: Torque curve.

Power curves are obtained multiplying torque curves and rotational speed and increase throughout the whole engine operating range.

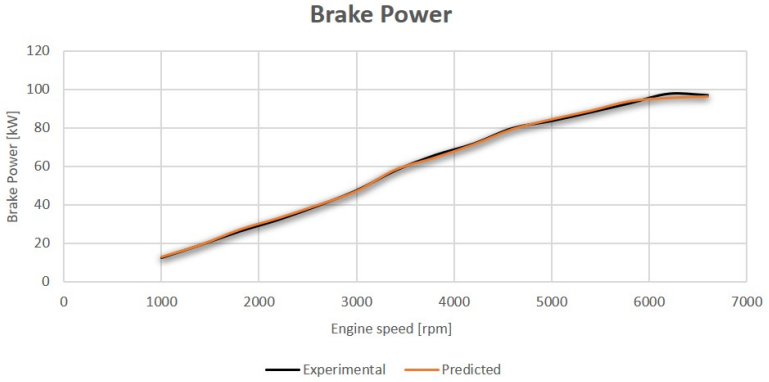

Figure 3.37: Power curve.

The final working parameter shown in this section is BSFC (Brake Specific Fuel Consumption). It is included in this study because it is strictly related to the global efficiency of the engine as it is an index of the capability of the engine to exploit the energy contained into a unit mass of fuel to produce mechanical energy.

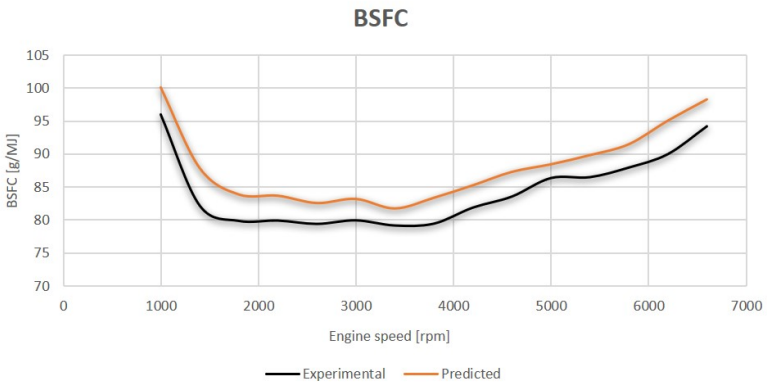

Figure 3.38: Brake specific fuel consumption.

The plot shows a typical decreasing-increasing BSFC trend for both experimental and predicted data, but the last one is globally greater than the first one due to software overestimation.

Pollutant emissions

Finally, pollutant emissions of a single cylinder are examined:

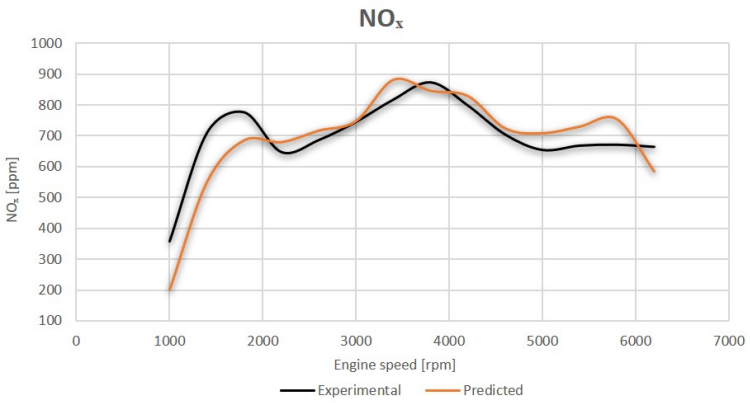

Figure 3.39: NO_x cylinder emissions.

NO_x prediction shows some discrepancies with respect to the experimental trend but it is acceptable anyway.
Moving to CO, Gasdyn outputs turn out to be quite accurate:

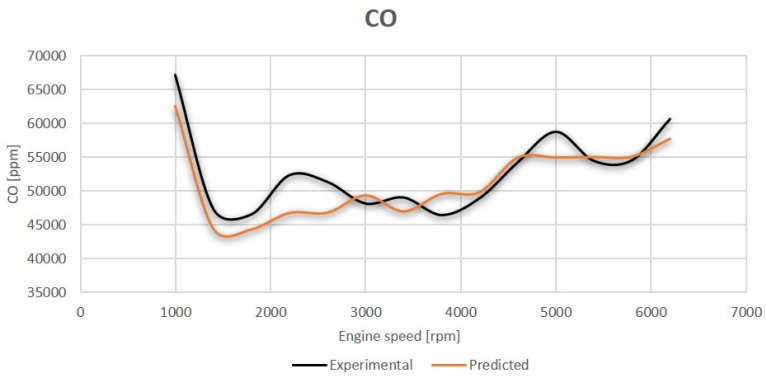

Figure 3.40: *CO* cylinder emissions.

The last pollutant of interest is CO_2, whose predicted trend shows an overall congruence with the experimental one, aside from the low rpm range that exhibits a slight overestimation of the results.

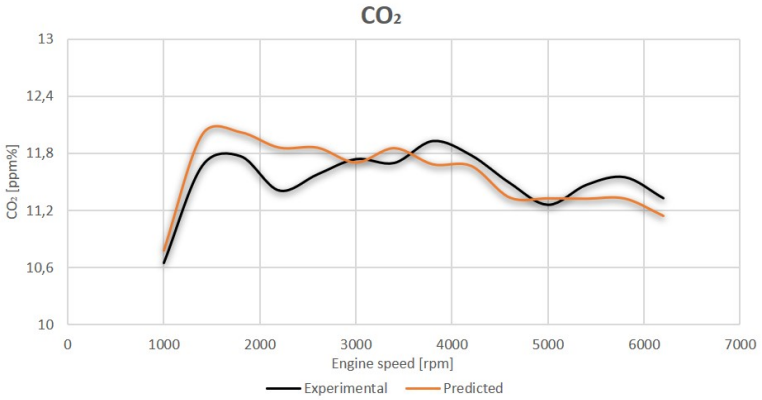

Figure 3.41: CO_2 cylinder emissions.

Chapter 4

Investigation on LIVC/EIVC and Increased GCR Effects During Part Load Operations

4.1 Introduction

This chapter discusses the two intake valve closing strategies that can be used to realize Atkinson-Miller cycles, thus reducing pumping losses during part load. They are called Early Intake Valve Closing (EIVC) and Late Intake Valve Closing (LIVC). Both strategies keep the intake valve opening point in a fixed position, whilst moving the closing point to reduce pumping losses and hence improve fuel economy.
Since most of the time gasoline engines are not full load operated in vehicle applications, especially in city traffic, part load operation covers the most common operation situations. However, engine part load performances deteriorate due to pumping losses and low thermal efficiency, but Atkinson-Miller cycles seem to attenuate such drawbacks by increasing the opening angle of the throttle valve to obtain the same brake torque of the basic Otto cycle.
Hence this works is focused on part load rather than full load that is examined in the validation phase only.
To actuate these strategies, it is necessary to find new valve lift profiles that adapt to the new valve timings, hence a calculation of them has been done and plotted by the graphs in Figure 4.1 and 4.4.
After choosing the investigation operating points (regimes and loads), the next step was to find the correct opening angle of the throttle valve to match the desired brake torque for each of them with the help of the PID

controller described in Chapter 3.
Then, simulations for each load and IVC were made and both convenient and inconvenient cases arose and will be explained away later.
Finally, one last modification on the engine was made: the compression ratio CR was increased from 10 to 13 by modifying some cylinder parameters and keeping EIVC and LIVC valve lift profiles to combine the effects of the two modifications.
The results of both actions will be examined within the whole chapter.

4.2 New valve lift profiles

4.2.1 Late intake valve closing

Starting from the original valve lift profile of the Alfa Romeo engine exported from Gasdyn, a generic LIVC of x°CA is obtained by extending the duration of the maximum lift of the base camshaft. After several simulations it is emerged that the feasible LIVC intervals for the purposes of this thesis are the following:

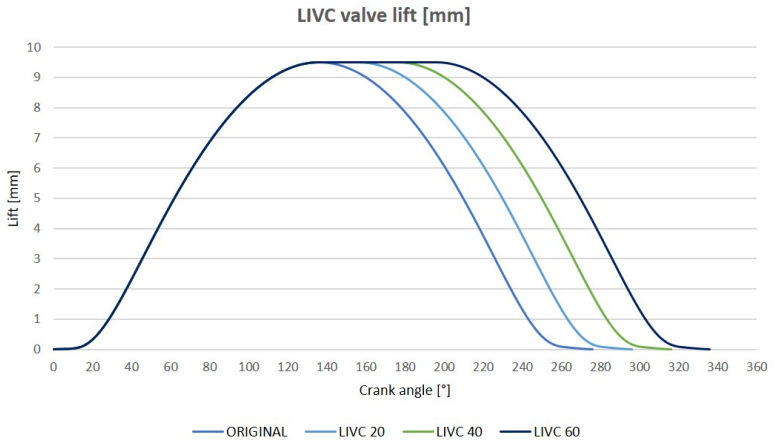

Figure 4.1: LIVC valve lift profiles.

Moving to Gasdyn, the new valve lift profiles have been imported from the Excel files just created, producing the valve timing graphs reported below:

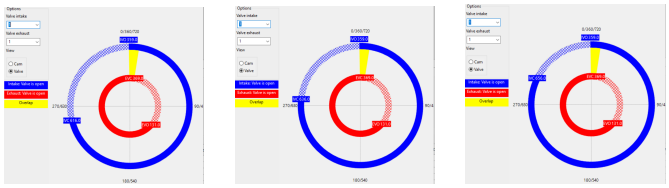

(a) (b) (c)

Figure 4.2: Valve timings: LIVC20 (a), LIVC40 (b), LIVC60 (c).

Now, the intake valve closes at 616, 636, and 656°CA instead of 596°CA as in the base case, named "ORIGINAL".

4.2.2 Early intake valve closing

On the other hand, a generic EIVC of x°CA is realized with a reduced lift compared to the original profile. Such reduction requires a more complex procedure.
Each curve must have the same shape of the original one; to do so, some assumptions and conditions are applied.
The lift profile is assumed to be exactly the same at the beginning/end of the opening/closing event, so within the first and the last 75°CA for EIVC60 and EIVC80, and 30°CA for EIVC100 and EIVC120 the values of the valve lift are the same.
Then, the central part of the curve is derived through a polynomial approximation, according to the following conditions:

- The initial point, x_{start} (76 or 31°CA), of the polynomial and its derivative are the same as those of the original profile;
- The final point, x_{end}, of the polynomial and its derivative are the same as those of the original profile. The positioning of this point depends on the selected advance:

$$x_{end} = IVC_{original} - x_{same} - ADV$$

Where:

  - $IVC_{original} = 276°CA$ is the crank angle at which the original Otto cycle closes the inlet valve;
  - $x_{same} = 75\ or\ 30°CA$;

– $ADV = 60,\ 80,\ 100\ or\ 120°CA$ is the advance that can be adopted.

An illustrative figure is reported below:

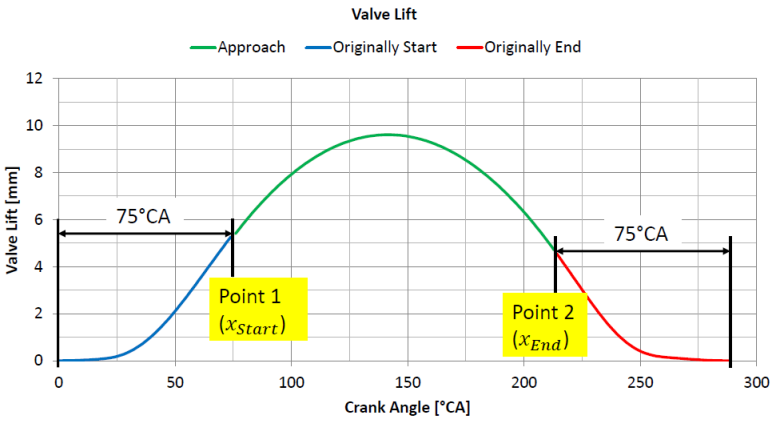

Figure 4.3: Different sections of the valve lift curve.

Thanks to these assumptions, a good connection between the first, central and last portion of the curve is achieved. The derivatives are generated by using the difference quotient of the original profile around the starting and ending points of the polynomial approximation:

$$f'(x_{start}) = \frac{f(x_{start+1}) - f(x_{start-1})}{x_{start+1} - x_{start-1}}$$
$$f'(x_{end}) = \frac{f(x_{end+1}) - f(x_{end-1})}{x_{end+1} - x_{end-1}}$$

Since there are four necessary conditions, the solution is determined by a polynomial of third degree:

$$f(x) = ax^3 + bx^2 + cx + d \tag{4.1}$$

Whose derivative is:

$$f'(x) = 3ax^2 + 2bx + c$$

Applying the aforementioned conditions to $f(x)$, a set of four linear equations with the four unknowns a, b, c and d can be solved numerically by

means of the Gaussian Elimination Method.
Finally, the value of the valve lift for each point within the interval $(x_{end} - x_{start})°CA$ is computed by the equation 4.1 and the complete profile in Figure 4.4 is created:

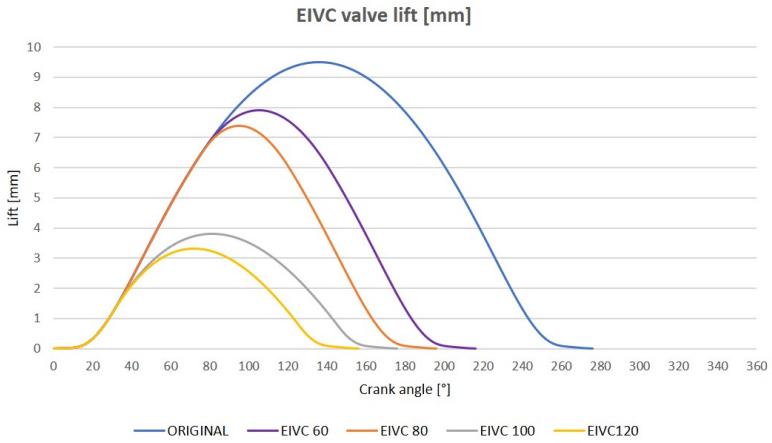

Figure 4.4: EIVC valve lift profiles.

Moving to Gasdyn, the new valve lift profiles have been imported from the Excel files just created, producing the valve timing graphs reported below:

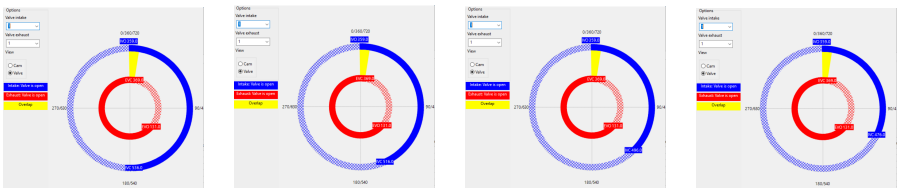

(a) **(b)** **(c)** **(d)**

Figure 4.5: Valve timings: EIVC60 (a), EIVC80 (b), EIVC100 (c), EIVC120 (d).

Now, the intake valve closes at 536, 516, 496 and 476°CA instead of 596°CA as in the base case.

4.3 Part load settings

4.3.1 Operating points selection

The main purpose of this work is to prove that the Atkinson-Miller cycle can improve fuel economy and total efficiency at part load which is generally characterized by the lowest efficiencies due to strong pumping losses connected to the throttle valve load regulation.
Therefore, some loads and regimes are chosen for this investigation.
Two low (15 and 30%), an intermediate (50%) and a high (70%) load are selected to cover almost the entire operating field of the engine. These percentages are referred to the brake torque at full load, hence, the desired values $T_{desired}$ are computed as:

$$T_{desired}\ [Nm] = T_{full\ load}\frac{Load\%}{100}$$

The analysis is carried out by varying the rotational speed for each load; in particular, 1800, 3000 and 4200 rpm are considered to be representative of the most common operating conditions for a car equipped with a SI engine.
The combination of 4 load percentages and 3 regimes gives a total of 12 operating points.

4.3.2 Throttle valve adjustments

Once the desired values of the torque for each point are evaluated, the corresponding throttle valve opening must be detected with the help of the PID controller presented in Chapter 3.
To simulate these 12 points in Gasdyn with a single job, a sort of trick is necessary. In fact, taking as example the 1800 rpm regime family, it is not possible to select 1800 rpm for each load, hence the operating point characterized by 1800 rpm and part load 70% corresponds to 1800 rpm in Gasdyn, the one defined by 1800 rpm and part load 50% is marked out as 1801 rpm and so on. Then, all the target values are inserted in the PID controller *Sensor* section.

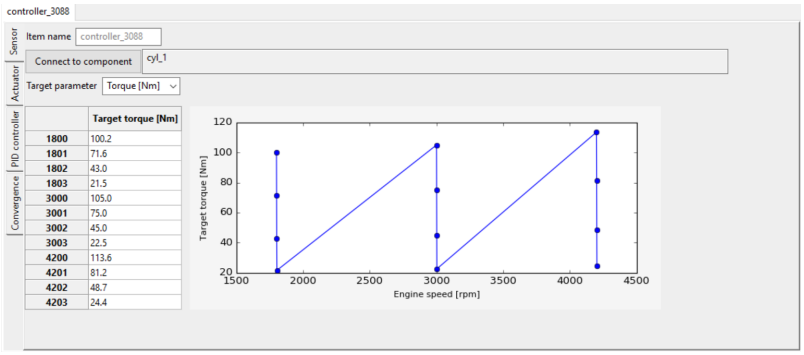

Figure 4.6: *Sensor* section on Gasdyn: Target torque.

A sensor is placed into the cylinder to measure the instantaneous values of the torque (target parameter) and to communicate them to the controller with a closed-loop mechanism until they reach convergence (Figure 4.7), otherwise the PID controller keeps adjusting the throttle valve opening (actuated parameter) and another simulation cycle begins.

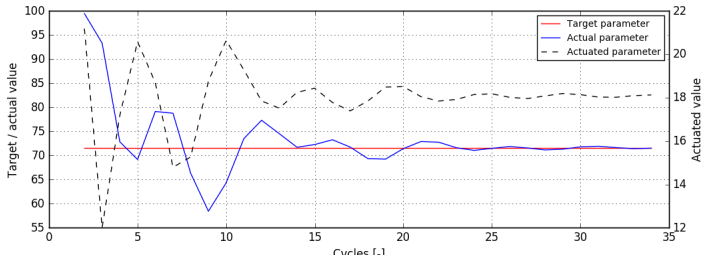

Figure 4.7: Example of convergence output plot.

The maximum number of simulation cycles is set at 100 and the tolerance at 0.5%, but if the actual parameter (blue line) approaches to the target parameter (horizontal red line) before the 100^{th} cycle, the controller skips to the next regime. Anyways, the convergence is not always reached, hence some errors have to be taken into account.

4.4 LIVC and EIVC application

After setting the controller up, a job that collects every load and regime is created in Gasdyn for each delay and advance and simulations can be launched.
The main purpose of these simulations is to prove that the application of LIVC and EIVC strategies can lead to enhanced fuel economy and higher

total efficiency. To make different cases comparable with each other, the torque is kept constant for each delay and advance applied to the same operating point (same regime and load).
The ideal LIVC strategy allows air to be drawn into the cylinder close to atmospheric pressure for the entire induction stroke, thus drawing in the maximum possible air mass. The intake valve is kept open during the beginning of the compression stroke, allowing some of the trapped air to flow back out of the cylinder into the intake manifold.
While if EIVC is adopted, the intake valve closes part of the way through the induction stroke to prevent any further air from entering the cylinder. Both interventions result in a reduced amount of trapped air.
The expectation of this action is to reduce pumping losses, the greatest source of efficiency decay, by increasing the opening angle of the throttle valve to reach the desired torque despite the lower air mass flow rate aspirated by each cylinder.

4.4.1 Results and discussion

In this section only the most favourable simulations' outputs are selected and reported.
In some cases, strong delays or advances did not make it possible to reach the targeted torque due to an excessive reduction of the effective compression ratio, therefore they are not discussed.

Part load 15%

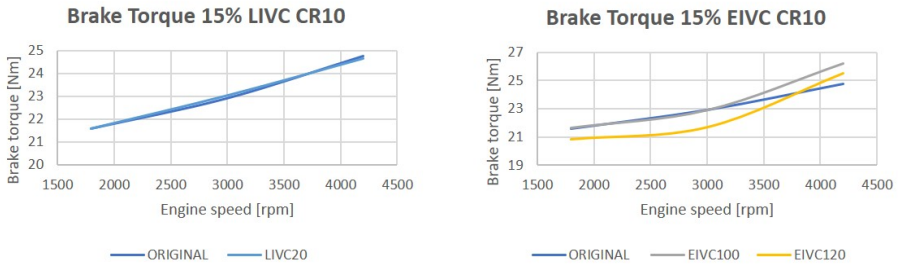

(a) **(b)**

Figure 4.8: Brake torque 15%: LIVC (a), EIVC (b).

As shown by the plot, LIVC20 brake torque perfectly adheres to the ORIGINAL desired one, while if delays to the intake valve closure are

applied, the controller output is less precise but still acceptable, nonetheless it affects other parameters.
The brake specific fuel consumption BSFC [g/MJ] is defined as the amount of fuel required to produce a single unit of energy and indicates the capability of the engine to convert fuel's chemical energy into mechanical energy.
The third fundamental parameter of this analysis is engine total efficiency, intended as the ratio of the work produced per cycle to the amount of fuel energy supplied per cycle that can be released in the combustion process. BSFC strongly influences total efficiency, according to the formula:

$$\eta_{tot} = \frac{P_{brake}}{m_{fuel} Q_{LHV}} = \frac{1}{BSFC\ Q_{LHV}}$$

In fact, they have a specular trend:

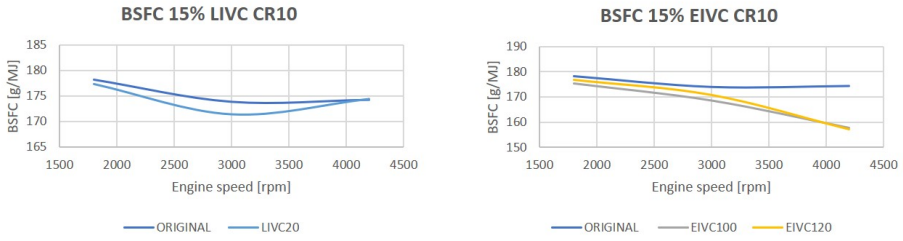

(a) **(b)**

Figure 4.9: BSFC 15%: LIVC (a), EIVC (b).

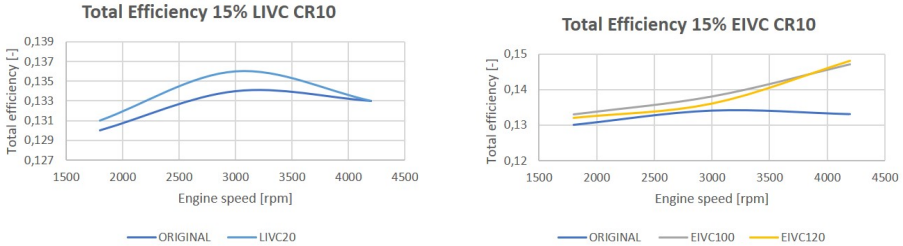

(a) **(b)**

Figure 4.10: Total efficiency 15%: LIVC (a), EIVC (b).

In the LIVC20 situation, BSFC is almost equal to that of the ORIGINAL case at the beginning and at the end of the considered engine speed range;

a reduction from 173.9 g/MJ to 171.3 g/MJ is obtained at 3000 rpm and is reflected by an improvement in total efficiency of 0.2% (from 13.4% to 13.6%).
A bigger improvement in fuel economy is recorded for EIVC120 as the rotational speed increases; in fact, at 4200 rpm BSFC decreases from 174.3 g/MJ to 157.2 g/MJ, leading to an increase of total efficiency from 13.3% to 14.8%.
An alternative visualization of these improvements is the bottom area of the cycle p-V diagram that represents the compression work made by the piston: if this area shrinks, the negative work decreases and the efficiency grows.

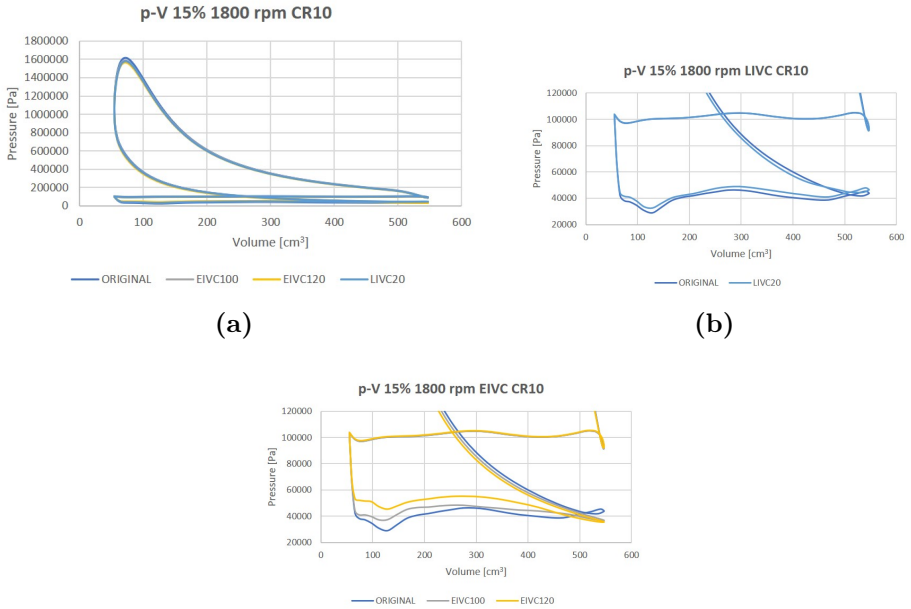

Figure 4.11: p-V diagram 1800 rpm 15% (a); LIVC (b), EIVC (c) close-ups.

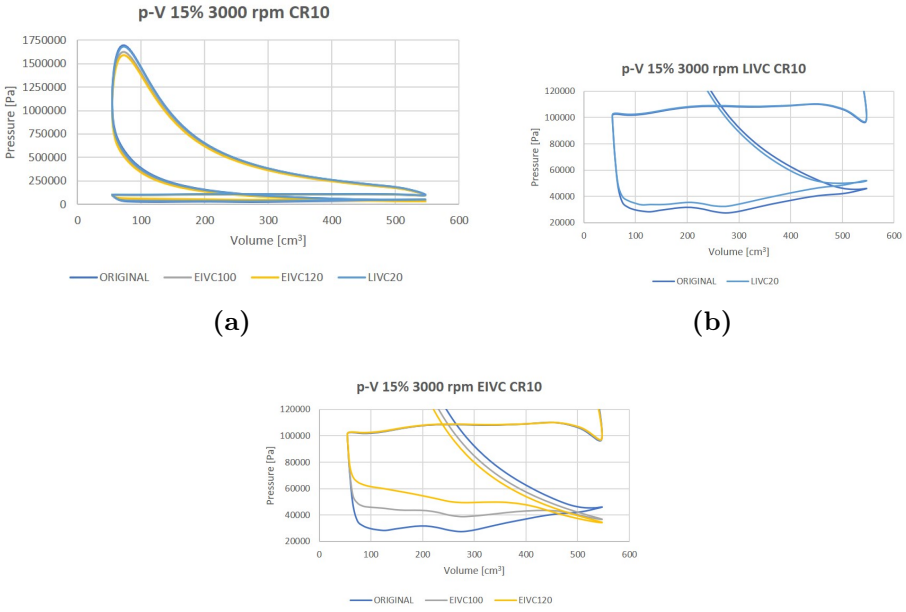

Figure 4.12: p-V diagram 3000 rpm 15% (a); LIVC (b), EIVC (c) close-ups.

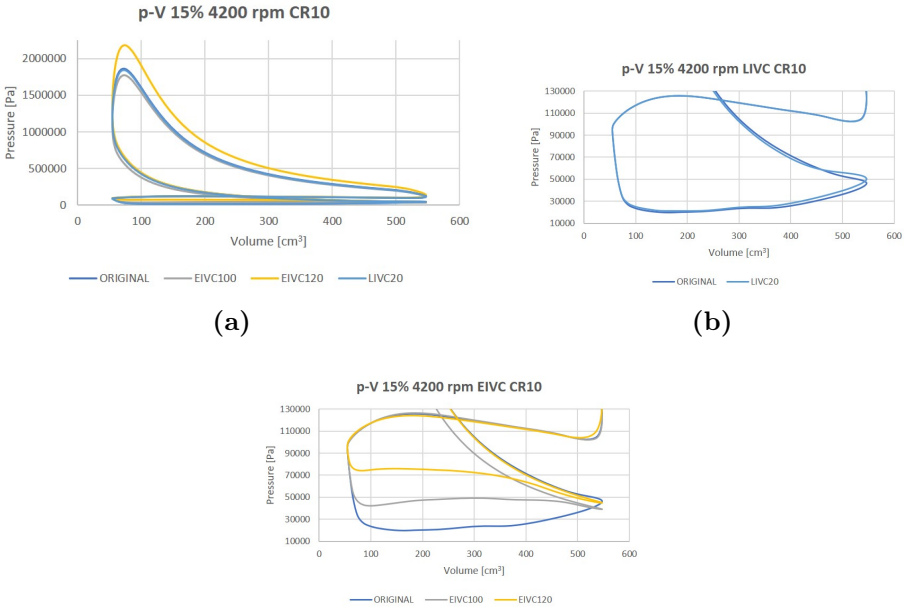

Figure 4.13: p-V diagram 4200 rpm 15% (a); LIVC (b), EIVC (c) close-ups.

As for BSFC and total efficiency plots, the biggest improvement is observed at 4200 rpm for EIVC120, while for LIVC20 the reduction of the bottom area is as slight as the fuel economy/total efficiency gain at 3000 rpm.
Some additional considerations can be made for pollutants.

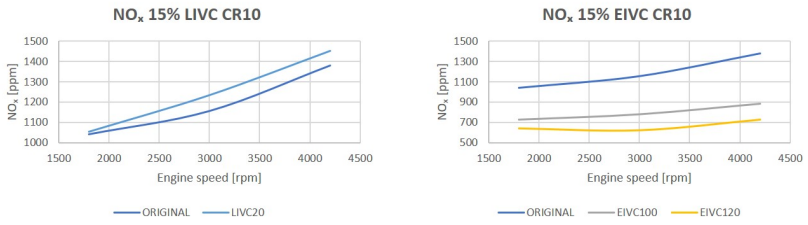

(a) **(b)**

Figure 4.14: NO_x emissions 15%: LIVC (a), EIVC (b).

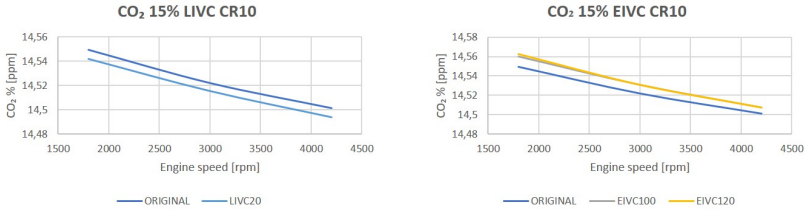

(a) **(b)**

Figure 4.15: CO_2 emissions 15%: LIVC (a), EIVC (b).

As explained in subsection 2.4.2, NOx formation is aided by high temperatures.
For EIVC100 and EIVC120 a significant reduction of NO_x can be noticed due to the strong advance of the intake valve closure that reduces the effective compression ratio, thus lowering the in-cylinder temperature at the end of the compression stroke.
This positive effect does not hold for LIVC20.
Moving to CO_2, neither a significant reduction nor an increase is observed, hence it can be considered constant in each case.

Part load 30%

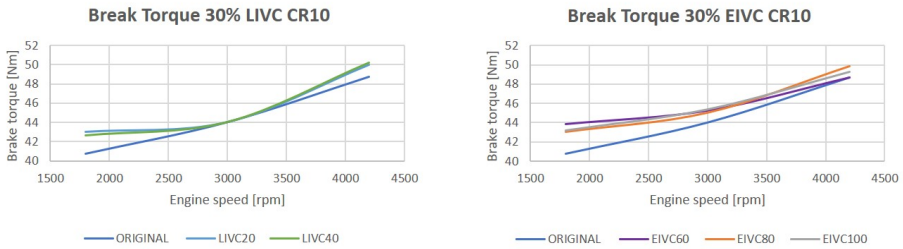

(a) **(b)**

Figure 4.16: Brake torque 30%: LIVC (a), EIVC (b).

In both LIVC cases, the brake torque does not reach perfect convergence at 1800 and 4200 rpm, but at 3000 rpm a perfect match between all the curves is found.
For EIVC cases, the accuracy of the prediction increases as the engine speed grows.
Here the BSFC and total efficiency behaviours are displayed:

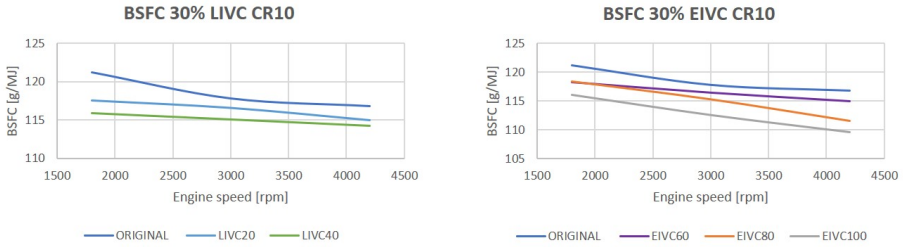

(a) **(b)**

Figure 4.17: BSFC 30%: LIVC (a), EIVC (b).

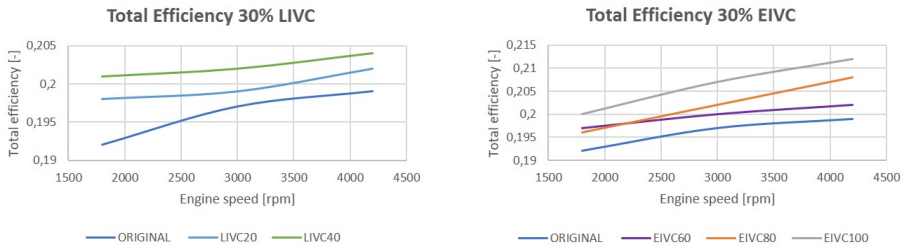

(a) **(b)**

Figure 4.18: Total efficiency 30%: LIVC (a), EIVC (b).

Looking at BSFC plots of the LIVC configurations, the highest discount in fuel consumption is encountered at 1800 rpm thanks to a delay of 40°CA, moving from 121.2 g/MJ (ORIGINAL) to 115.9 g/MJ (LIVC40) and yielding +0.9% in total efficiency (from 19.2% to 20.1%).
The most favourable configuration among all, is EIVC100 that presents a drop in BSFC of 7.2 g/MJ (from 116.8 g/MJ to 109.6 g/MJ) that translates into an increase of total efficiency of 1.3% (from 19.9% to 21.2%).
Such improvements are deduced from the reduction of the compression work area in the p-V diagrams as well:

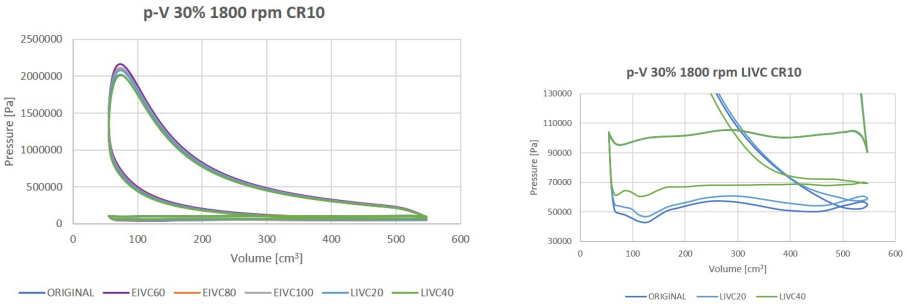

(a)

(b)

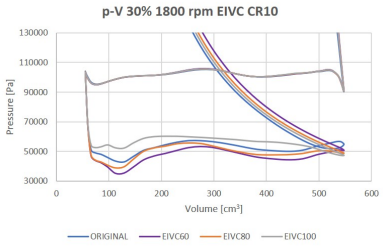

(c)

Figure 4.19: p-V diagram 1800 rpm 30% (a); LIVC (b), EIVC (c) close-ups.

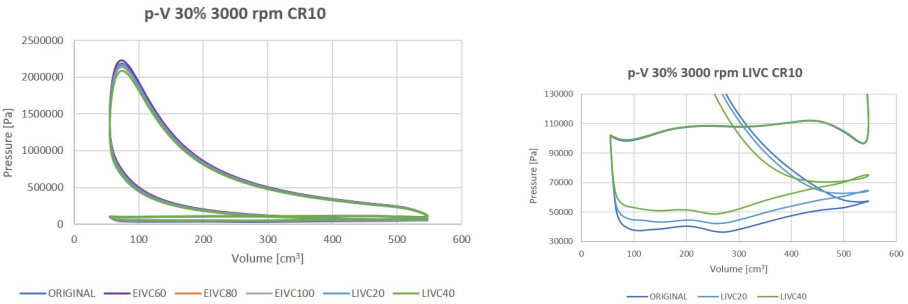

(a)

(b)

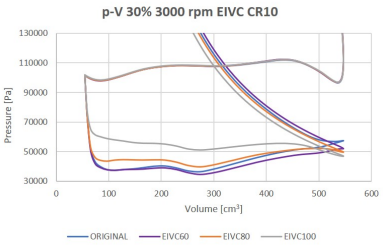

(c)

Figure 4.20: p-V diagram 3000 rpm 30% (a); LIVC (b), EIVC (c) close-ups.

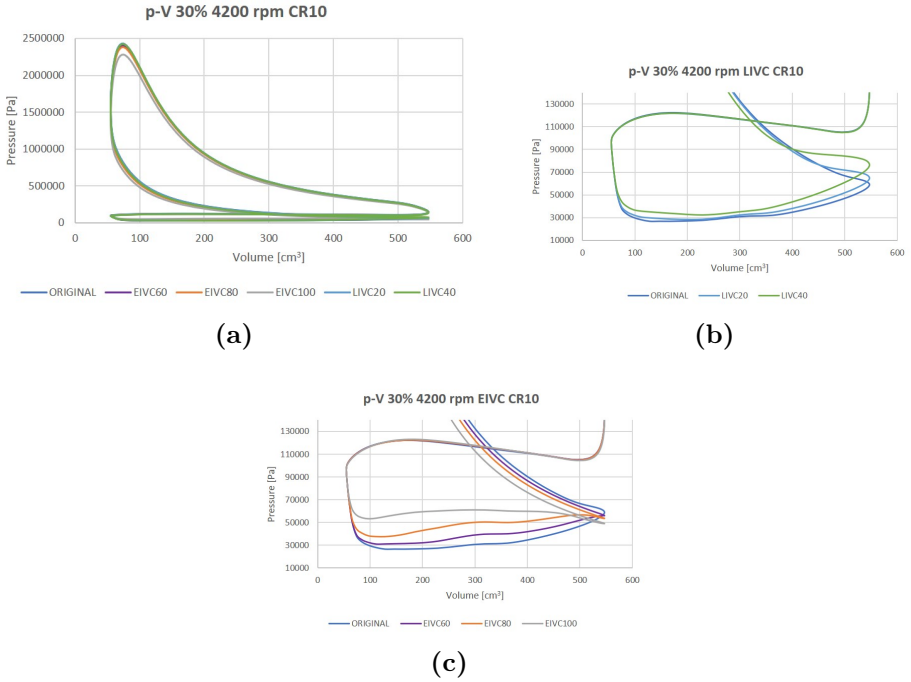

Figure 4.21: p-V diagram 4200 rpm 30% (a); LIVC (b), EIVC (c) close-ups.

For LIVC20 and LIVC40 a slight increase in NO_x emissions is registered. As expected, the decrease of in-cylinder temperature derived from an advance of 100°CA of the intake valve closure carries a reduction in NO_x formation with it. More specifically, the emissions move from 1954.8 ppm (ORIGINAL case) to 1325.8 ppm (EIVC100).
CO_2 emissions decreases for LIVC20 and LIVC40 only, while in EIVC cases they increase minimally. In both cases they can be considered almost the same of the ORIGINAL case ones.

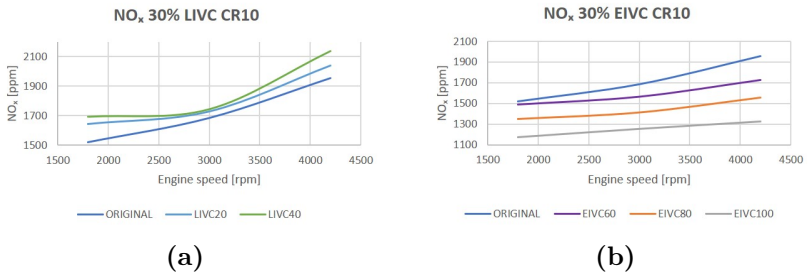

Figure 4.22: NO_x emissions 30%: LIVC (a), EIVC (b).

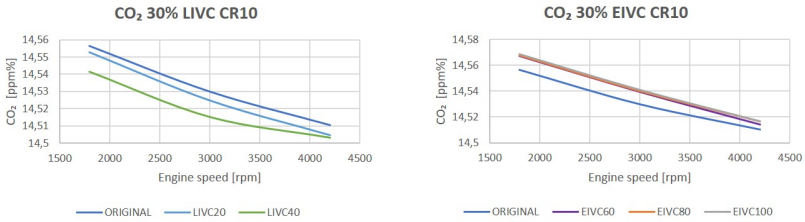

(a) **(b)**

Figure 4.23: CO_2 emissions 30%: LIVC (a), EIVC (b).

Part load 50%

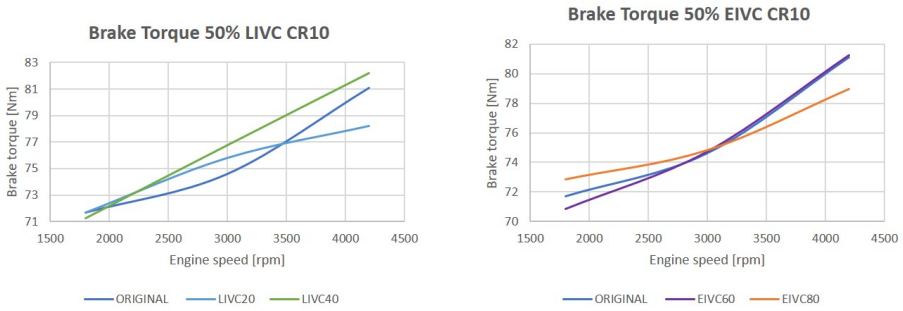

(a) **(b)**

Figure 4.24: Brake torque 50%: LIVC (a), EIVC (b).

As shown by the plot, LIVC20 and LIVC40 brake torques do not adhere perfectly to the ORIGINAL desired one at 3000 and 4200 rpm. However, as the target value of the torque increases, these errors are less influential. For example, in the worst case shown in Figure 4.24a, the error is:

$$err\% = \frac{T_{LIVC40} - T_{ORIGINAL}}{T_{ORIGINAL}} \times 100\% = \frac{(76.774 - 74.612)Nm}{74.612Nm} \times 100\% = 2.9\%$$

Hence it is acceptable, but it should still be taken into account when comparisons with other cases are made.
The same applies for EIVC80, while EIVC60 shows a good overlapping with the ORIGINAL trend.
BSFC and total efficiency plots are presented below:

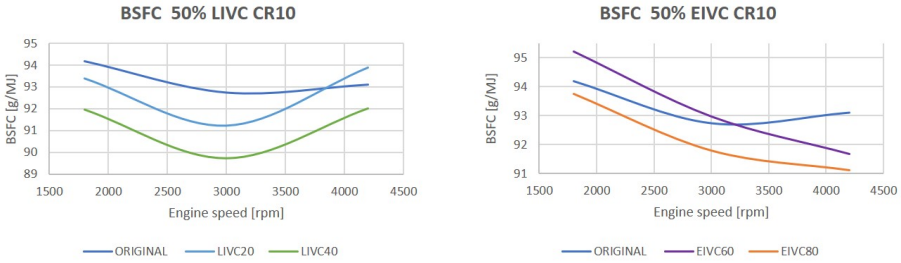

(a) **(b)**

Figure 4.25: BSFC 50%: LIVC (a), EIVC (b).

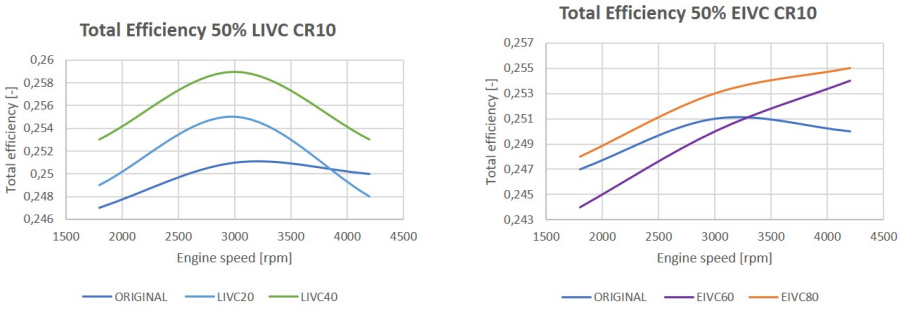

(a) **(b)**

Figure 4.26: Total efficiency 50%: LIVC (a), EIVC (b).

Both LIVC configurations lead to a consistent reduction in BSFC aside from LIVC20 which shows a slight increase at 4200 rpm. In particular, LIVC40 is characterized by a discount of 3 g/MJ at 3000 rpm.
Similarly, total efficiency spikes at 3000 rpm in both LIVC20 and LIVC40; the highest improvement is found for the latter: 25.9% with respect to 25.1% of the ORIGINAL case.
EIVC80 BSFC curve lays below the ORIGINAL one within the whole engine speed range, while for EIVC60 trend, an improvement in fuel economy arises from 3000 rpm forward. The best situation verifies at 4200 rpm for EIVC80, where BSFC goes from 93.1 g/MJ to 91.1 g/MJ and total efficiency grows from 25% to 25.5%.
Here, p-V diagrams are reported as an additional representation of the aforementioned enhancements:

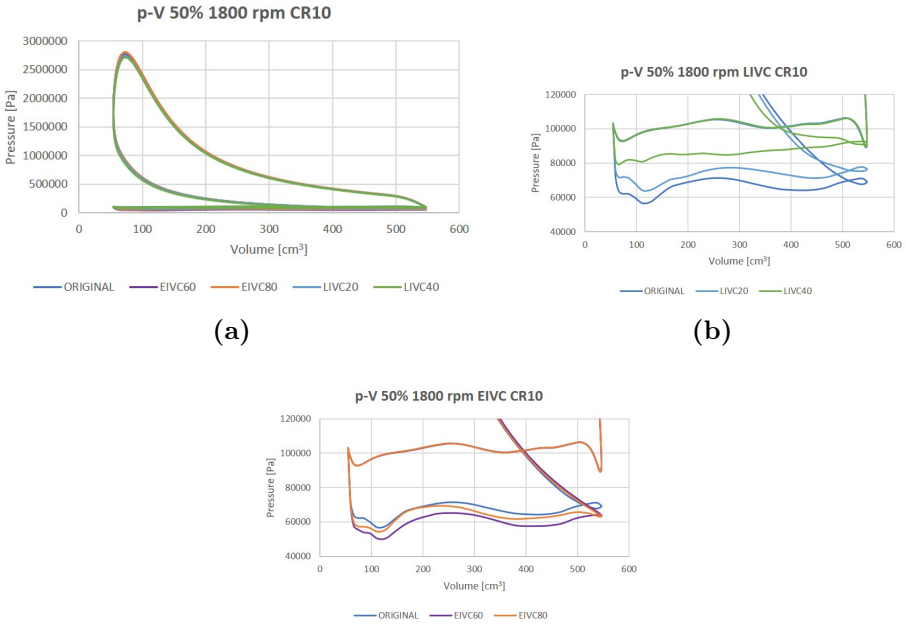

Figure 4.27: p-V diagram 1800 rpm 50% (a); LIVC (b), EIVC (c) close-ups.

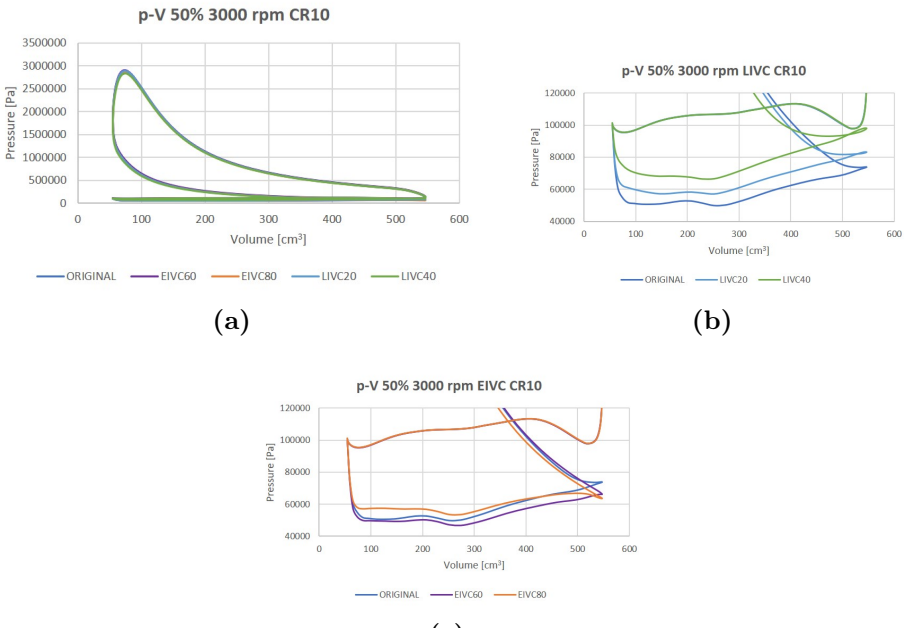

Figure 4.28: p-V diagram 3000 rpm 50% (a); LIVC (b), EIVC (c) close-ups.

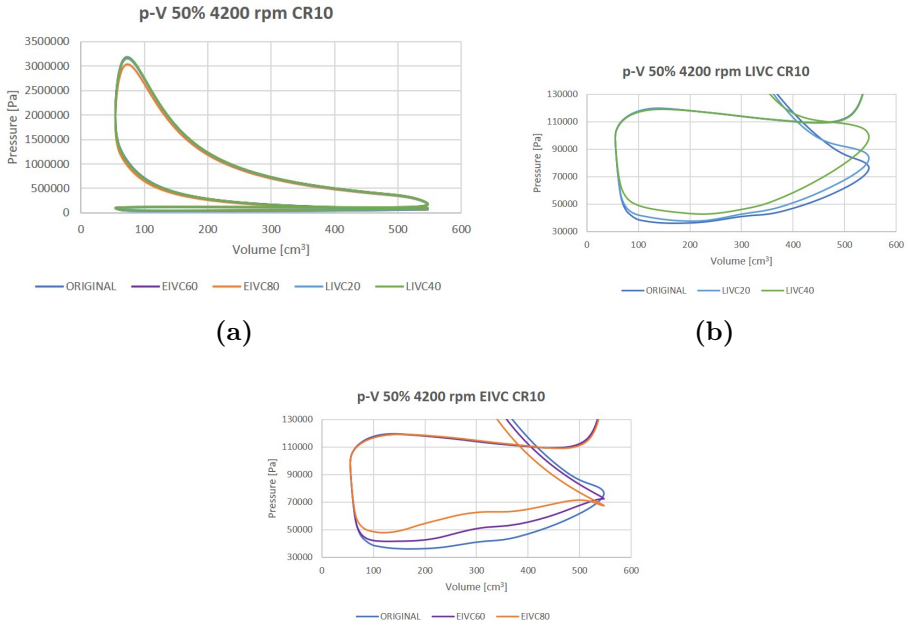

(a) **(b)**

(c)

Figure 4.29: *p-V* diagram 4200 rpm 50% (a); LIVC (b), EIVC (c) close-ups.

Some additional considerations can be made for pollutants.

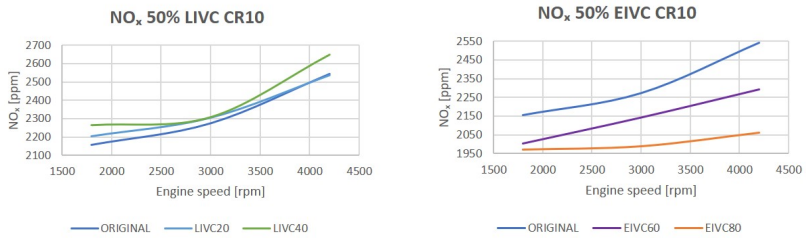

(a) **(b)**

Figure 4.30: NO_x emissions 50%: LIVC (a), EIVC (b).

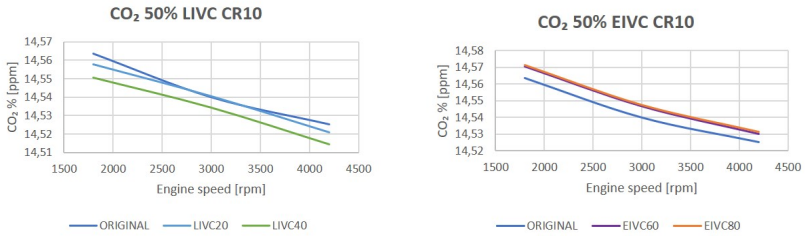

(a) **(b)**

Figure 4.31: CO_2 emissions 50%: LIVC (a), EIVC (b).

EIVC60 and EIVC80 a significant reduction of NO_x can be noticed; in particular, EIVC80 configuration reduces NO_x emissions of 483 ppm. This positive effect does not hold for LIVC20 and LIVC40.
Moving to CO_2, neither a significant reduction nor an increase is observed, hence it can be considered constant in each case.

Part load 70%

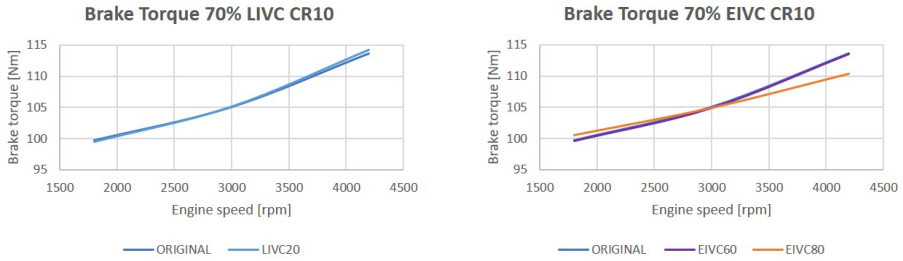

(a) **(b)**

Figure 4.32: Brake torque 70%: LIVC (a), EIVC (b).

Looking at LIVC20 plot, the brake torque reaches perfect convergence. EIVC60 and the first half of EIVC80 match the ORIGINAL trend as well.

Here the BSFC and total efficiency behaviours are displayed:

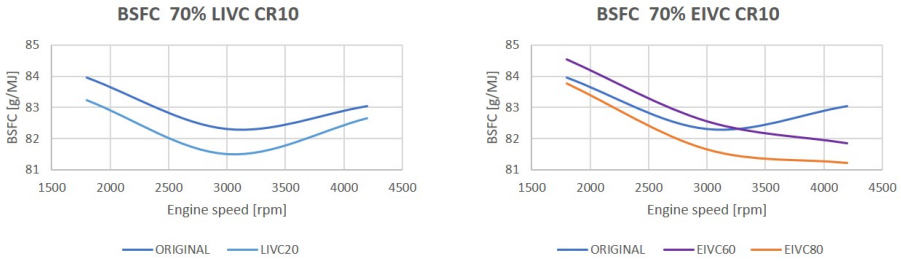

(a) **(b)**

Figure 4.33: BSFC 70%: LIVC (a), EIVC (b).

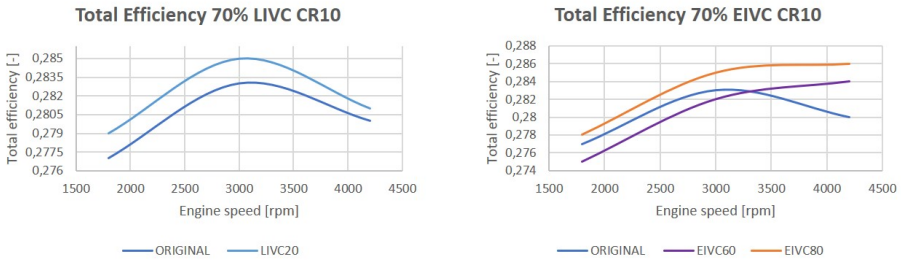

(a) **(b)**

Figure 4.34: Total efficiency 70%: LIVC (a), EIVC (b).

As the part load percentage increases, the advantage derived from a further opening of the throttle valve becomes less evident; this translates into a smaller relative BSFC reduction and total efficiency growth as shown by the graphs above.
In fact, the maximum discount in BSFC among all the selected configurations is recorded for EIVC80 at 4200 rpm and consists in -1.8 g/MJ; the highest value of total efficiency reached by the same configuration is 28.6% (+0.6%).
Therefore, an expectable shrinking of compression work area can be noticed in the p-V diagrams:

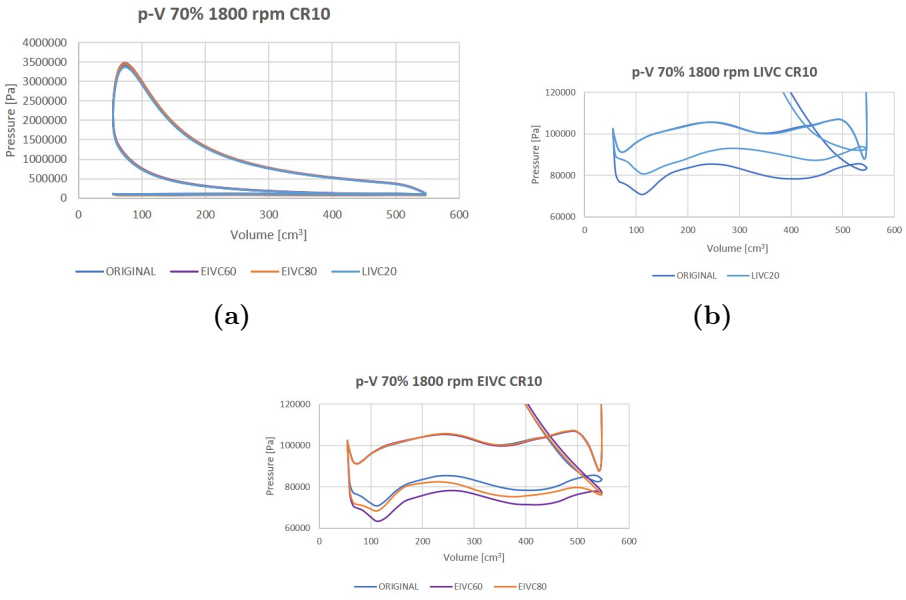

Figure 4.35: p-V diagram 1800 rpm 70% (a); LIVC (b), EIVC (c) close-ups.

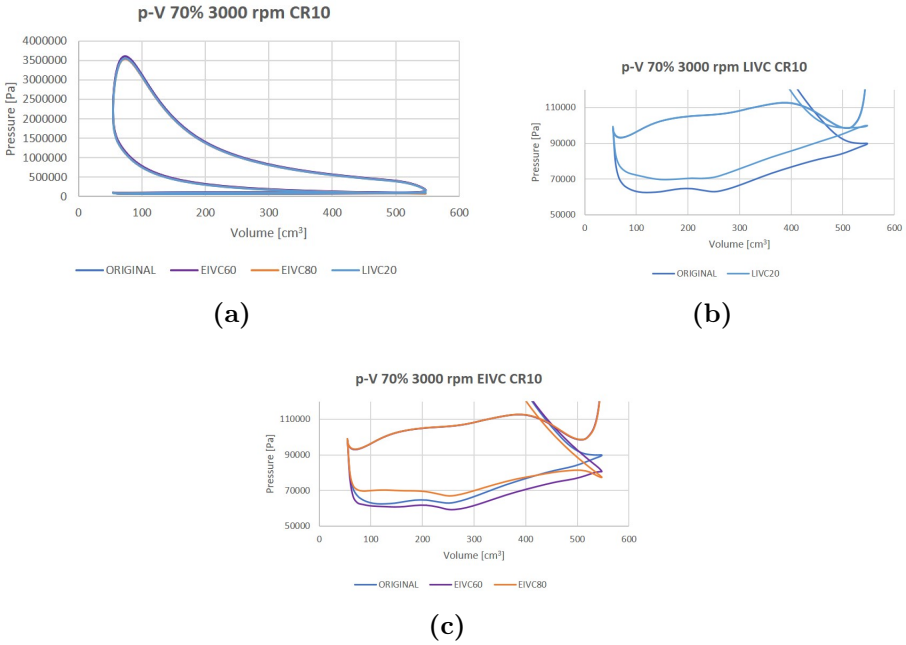

Figure 4.36: p-V diagram 3000 rpm 70% (a); LIVC (b), EIVC (c) close-ups.

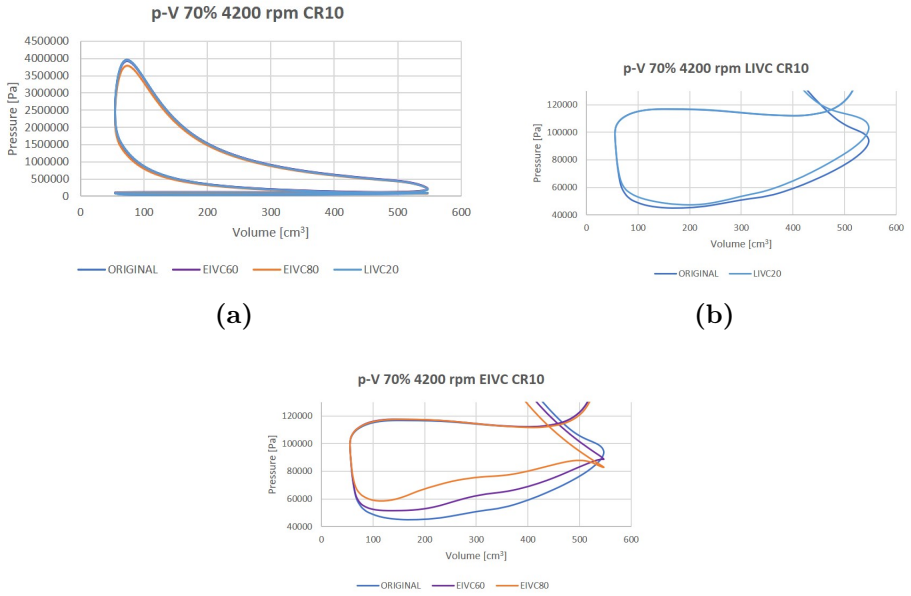

(a) **(b)**

(c)

Figure 4.37: p-V diagram 4200 rpm 70% (a); LIVC (b), EIVC (c) close-ups.

The only relevant consideration about pollutant emissions concerns the reduction of NO_x release.
In particular, EIVC80 yields the heaviest reduction at 4200 rpm (465.4 ppm).

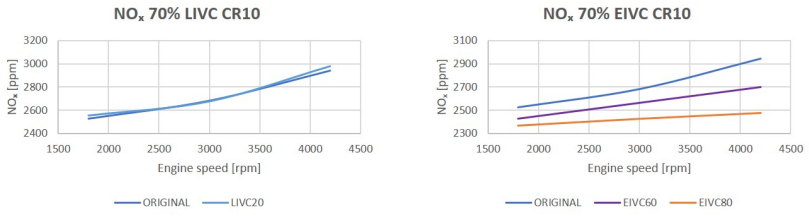

(a) **(b)**

Figure 4.38: NO_x emissions 70%: LIVC (a), EIVC (b).

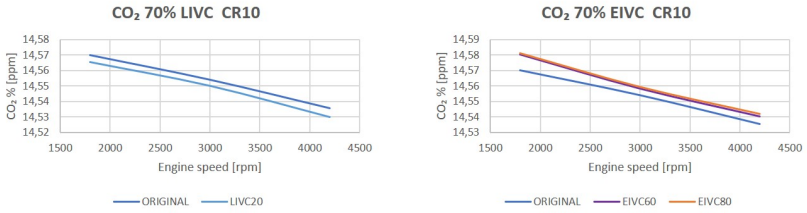

(a) **(b)**

Figure 4.39: CO_2 emissions 70%: LIVC (a), EIVC (b).

4.5 GCR increase

LIVC and EIVC application's main drawback is the reduction of the effective compression ratio ECR, that in turn leads to a decrease of thermal efficiency.
Hence, the final part of this work examines the advantages of coupling LIVC/EIVC strategies to increased GCR.
Geometric compression ratio can be increased by reducing the volume of the combustion chamber by increasing another geometrical parameter, squish width.
A graphical representation of the cylinder head is provided in Figure 4.40:

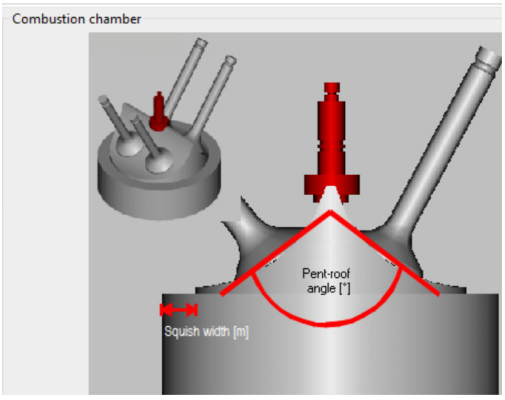

Figure 4.40: Cylinder head.

A GCR of 13 is obtained for a squish width of 0.014 m.
This value of GCR has been chosen after several attempts to change the cylinder geometry in Gasdyn, spotting the geometrical limits of the engine.

4.5.1 Results and discussion

The same amount of simulations as the previous action has been done, but in this section only the most significant ones are discussed and compared to the ORIGINAL case.

Part load 15% and 30%

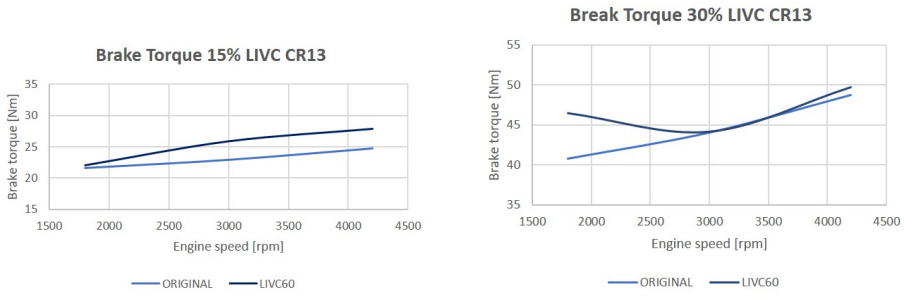

(a) **(b)**

Figure 4.41: Brake torque 15% CR13 LIVC (a) and 30% CR13 LIVC (b).

With the application to both part loads of LIVC alone, brake torque does not reach convergence at all due to the excessive reduction of ECR. If a delay of 60°CA is coupled with an increase of GCR, brake torque approaches to the ORIGINAL trend carrying an error of few Nm with it.

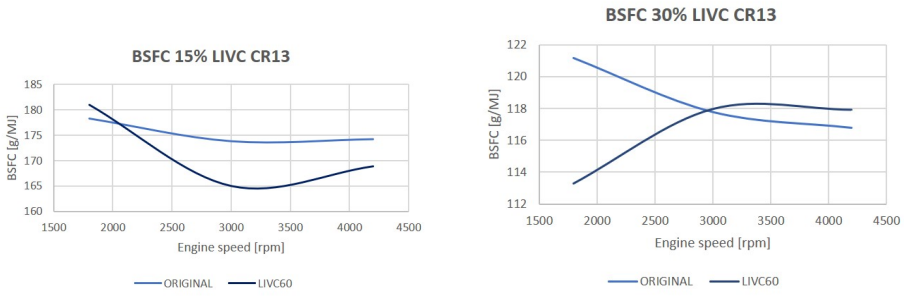

(a) **(b)**

Figure 4.42: BSFC 15% CR13 LIVC (a) and 30% CR13 LIVC (b).

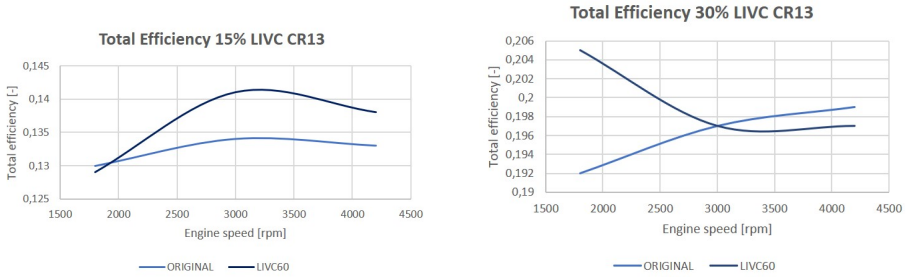

(a) **(b)**

Figure 4.43: Total efficiency 15% CR13 LIVC (a) and 30% CR13 LIVC (b).

At part load 15%, the greatest enhancements are obtained at 3000 rpm (-8.9 g/MJ of fuel consumption and +0.7% in total efficiency).
While at part load 30%, LIVC60 is advantageous from 1800 to 3000 rpm only, then BSFC goes beyond the ORIGINAL value; similarly, total efficiency is greater than the ORIGINAL one in the first portion of the engine speed range, then it decreases.
In p-V diagrams, a strong reduction of compression work area can be noticed:

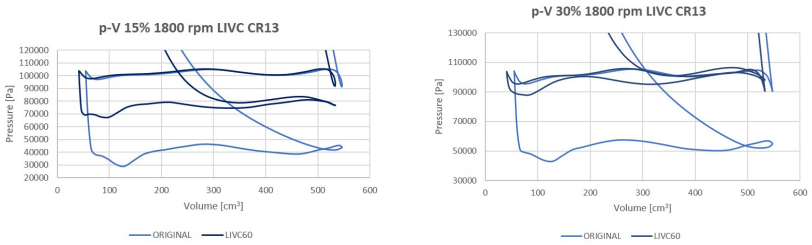

(a) **(b)**

Figure 4.44: p-V diagram 1800 rpm 15% CR13 LIVC (a) and 30% CR13 LIVC (b).

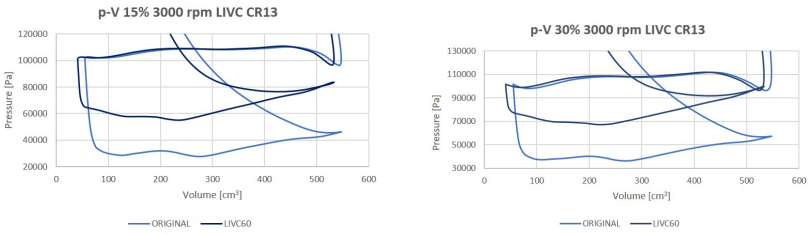

(a) **(b)**

Figure 4.45: p-V diagram 3000 rpm 15% CR13 LIVC (a) and 30% CR13 LIVC (b).

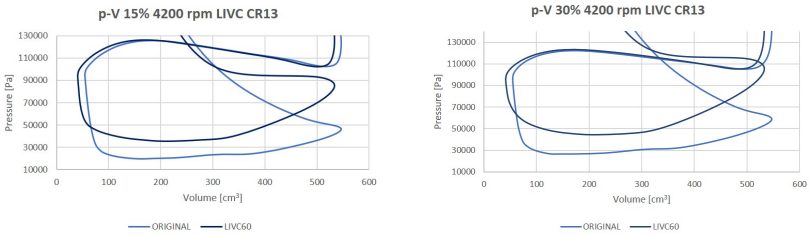

(a) **(b)**

Figure 4.46: p-V diagram 4200 rpm 15% CR13 LIVC (a) and 30% CR13 LIVC (b).

As GCR increases, the in-cylinder temperature rises with it, hence, one main drawback of this action is the higher production of NO_x.
On the other hand, CO_2 production slightly decreases.

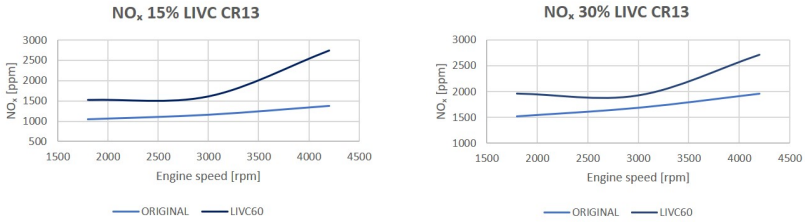

(a) **(b)**

Figure 4.47: NO_x emissions 15% CR13 LIVC (a) and 30% CR13 LIVC (b).

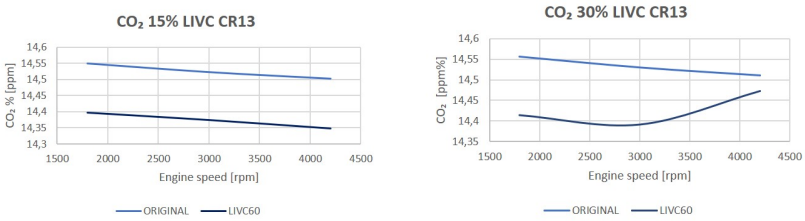

(a) **(b)**

Figure 4.48: CO_2 emissions 15% CR13 LIVC (a) and 30% CR13 LIVC (b).

Part load 50%

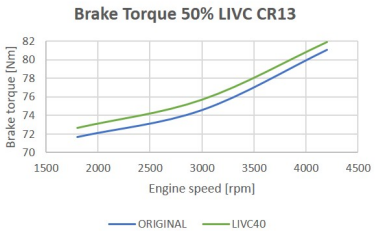

Figure 4.49: Brake torque 50% CR13 LIVC.

LIVC40 brake torque matches the targets.

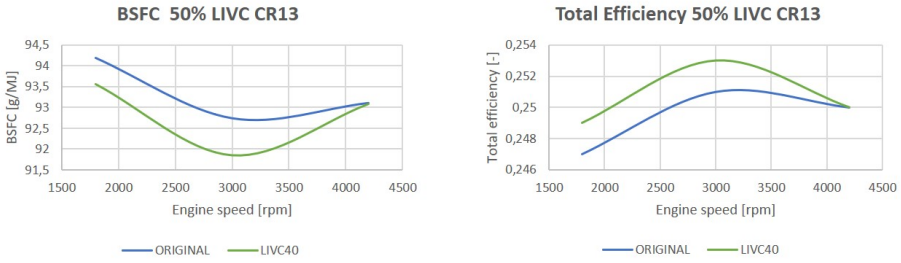

(a) **(b)**

Figure 4.50: BSFC 50% CR13 LIVC (a), total efficiency 50% CR13 LIVC (b).

Intermediate regimes are characterized by appreciable improvements in both fuel economy and total efficiency: BSFC goes from 92.7 g/MJ to 91.8 g/MJ and total efficiency from 25.1% to 25.3%.
p-V diagrams reflect these enhancements as well:

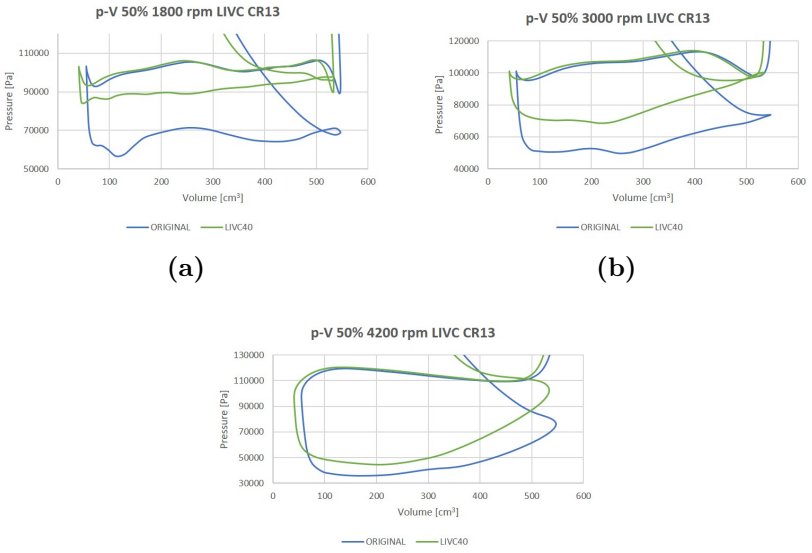

(a) **(b)**

(c)

Figure 4.51: p-V diagrams 50% CR13 LIVC, 1800 rpm (a), 3000 rpm (b), 4200 rpm(c).

An increased NO_x production and a minor decrease of CO_2 emissions take place.

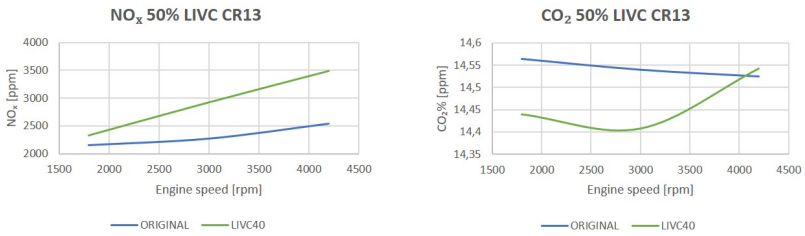

(a) **(b)**

Figure 4.52: NO_x emissions 50% CR13 LIVC (a), CO_2 emissions 50% CR13 LIVC (b).

Part load 70%

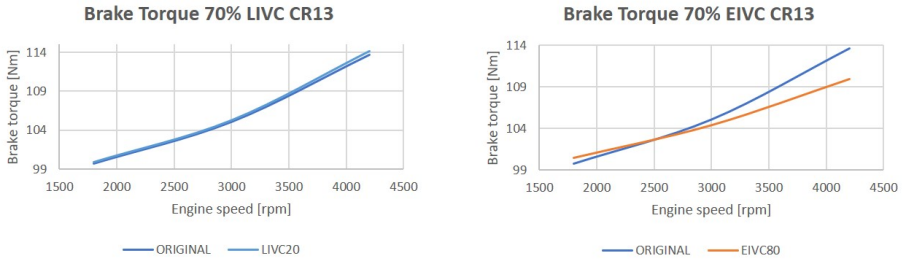

(a) **(b)**

Figure 4.53: Brake torque 70% CR13 LIVC (a), EIVC (b).

LIVC20 confirms a good correspondence with the ORIGINAL trend, while EIVC80 brake torque minimally departs from the desired values from 3000 rpm forward.

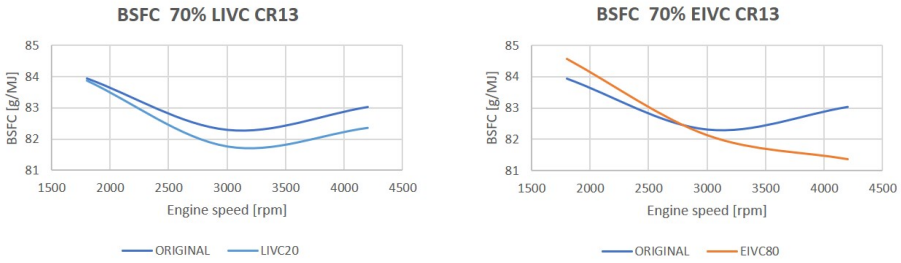

(a) **(b)**

Figure 4.54: BSFC 70% CR13 LIVC (a), EIVC (b).

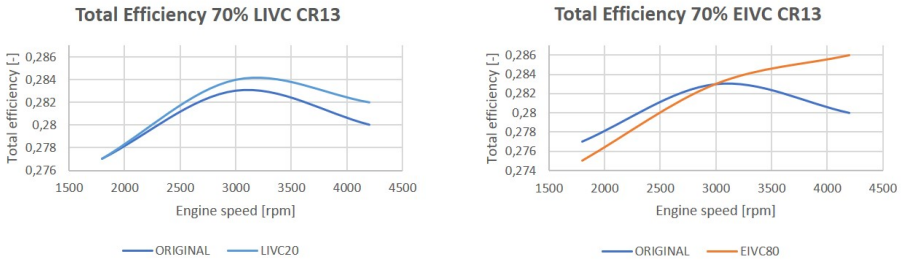

(a) **(b)**

Figure 4.55: Total efficiency 70% CR13 LIVC (a), EIVC (b).

Looking at LIVC20 behaviours, the benefits in BSFC and efficiency deriving from the adoption of new GCR grow as the engine speed becomes higher (-0.7 g/MJ and +0.2% at 4200 rpm).
The adoption of an advance of 80°CA in the inlet valve closure is advantageous only for engine speeds higher than 3000 rpm; in particular BSFC starts falling, reaching its minimum value (81.37 g/MJ) at 4200 rpm, and total efficiency has a peak at the same rotational speed (28.6%).
p-V diagrams are reported as an additional representation of these behaviours:

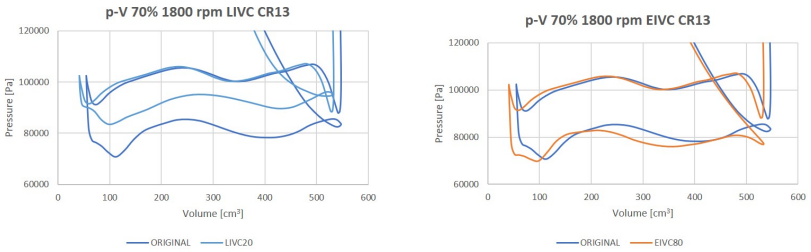

(a) **(b)**

Figure 4.56: p-V diagrams 1800 rpm 70% CR13 LIVC (a), EIVC (b).

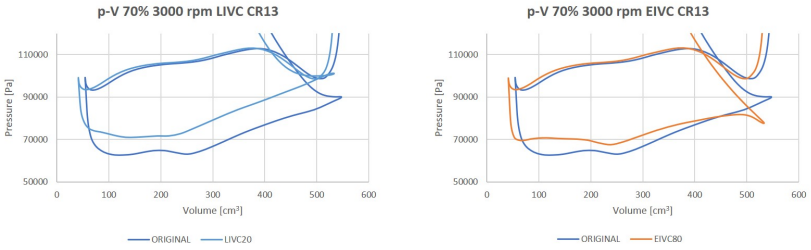

(a) **(b)**

Figure 4.57: p-V diagrams 3000 rpm 70% CR13 LIVC (a), EIVC (b).

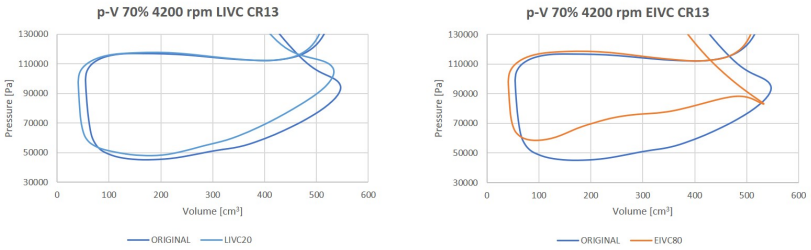

(a) **(b)**

Figure 4.58: p-V diagrams 4200 rpm 70% CR13 LIVC (a), EIVC (b).

In both cases, NO_x production increases as expected.
CO2 emissions are almost the same for EIVC80, while, if a delay of 20°CA is applied, they sharply fall.

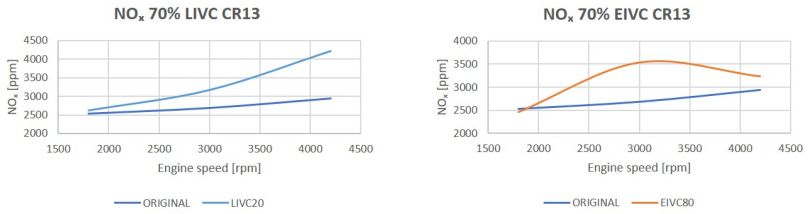

(a) **(b)**

Figure 4.59: NO_x emissions 70% CR13 LIVC (a), EIVC (b).

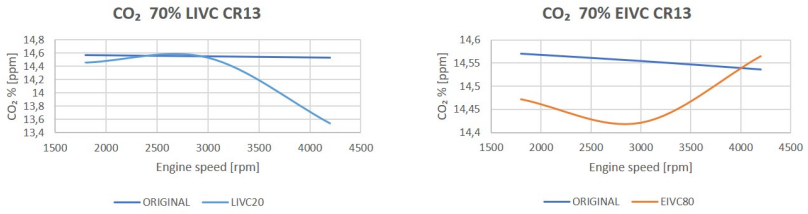

(a) **(b)**

Figure 4.60: CO_2 emissions 70% CR13 LIVC (a), EIVC (b).

Conclusions

Based on the research performed for this thesis, the following conclusions can be given:

1. The engine validation phase was successful, hence Gasdyn simulations are reliable;

2. During the part load setting phase, a good convergence has been reached in almost every case, except for those that implied an excessive reduction of ECR due to heavy delays or advances in the intake valve closure;

3. The greatest relative improvements in fuel economy and total efficiency have been achieved at low loads (15% and 30%), where the effect of pumping loss reduction is more significant;

4. As expected, NO_x emissions decreased thanks to the reduced in-cylinder temperature as a consequence of lower ECR while CO_2 emissions did not face a significant change;

5. The increase of GRC made it possible to adopt delays that were higher than those applied to the CR10 cases at low loads (e.g. LIVC60 at 15% and 30%).

An extension of this thesis can be made by deriving some engine performance maps of torque, power, BSFC and emissions to make a global analysis of engine performances.
Possible future works can be based on the introduction of a turbocharger coupled with efficient intake cooling improving the knocking resistance and assessing the problem of reduced power density.
Another promising technical measure for achieving optimum performance within the entire engine speed and load range is VVT + VCR. A VCR mechanism is crucial, but it increases engine complexity and cost. Some technical challenges are needed to realize VCR mechanisms.

Bibliography

[1] Desmond E Winterbone and Richard J Pearson. *Theory of engine manifold design: wave action methods for IC engines*. Wiley-Blackwell, 2000.

[2] Giancarlo Ferrari. *Internal combustion engines*. Società Editrice Esculapio, 2014.

[3] Cristian Ierardi. "Sviluppo, aggiornamento e introduzione del trasporto di specie chimiche nel metodo 3D Cell per la simulazione 1D di motori a combustione interna". Tesi di laurea magistrale. Politecnico di Milano, 2018/2019.

[4] Matteo Tamborski. "Simulazione 1D dei flussi instazionari nei motori a c.i. mediante i metodi numerici CE-SE e GC-TVD". Tesi di laurea magistrale. Politecnico di Milano, 2017/2018.

[5] Jinxing Zhao. "Research and application of over-expansion cycle (Atkinson and Miller) engines–A review". In: *Applied Energy* 185 (2017), pp. 300–319.

[6] Tie Li et al. "The Miller cycle effects on improvement of fuel economy in a highly boosted, high compression ratio, direct-injection gasoline engine: EIVC vs. LIVC". In: *Energy conversion and management* 79 (2014), pp. 59–65.

[7] Renhua Feng et al. *Investigations of atkinson cycle converted from conventional otto cycle gasoline engine*. Tech. rep. SAE Technical Paper, 2016.

[8] Richard Osborne et al. "A Miller cycle engine without compromise–The Magma concept". In: *17. Internationales Stuttgarter Symposium*. Springer. 2017, pp. 1507–1529.

[9] Fredrik Holst and Manne Solbreck. "Numerical and Experimental Investigation of the Atkinson Cycle on a 2.0 liter 4-cylinder Turbocharged SI-engine". In: *Göteborg, Sweden* (2014).

[10] Alberto Boretti and Joseph Scalzo. *Exploring the advantages of atkinson effects in variable compression ratio turbo GDI engines*. Tech. rep. SAE Technical Paper, 2011.

[11] Aaron Isenstadt et al. "Downsized, boosted gasoline engines". In: *The international council on clean transportation* (2016).

[12] Mark Stuhldreher et al. "Benchmarking a 2016 Honda Civic 1.5-Liter L15B7 Turbocharged Engine and Evaluating the Future Efficiency Potential of Turbocharged Engines". In: *SAE International Journal of Engines* 11.2018-01-0319 (2018), pp. 1273–1305.